Raman Scattering
in
Optical Fibres

David Alan Wardle

A thesis submitted in partial fulfilment of the requirements
for the degree of Doctor of Philosophy in Physics

The University of Auckland

January 1999

Abstract

The Raman effect is the inelastic scattering of photons by matter. When a monochromatic light beam (pump beam) propagates in an optical fibre, spontaneous Raman scattering transfers some of the photons to new frequencies. The probability of a photon scattering to a particular frequency shift, depends on that frequency shift, forming a characteristic spectrum. The scattered photons may lose energy (Stokes) or gain energy (anti-Stokes). If the pump beam is linearly polarized, then the polarization of scattered photons may be the same (parallel scattering) or orthogonal (perpendicular scattering). If photons are already present at other frequencies then the probability of scattering to those frequencies is enhanced (stimulated scattering).

In this thesis, the equations governing the Raman effect, both in bulk glass and single mode fibre, are restated. The probability of spontaneous scattering (parallel and perpendicular) in an optical fibre has been measured for frequency shifts between 4THz and 58THz. Particular attention has been given to those frequency shifts where the scattering is intrinsically weak. This has identified those frequency shifts where it might be possible to eliminate Raman noise from experiments designed to generate quantum states of light in optical fibres using four wave mixing.

From the measured scattering probabilities, the Raman equations can be used to predict the scattering cross-section in bulk glass. The prediction is found to be in reasonable agreement with measurements of the bulk glass cross-section published by other authors.

By increasing the pump power, the transition to stimulated scattering has been observed. In the case of Stokes scattering there is reasonable agreement between the Raman equations and experimental observations. In the case of anti-Stokes scattering, and in the limit of very high pump power, behaviour is observed which is not predicted by the Raman equations, indicating that other processes must be included to successfully describe such experiments.

Preface

This thesis is primarily concerned with the propagation of light in optical fibres, in particular, with the propagation of visible wavelength laser beams, including kilowatt peak power pulses, in single mode, fused silica fibres. The organization of the thesis is as follows.

Chapter 1 gives an overview of the research undertaken, including an account of the original motivation for the research, a brief review of the relevant work which has already been performed, and an appraisal of the significance of the results obtained. A more comprehensive review of the relevant literature on the Raman effect is given in Chapter 2. Both Chapter 1 and Chapter 2 assume a familiarity with modern optics. Less well prepared readers are therefore advised to skip over these chapters and begin with Chapter 3.

Chapter 3 gives an introduction to the basic physics of some optical phenomena, including all the phenomena encountered in this thesis. The perspective is perhaps a little unusual. Firstly, the discussion is conceptual rather than mathematical. Secondly, an attempt has been made to establish how the phenomena work at the microscopic level of charged particles and photons, and also to identify the underlying mechanisms common to all the phenomena. Because the chapter is non-mathematical, some of the behaviour is imprecisely defined. A more precise, mathematical description of the Raman effect is given in Chapter 5. The equations in Chapter 5 have been derived from a full quantum mechanical treatment, which is presented in Appendix A, but this treatment is not free of approximations. Since these approximations might, in some regimes, undermine the validity of the equations, the approximations are also summarized in Chapter 5. Chapters 3 and 5 and Appendix A are therefore complementary, with closely related, definitions, concepts and mathematics, distributed between the three chapters. The perplexed reader is encouraged to skip back and forth between these chapters in search of enlightenment.

Chapter 4 gives a brief introduction to optical fibres, including relevant mathematical results. Chapter 6 generalizes the equations for the Raman ef-

fect in Chapter 5 to deal with complications which arise in real experiments, discussing, for example, pulse propagation and fibre loss. It also begins to describe how Raman scattering measurements are actually made, although from a somewhat theoretical point of view. How measurements are made from an experimental point of view should become clear on reading Chapter 7, which gives an overview of the apparatus used in this thesis. The calibration of the apparatus is discussed in Chapter 8.

The actual experimental results are divided between Chapters 9 and 10. Chapter 9 deals with the spontaneous scattering experiments, which are essentially experiments performed at low powers. The experimental results are compared with theoretical predictions and/or with measurements made by other authors. Chapter 10 deals with the stimulated scattering experiments, which are essentially experiments which extend into a regime of greater powers. Again experimental results are compared with theoretical predictions.

Finally, Chapter 11 summarizes the results and makes some concluding remarks.

Contents

List of Figures

List of Tables

List of mathematical symbols

This is a list of the most widely used symbols found in the chapters. It is not a complete list. The symbols used in Appendix A are excluded, although every attempt has been made in Appendix A to keep the notation consistent where possible.

Symbols subscripted p denote the value of the quantity appropriate to the pump beam. Symbols subscripted $\parallel$ and $\perp$ are for parallel and perpendicular scattering respectively.

b_0	background which is independent of pump
b_p	background due to pump
c	speed of light in vacuum
dA	infinitesimal of area
dV	infinitesimal of volume
$d\Phi$	infinitesimal of solid angle
$\mathbf{e}$	electric field unit vector
f	transverse mode profile
g	stimulated Raman gain coefficient for an optical fibre
$\hat{g}$	Raman gain coefficient (bulk glass geometry)
$h\,(\Omega, T)$	temperature dependence of spontaneous scattering (see Equation 5.3)
$\hbar$	Planck constant divided by 2π
ha#1	setting of horizontal adjust micrometer of mirror at #1 (see Figure 7.3)
k	Boltzmann constant
$n\,(\omega)$	refractive index for light of angular frequency ω
r	radial distance from centre of fibre
$\hat{r}$	mode field radius
t	laboratory time
v	group velocity of Raman light
v_g	group velocity
v_p	group velocity of pump
$\hat{x}$	mode field radius in x direction

$\hat{y}$	mode field radius in y direction
z	distance down fibre
A_{eff}	effective area of overlap between two beams
C	count rate at photomultiplier tube
$F(\omega)$	filter function of monochromator
I	overlap integral
$M_{\parallel}$, $M_{\perp}$	material Raman functions
P_p	pump power
R	spontaneous Raman scattering coefficient for an optical fibre
$\hat{R}$	spontaneous Raman scattering differential cross-section per unit volume
T	retarded time (Section 6.2). Temperature in kelvins (elsewhere).
T_F	temporal power FWHM
T_R	time between pulses from pulsed laser
α	fibre loss for Raman light
α_p	fibre loss for pump
β_2	group velocity dispersion parameter
ϵ_0	vacuum permittivity
η	collection efficiency of monochromator/PM tube
θ	far field divergence angle for light leaving fibre (see Figure 4.2), angle between electric field vectors of two light beams (elsewhere).
λ_c	centre wavelength of monochromator
$\bar{\nu}$	wavenumber separation between pump and scattered light (Equation 9.2)
ω	angular frequency of Raman scattered light
ω_c	centre angular frequency of monochromator/PM tube
ω_F	spectral power FWHM
ω_p	angular frequency of pump beam
Γ	optical power per unit angular frequency at angular frequency ω
Λ	intensity per unit angular frequency
Ω	difference between ω_p and ω (Raman frequency shift; positive for Stokes scattering)

List of abbreviations

cps	counts per second
cw	continuous wave (used in this thesis to describe a light source which is not time dependent or an experiment performed with such a source)
FWHM	full width at half maximum
PM	photomultiplier
QE	quantum efficiency
SRS	stimulated Raman scattering

Remark

Uncertainties quoted are estimates of standard deviation rather than, for example, 90% confidence limits.

Chapter 1

The Research

The purpose of this chapter is to provide readers well versed in the basic concepts of modern optics with a brief account of what research has been undertaken, why it was undertaken and the significance of the results obtained. Such readers may find Chapter 3 a useful glossary of terms. Less prepared readers are advised to skip this chapter completely and return to it when they have read some of the chapters which follow.

1.1 History of experiments at Auckland: four wave mixing in fibres and intensity difference squeezing

In the late 1980s experiments were performed at Auckland to try and generate and detect intensity difference squeezing using four wave mixing in single mode optical fibres [22]. In these experiments, pulses (about 50ps duration, 500W peak power and visible wavelength) from a mode locked laser (pump beam) were launched into a single mode, polarization preserving fibre. Phase matched four wave mixing resulted in the production of two new beams (sidebands) propagating in the same direction as the pump; one of longer wavelength (Stokes) and one of shorter wavelength (anti-Stokes). Since spectral measurements revealed that the energy of one Stokes photon and one anti-Stokes photon summed to give the energy of two pump photons, it was suggested that the sidebands are generated by single transitions in which two pump photons are destroyed and a Stokes/anti-Stokes pair created. This would result in the number of photons in the Stokes beam always equalling the number of photons in the anti-Stokes beam (intensity difference squeezing).

In the experiment each sideband was directed at a photodiode and the two photocurrents were subtracted. The theory predicts that the difference of the two photocurrents should exhibit a noise level beneath the so called 'shot-noise limit,' which constitutes an experimental demonstration of intensity difference squeezing. Typically the pump power was chosen so that the number of photons in each sideband pulse was of the order 10^6. It was essential to have at least this many photons or noise mechanisms inherent in the photodiodes and electronics would forbid the observation of any squeezing. Other experiments which have successful demonstrated intensity difference squeezing with short pulses have also involved pulses with a similar number of photons (see for example [10] and [81]).

Despite a considerable amount of effort no intensity difference squeezing was observed, although the amplitude fluctuations in each beam were shown to be strongly correlated. The measured power in the Stokes beam was found to be larger than the measured power in the anti-Stokes beam. This suggests the presence of stimulated Raman scattering (SRS). SRS can transfer photons from pump to Stokes. It can also transfer photons from anti-Stokes to pump. This would destroy the correlation in the photon number between the two sidebands.

1.2   Original research plan: intensity difference squeezing and photon counting

It was known at the time that the effects of SRS could be reduced by reducing the power of the pump beam. However, as already mentioned, this was not possible using the photodiode detectors. The original direction of this Ph.D. research was to replace the photodiodes with photon counting detectors (in this case photomultiplier tubes). This would allow considerable reduction in the pump power, hopefully eliminating SRS and allowing the intensity difference squeezing to be observed.

It should be pointed out that to date no experiment has detected intensity difference squeezing by photon counting on pairs of short pulses. In fact there are no experiments performed to date which show any non-classical effects by photon counting on short pulses. (Here 'short' means shorter than the response time of the detector. For all available photon counting detectors the response time is at least 100ps.) This is because even the most up to date photon counting detectors can only enumerate a very small number of photons (fewer than three) if the photons happen to arrive within the detector response time (for a recent discussion of the latest technology see

[48]).

In the early stages of this thesis considerable attention was given to the problem of detecting intensity difference squeezing in short pulses using photomultipliers. By extending a method for proving inequalities first suggested by Kovačec [47], and by using the new method to establish some new inequalities (which are refinements of the Cauchy-Buniakovsky-Schwarz inequality), a potentially successful scheme was devised. A requirement of the scheme is that the average number of photons in a sideband be reduced to below one. Unfortunately the opportunity to test the scheme was not forthcoming during the time available for this thesis, and this line of research will not be discussed further.

In some preliminary experiments the intensity of the pump was reduced to the point where each pump pulse produced on average about one photon in each sideband. Under these conditions it was found that most of the photons came, not from the four wave mixing, but from spontaneous Raman scattering (SponRS).

Unlike SRS, SponRS does not actually interact with the four wave mixing. There should be pairs of correlated photons but they are emerging coincidentally with a background of uncorrelated SponRS photons. Note that, for the squeezing experiment, this background cannot be removed by subtracting the mean SponRS signal from the measured results. This is because the actual number of Raman photons present in a pulse varies from pulse to pulse in an unpredictable, statistical fashion.

This brought research on intensity difference squeezing to a halt; at high pump powers SRS destroys the squeezing, at low pump powers the sidebands are contaminated by SponRS and, between these two regimes, it is not possible to carry out squeezing measurements because no suitable detectors are available.

1.3 Theory of Raman scattering in fibres

The focus of research therefore shifted to investigating how SponRS might be eliminated or, at least, reduced.

The obvious first step was to go to the literature in order to find out how the scattering depends on experimental parameters which might be varied (for example, the pump wavelength, the ambient temperature, and so on). There are a large number of papers, both theoretical and experimental, already published on Raman scattering in optical fibres. A survey of these reveals that most adopt what might be called the classical nonlinear optics model of the Raman effect. In this model, the light beams are treated as

classical waves and the gain coefficient of the fibre is a fitted parameter. The model successfully describes experiments in which a signal beam is launched into a fibre coincidentally with a pump beam and experiences amplification (or attenuation) due to SRS. The model does not account for spontaneous scattering. In particular, the model does not fully describe experiments in which a pump beam alone is incident on the fibre and other optical beams grow from the vacuum state. For a lucid exposition of the classical nonlinear optics model see the monograph by Agrawal [5].

Some authors have incorporated SponRS by simply adding to the classical nonlinear optics model white noise of arbitrary strength (see for example [92]). But, from a theoretical point of view, it is possible to calculate the strength of the spontaneous scattering from the fitted gain. In an early paper, Smith [80] gave the appropriate relations . Smith made the assumption that the temperature of the fibre was at absolute zero rather than room temperature and, rather unfortunately, omitted to state that this was the case. For the purposes of Smith's analysis this assumption introduces very small error (for Stokes scattering at the peak of the gain the error is only about 13%). However, in other experimental regimes the error is serious, in particular it predicts no spontaneous anti-Stokes scattering. Smith's incorrect results were subsequently cited by other influential authors (for example, [9] and [25]), and the incorrect results have now become widespread in the applied physics/engineering literature.

It is also possible to relate the spontaneous scattering in a fibre to the spontaneous scattering in bulk glass. The correct relations have been derived by O'Conner and Tauc [67], using a classical approach based on coherence, and also by Crosignani et al. [24], using the quantum theory of light. The quantum mechanical treatment has the advantage that it leads to a theory for scattering in fibres in which both spontaneous and stimulated scattering are treated in a unified manner. More recently, Carter and Drummond [20] have reviewed the quantum theory of light propagation in optical fibres. It is probably reasonable to remark that both the work of Crosignani et al. and the work of Carter and Drummond have a level of theoretical rigour which most applied physicists/engineers would find intimidating. For such readers, the experimental papers by Stolen and co-workers (see, for example, [82], [83] and [88]) are more accessible. These give the correct relations between the gain and spontaneous scattering in bulk glass and the gain in a fibre. Unfortunately the spontaneous scattering in the fibre is only treated in an approximate fashion (also some of the definitions are rather ambiguous, for example, there are ambiguities as to whether frequencies are Hz, rad/s or cm^{-1}).

All the correct results for the Raman effect in fibres are therefore al-

ready available in the literature but they are dispersed across several papers amongst a considerable amount of material that is not strictly correct. This is obviously an undesirable state of affairs. The correct equations are brought together in this thesis with a discussion of the assumptions necessary for their derivation. This is the first central result of this thesis.

1.4 Measurement of the spontaneous Raman scattering spectrum

Returning to the problem of eliminating SponRS from the four wave mixing experiments, it is clear from the Raman equations that varying the pump wavelength, ambient temperature or fibre material/geometry are unlikely to be successful strategies. The only approach with promise is to identify those angular frequency shifts and polarizations for which the SponRS is intrinsically weak. Spectra for SponRS in bulk samples of fused silica have been available in the literature since the 1950s. However, for this research, these spectra are not particularly useful as they have tended to concentrate on angular frequency shifts and polarizations for which the scattering is intrinsically strong. Early spectra concentrated on these regions because they give valuable information about the molecular structure of glass. More recent studies have concentrated on these regions because the relatively strong peaks in the spectra can be exploited in constructing fibre Raman amplifiers and lasers, and also because they are the dominant source of SRS induced cross talk in telecommunications applications.

A second drawback of the existing spectra is that, with a few exceptions, they are all what might be called relative spectra. That is, what is measured is the strength of the scattering at one frequency shift in comparison to the strength of the scattering at other frequency shifts. The absolute scattering probability at a particular frequency shift is not determined. But absolute measurements are exactly what is required in the context of this thesis, since the strength of the SponRS needs to be compared to the strength of the four wave mixing.

In this thesis, the absolute spontaneous Raman scattering spectrum of a single mode fibre has been measured directly. Both the parallel (polarization of scattered photon the same as linearly polarized pump) and perpendicular (scattered photon polarized at right angles to linearly polarized pump) spectra have been measured for angular frequency shifts ranging from 2.4×10^{13}rad/s to 3.5×10^{14}rad/s (4THz to 56THz). Minima in the perpendicular Raman spectra which might provide windows in which four wave

mixing experiments can be performed free of SponRS have been identified. This is the second central result of this thesis.

1.5   Testing the Raman equations

Using the Raman equations to guide the strategy for eliminating the Raman effect only makes sense if the Raman equations are known to be correct experimentally. However, to date the experimental testing of these equations has not been comprehensive. This is because the theory most widely used (the classical wave picture) does not include spontaneous scattering, and yet, in almost all experiments, some, or all, of the Raman light starts in the vacuum state and grows by spontaneous scattering. The decision was therefore made to dedicate the rest of the thesis to testing the validity of the Raman equations.

1.5.1   Spontaneous scattering

Measurements of the absolute spontaneous Raman scattering probability in bulk glass have previously been reported by Stolen and Ippen [83] and Hellwarth et al. [42]. Their results can be compared to the measured spontaneous scattering probability in an optical fibre using the equations derived by O'Conner and Tauc and by Crosignani et al. (see Section 1.3). This has been done and the results of the comparison found to support the equations. This is the third central results of this thesis.

Note that Brinkmeyer [16] has shown that the same equations also relate the backscattered Rayleigh light in fibres to Rayleigh scattering in bulk glass, and that the equations have been experimentally confirmed in the case of Rayleigh scattering by Gold and Hartog [35]. Also note that an absolute measurement of the spontaneous Raman scattering probability in a long length of ordinary (not polarization preserving) single mode fibre has previously been reported by Mochizuki et al. [61]. These authors also measured the stimulated gain in the same fibre. They could have related their spontaneous measurements to the spontaneous measurements in bulk glass, but instead related them, with considerable success, to their measured gain.

1.5.2   Stimulated scattering

In a Raman scattering experiment in which the Raman light grows from the vacuum state, if the pump power is increased then the number of scattered photons will also increase. At high pump powers the number of scattered

photons may become large enough for stimulated scattering to become significant. This transition from spontaneous to stimulated scattering has previously received very little attention. Stone [90] made relative measurements in a liquid core fibre filled with benzene. More recently, both Anders Olsson and Hegarty [1] and Aoki [7] have made absolute measurements in long lengths of ordinary (not polarization preserving) single mode fibre. Both authors have tried to reproduce their data with the Raman equations using the measured gain in their fibres as a fitted parameter. Anders Olsson and Hegarty get good agreement but Aoki seems to be in error by a factor of two. This may be due to the difficulties which arise relating the spontaneous scattering to the stimulated gain in fibres which do not preserve polarization.

As well as involving fibres which do not preserve polarization, these previous papers have only investigated scattering to the frequency shift where the scattering is strongest. In this thesis, the transition from spontaneous scattering to stimulated scattering is observed in a polarization preserving fibre, and for a range of frequency shifts, including some anti-Stokes shifts. The results are compared with predictions based on the Raman equations, with the strength of the spontaneous scattering as the only fitted parameter. In the case of Stokes scattering the agreement is reasonable. In the case of anti-Stokes scattering, and in the limit of very high pump power, behaviour is observed which is not predicted by the Raman equations, indicating that other processes must be included to successfully describe such experiments.

Chapter 2

Literature

Since its discovery in 1928 (Raman himself was awarded the Nobel Prize in 1930) the Raman effect has become a large subject, encompassing a number of subdisciplines (as well as Raman scattering in fibres, there are, for example, chemical analysis, chemical structure determination, surface enhanced Raman scattering, Raman microscopy). To review the whole subject is impractical, and also rather unnecessary, since many of the subdisciplines are not relevant to scattering in optical fibres. Despite being considerably younger, dating back only to the 1970s, the subdiscipline of scattering in fibres still amounts to a large enough number of papers to make the prospect of a review a forbidding task. Fortunately, many of these papers, whether justified or not, adopt the classical picture (see Section 1.3) and are therefore not particularly relevant in the context of this thesis. This chapter is an attempt to review that fraction of the literature which is relevant beyond the classical picture. It should not be misinterpreted as a comprehensive review of Raman scattering in optical fibres, since many of the papers dealing with classical pictures have been omitted. The chapter is directed at readers who already have some familiarity with the subject. Less well prepared readers are advised to skip to Chapter 3.

2.1 Some useful books

The textbook by Long [51] on Raman spectroscopy includes a brief review of the history of the Raman effect. The book discusses many aspects of the Raman effect, using classical models (light and matter treated using classical physics) with great clarity. A semi-classical theory (matter treated using quantum mechanics, light treated using classical mechanics) is also presented, but the presentation is rather less clear. A fully quantum picture

(light and matter treated using quantum mechanics) is not included. This is something of a drawback, since only in this picture can both spontaneous and stimulated scattering be described in rigorous terms.

The textbook by Loudon [53] makes no attempt to survey the full range of phenomena that are encompassed by the Raman effect. But it does give a fully quantum mechanical treatment for one simple system. This complements the material presented by Long. Having read both books, it should be clear how to construct a fully quantum mechanical treatment appropriate for any Raman scattering problem.

The textbook by Neumann [65] gives a useful introduction to optical fibres and the textbook by Agrawal [5] discusses the more specialized problem of pulse propagation in fibres. It should be pointed out that Agrawal uses a classical description of light, and that some of the phenomena experienced by propagating pulses lie outside such a description.

The book edited by Miller and Chynoweth [58], is a collection of contributions from researchers at Bell Labs. When it appeared in 1979 it must have represented almost everything that was known about optical fibre technology. Despite its age it remains a tremendous resource.

2.2   Early work

Prior to the advent of the laser in about 1960, measurement of Raman spectra was rendered difficult by the lack of a properly suited light source. Despite this, spontaneous Raman scattering spectra in bulk samples of fused silica were recorded during the 1950s. These were relative spectra, in which the frequencies of the spectral peaks were measured but not their absolute strength. A review of the early work has been given by Simon [78]. This review appears as one chapter in a collection [54]; the other chapters also contain useful information on other aspects of glass.

By the late 1960s, Bell, Dean and coworkers had developed a theory which allowed the frequencies of oscillation associated with the nuclear motion in fused silica to be predicted from first principles [13]. This theory starts with the normal modes of a single SiO_4 tetrahedron, and then uses a statistical approach to deal with the problem of a large number of the tetrahedra bonded together in an irregular network. The agreement between the predicted frequency spectra and the spectra observed in infra-red absorption and Raman scattering experiments is truely remarkable.

2.3 Relative spontaneous scattering spectra

A relative spontaneous scattering spectrum is one in which only the frequency shift axis is calibrated. The authors referenced in this section have made measurements at room temperature unless explicitly stated otherwise.

2.3.1 Bulk glass

Tobin and Baak [91] have measured the parallel and perpendicular scattering spectra for fused silica for frequency shifts from about 15cm^{-1} to about 1400cm^{-1}. Hass [38] has measured the parallel and perpendicular scattering spectra for both silica and germania for frequency shifts from 10cm^{-1} to 1300cm^{-1}. The spectra for silica were recorded at room temperature, liquid nitrogen temperature and liquid helium temperature. An earlier paper [37] gives a subset of these results. Winterling [101] has measured the parallel and perpendicular scattering of silica for frequency shifts from 4cm^{-1} to 650cm^{-1} at temperatures down to 40K. Galeener and Lucovsky [33] have measured the parallel and perpendicular scattering and infrared reflectivity spectra of silica and germania from about 20cm^{-1} to 1500cm^{-1}.

2.3.2 Optical fibre

Note that multimode fibres do not preserve polarization, so that, in the references which follow, the use of a multimode fibre means that the scattering measured is some sort of average of the parallel and perpendicular scattering.

Walrafen [98] has measured the spectra from both a fused silica multimode fibre and a fused silica multimode fibre doped with $\simeq 14\%$ GeO_2 and $\simeq 13\%$ B_2O_3. The spectra extend from about 100cm^{-1} to 4300cm^{-1}. A further paper by Walrafen and Stone [99] compared the relative spectra recorded with bulk samples to the relative spectra recorded with multimode fibres. The bulk samples included fused silica, germania and boric oxide as well as fused silica doped with germania and/or boric oxide. Infrared absorption spectra of the bulk samples were also measured.

Lan, Banerjee and Mitra [49] have measured spectra for multimode fibres from 10cm^{-1} to 3700cm^{-1}. Spectra for the interval 10cm^{-1} to 28cm^{-1} were recorded at elevated temperature (373K) and reduced temperature (238K) as well as at room temperature.

Stolen and Bösch [87] have reported spectra obtained from a multimode silica core fibre at very low temperature (1.5K) and very small frequency shifts (less than 30cm^{-1}). Stolen, Lee and Jain [88] have also reported a spectrum from a single mode polarization preserving fibre for the interval

0cm^{-1} to 1400cm^{-1}.   This would appear to be for parallel scattering, although this is not made clear in the paper.

2.4   Absolute spontaneous scattering spectra in bulk fused silica

Stolen and coworkers [82], [83] have reported measurements of the scattering cross-section (see Section 5.1) in bulk samples of fused silica for frequency shifts from 20cm^{-1} to 1300cm^{-1}. In the first paper, it is not clear if the cross-section is for parallel scattering or depolarized scattering (the average of parallel and perpendicular scattering).   In the second paper it is clear that it is for parallel scattering. The value of the cross-section quoted in the second paper is smaller than the value quoted in the first paper by about a factor of 2.7, but no explanation is given for the discrepancy.

Hellwarth and coworkers [42] have reported absolute scattering spectra for both parallel and perpendicular scattering in five different glasses, including fused silica for frequency shifts from about 20cm^{-1} to 1300cm^{-1} (see also the review article by Hellwarth [43]).

2.5   Stimulated scattering in optical fibres

2.5.1   Experiments where the Raman light grows from the vacuum state

Stimulated Raman scattering was first observed in fused silica optical fibres by Stolen et al. [82].

Rothschild and Abad [72] have illuminated a multimode fibre with an ultraviolet wavelength pump and plotted the Raman power as a function of pump power, but the regime where spontaneous scattering is dominant has not been included.   They have used a fit to the data to deduce a value for the gain coefficient in bulk glass. As well as observing growth from the vacuum of the Stokes peak at a shift of 450cm^{-1}, they also observed growth of another Stokes peak at a shift of 3684cm^{-1}. This is associated with Raman scattering from OH impurities.   A similar experiment has been performed by Pini et al. [69].

Stolen et al. [88] have measured the spectra of Raman light generated in single mode fibres with different pump powers. The spectra are relative (see Section 2.3). An attempt has been made to reproduce the experimental results theoretically.   In the theoretical treatment the temperature of the

fibre is taken as absolute zero and the spontaneous scattering is treated in an approximate fashion ('In single-mode fibers, f can vary between 0.2 and 0.7, depending on wavelength and fiber parameters. For convenience we choose a value of $f = 1/2$.'). Very similar experiments and simulations have been reported using multimode fibres and ultraviolet pumping by Mizunami et al. [59] and Liu and Garmire [50].

More recently, Mahgerefteh et al. [55] have used the dependence of Raman power on pump pulse duration to determine the stimulated gain in a single mode fibre. Their measurement gives the depolarized gain (average of parallel and perpendicular) for frequency shifts from 133cm^{-1} to 533cm^{-1}. In their experiment, dispersion causes the Raman light and pump to walk off from one another after propagation through a certain distance. Varying the pulse duration is therefore equivalent to varying the fibre length. This almost amounts to a pump/signal experiment (see Section 2.5.2), from which the gain is easily deduced, since the Raman light generated at the beginning of the fibre acts as a signal for the remaining length.

2.5.2 Pump/signal experiments

Stolen and Ippen [83] used a pump/signal experiment (one in which both a pump and signal beam are launched into the fibre) to measure the stimulated gain in a single mode fibre at a frequency shift of 330cm^{-1}. Their relationship between the stimulated gain in fibres and the spontaneous cross-section in bulk glass (see Section 2.6) was used to relate the measured gain to the measured bulk cross-section (see Section 2.4). The measurements were found to be in good agreement.

Ikeda [46] has reported a pump/signal experiment using 1.3km of ordinary (not polarization preserving) single mode fibre and wavelengths at about 1μm. Aoki et al. [6] have also reported a pump/signal experiment using a 1.32μm pump wavelength and 3.5km of single mode (not polarization preserving) fibre.

Of particular relevance to this thesis are the papers by Anders Olsson and Hegarty [1], Mochizuki et al. [61] and Aoki [7]. These are all pump/signal experiments using telecommunications band (1.3μm to 1.6μm) wavelengths and ordinary (not polarization preserving) single mode fibres. The lengths of the fibres are 32km for [1], 53km for [61] and 3.5km for Aoki [7]. What makes these papers relevant is that, as well as using the pump/signal technique to measure the gain, the authors have also made measurements with the signal removed and the Raman light allowed to grow from the vacuum state. In all three papers an absolute measurement has been made of this Raman power and the theory of Smith [80] used to compare with a theoretical prediction

based on the measured gain.   [1] and [7] are of particular interest since they have measurements at both low pump powers and high pump powers, spanning the transition from spontaneous to stimulated scattering (in [61] the authors refer to the spontaneous scattered light as 'amplified spontaneous scattering', but actually there is no amplification since the pump powers used are too small for stimulated scattering to be significant).   The agreement between theoretical predictions and experimental results in [1] and [61] is good, while in [7] the Raman light which grows by spontaneous scattering is stronger than theory predicts by a factor of two.

Dougherty et al. [29] have performed a pump/signal experiment in which the bandwidth of the signal was very large (60nm). This allowed determination of the stimulated gain from 6cm^{-1} to 900cm^{-1}. Their experiment used 700m of polarization preserving, single mode fibre, which allowed determination of both the parallel and perpendicular gain.

Stone [90] has investigated Raman scattering from a liquid core fibre (a 5m length of fused silica capillary tube, with inside diameter 5μm, filled with benzene). This paper includes measurement of the Raman power verses the pump power. Although the Raman power is in arbitrary units, and although there are only six data points reported, this is relevant to this thesis since some of the data points are for low pump powers and some for high pump powers and the transition from spontaneous to stimulated scattering is clearly apparent.

2.6   Theory

Stimulated Raman scattering in bulk materials was first observed in 1962 when Woodbury and Ng [102] reported an anomalous spectral line in the output of a Ruby laser, Q switched with a nitrobenzene Kerr cell (this was not identified in the paper as stimulated Raman scattering). Shortly afterwards theoretical treatments were presented by Hellwarth [41] and Shen and Bloembergen [76]. This work was later reviewed by Bloembergen [14]. Experimental tests of the theory have been reported by von der Linde et al. [95]. These papers are not ideal for a discussion of Raman scattering in fibres for two reasons. Firstly, they contain extensive discussion on the propagation of phonon waves. This is irrelevant in the case of Raman scattering from glass where the phonons are assumed to be localized in comparison to the wavelength of light [77]. Secondly, they deal with scattering from materials where the Raman spectrum consists of well defined, narrow peaks, while the Raman spectrum of glass is broad and continuous. Despite these drawbacks, these papers have been widely cited by subsequent authors to justify their

treatment of Raman scattering in fibres.

Stolen et al. [82] have described the relationship between spontaneous and stimulated scattering in bulk glass. Unfortunately, this relationship is not clearly stated with some quantities poorly defined. In a later paper, Stolen and Ippen [83] give the relationship between the stimulated gain in fibres and the spontaneous cross-section in bulk glass. Similar criticism could be made against the presentation in this paper.

Smith [80] has calculated threshold powers for stimulated Raman and Brillouin scattering. The origin of a threshold is that, in order for stimulated scattering to grow, the stimulated gain (see Section 5.3) must exceed the linear loss (see Section 6.5). In the case of Raman scattering, the power of the spontaneously scattered light is calculated under the assumption that the fibre is at absolute zero. That an assumption about the temperature of the fibre has been made is not explicitly stated in the paper. This is unfortunate as the resulting equations have been widely interpreted by other authors as having universal validity. Auyeung and Yariv [9] have essentially repeated Smith's analysis but included the possibility of pump depletion. Dakss and Melman [25] have also essentially repeated Smith's analysis, concentrating on the limit of low pump power (where conversion to Stokes frequencies is small) and approximating the Raman gain spectrum by a Lorentzian rather than rectangular shape.

O'Connor and Tauc [67] have established the relationship between spontaneous Raman scattering in fibres and spontaneous Raman scattering in bulk glass using a classical approach which exploits the known result that the scattered light has nearly zero spatial coherence. (Note that Brinkmeyer [16] has applied the same approach to obtain equations for the backscattered Rayleigh light (see also [64] and [65, Section 5.9.2]). The resulting equations are identical to those for Raman scattering. The validity of these equations has been confirmed in an experiment by Gold and Hartog [35]). One drawback of O'Connor and Tauc's approach is that it does not allow the stimulated scattering to be included to make a unified description (there are also some factors of two which are difficult to interpret correctly). Crosignani et al. [24] have given a fully quantum mechanical treatment which overcomes this difficulty.

More recently Stolen et al. [89] have given Raman equations suitable for the propagation of pulses shorter than the Raman response time (about 1ps). Finally, Headley, III, and Agrawal [39] have shown how spontaneous Raman scattering can be incorporated into the classical framework of the nonlinear Schrödinger equation by adding an appropriate Langevin noise term. In this paper, the temperature dependence of the spontaneous scattering, neglected in Smith's analysis, is restored.

Chapter 3

Some optical phenomena

This chapter gives a brief introduction to some optical phenomena. The list of phenomena is not exhaustive, but is adequate to describe the propagation of kW peak power, visible wavelength laser pulses with durations longer than about 1ps through single mode, fused silica optical fibres. The presentation is aimed at a non-specialist audience.

The phenomena, which include, among other things, dispersion, Raman scattering, self- and cross- phase modulation and four wave mixing, are first described in macroscopic terms. In other words, in terms of the change in energy or the change in propagation velocity of light beams, which is how they are observed in experiments. But there is also an attempt to give some insight into what is going on at a microscopic level, that is in terms of the interaction between the electromagnetic field and the charged particles which constitute atomic matter. The microscopic picture will not be discussed in any detail, indeed some of the concepts may seem rather vague. The objective is only to show how the different phenomena, which may seem quite distinct at the macroscopic level, are actually intimately related, and also to emphasize some concepts, such as energy conservation considerations, which are common to all the phenomena. The concepts are discussed with more rigour for the special case of Raman scattering in Appendix A It is hoped that Appendix A (which presents a complete microscopic theory) will complement the present chapter, allowing the interested reader to construct a full theory for any of the phenomena discussed here only in outline.

A completely quantum mechanical approach will be adopted for the microscopic picture. In fact a full quantum treatment is not strictly necessary to describe the propagation of visible light through glass. The same results are obtained from a semi-classical approach in which the electrons are treated classically while the nuclei and the electromagnetic field are treated using quantum mechanics (the exact opposite of physics circa 1920). Com-

pletely classical models are introduced in one or two places where they offer particular insight.

The organization of the chapter is as follows. Section 3.1 briefly discusses some aspects of the nature of matter in the absence of light and the nature of light in the absence of matter. Discussion of the interaction of light and matter starts in Section 3.2. Note that in Sections 3.2 through to 3.6 it is really the interaction of light with a very small piece of matter (a single source) which is being discussed; how the contribution of the many small sources present in a macroscopic sample of matter are to be summed is deferred until Section 3.7. Classical models are briefly discussed in Section 3.6.

3.1   Light and Matter

3.1.1   Glass and fused silica

In principle, fused (also called vitreous) silica (also called quartz) has the chemical formula SiO_2 (in practice it is impossible to eliminate all impurities and in some contexts the impurities are of central importance). Its structure is that of a covalent macromolecule; each atom in a sample of fused silica is held to every other by a network of covalent bonds. At a length scale of a few atoms, each silicon atom is surrounded by four oxygen atoms, in a tetrahedral geometry. At larger scales the arrangement of the tetrahedra is found to be irregular. Therefore fused silica has some local order but is not a crystal. Such a material is called a glass. Note that silica (SiO_2) is the main constituent of ordinary window glass but that it is possible to make glasses which contain neither silicon nor oxygen. For further discussion, see [54]. Also note that there are crystalline forms of SiO_2.

3.1.2   Electrons and phonons

A detailed description of the nature of matter, in particular how it relates to glass, will be given in Section A.1. For now, it is useful to point out that the electromagnetic field interacts with matter through the oscillatory motion of electric charge (assuming magnetic effects are small and can be neglected). In a molecular gas, such as carbon dioxide, there are at least two sources of oscillatory motion. The first is the electrons. These can make transitions between energy eigenstates, the motion typically involving frequencies greater than that of visible light. The second is the atoms. If these move relative to one another they experience a restoring force due to the presence of the chemical bonding. This means that the atoms can

oscillate about their equilibrium positions. Since the atoms may move in different directions there are usually several vibrational modes. Different vibrational modes have different frequencies because of the different masses and/or chemical bonding. The frequencies are typically much less than that of an optical photon. The amount of energy which can be stored in a vibrational mode is quantized. The lowest energy levels (which are the only ones occupied at room temperature) are found to be equally spaced to good approximation.

In the case of a solid the vibrational modes are called phonon modes and the quanta of energy which can be stored in the phonon modes are called phonons. In a crystalline solid the phonon modes have one significant difference from the vibrational modes in a molecular gas; unlike the modes in a gas, they involve the collective motion of large numbers of atoms, extending over distances which are larger than the wavelength of light. This can make the Raman effect (to be discussed in Section 3.3.4) a more complicated phenomenon in crystalline solids than in gases. In the case of amorphous solids, like glass, it seems that the phonon modes are well localized in comparison to optical wavelengths and the complications disappear; in the context of the Raman effect, the glass appears similar to a molecular gas [77]. In this thesis the term 'phonon' will be used (rather loosely) to encompass both the vibrational quanta in solids and the vibrational quanta in molecular gases.

In glass, the period of oscillation of the electronic motion is of the order 1fs, while the period of the phonon modes is of order 100fs.

3.1.3 Modes of the electromagnetic field

In what follows it will be useful to distinguish between photons in different field modes. The modes are actually the set of orthonormal solutions of the classical wave equation (see Section A.2.1). For the purposes of this chapter the main point is that photons in different modes are distinguishable (they may have different frequency, polarization or propagation direction).

3.2 Single photon processes

These can be described using first order perturbation theory and involve, as the title suggests, just one photon.

3.2.1 Single photon absorption

One of the simplest phenomena that can occur when light propagates through a material, is the absorption of a single photon. This is depicted diagrammatically in Figure 3.1. An electron makes a transition from the ground state $|g\rangle$ to an excited state $|e\rangle$ and a photon of angular frequency ω is destroyed. The probability of such a transition is found to scale linearly with the light intensity. Because of this, single photon absorption comes under the heading of linear optics. In reality the states $|g\rangle$ and $|e\rangle$ may encompass more than one electron, a detail that will be neglected in this chapter.
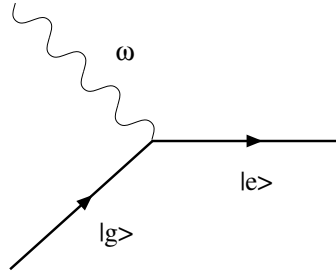
Figure 3.1: Diagram for the absorption of a single photon. The direction of time is from left to right. No particular significance is attached to the vertical dimension. The wavy line represents a single photon. The solid lines denote electronic states. Note that this, and the other diagrams in this chapter, are not really Feynman diagrams, although they will be used for perturbation theory calculations in Appendix A.

For a transition to be probable it must conserve energy to good approximation (this will emerge as a consequence of quantum dynamics in Section A.4.4 and will be a common feature of all the processes discussed in this chapter). This means that the angular frequency of the photon ω must approximately match the difference in angular frequency between ground and excited states $\omega_e - \omega_g$. The band gap in fused silica (difference in energy between ground and lowest excited electronic states) is about 10eV [11, Fig. 7.1], corresponding to an ultraviolet photon of wavelength 124nm. The energy conservation requirement therefore forbids the absorption of visible photons and glass appears transparent.

Figure 3.2 shows a second type of single photon absorption; the annihilation of a photon of angular frequency Ω and the creation of a phonon of angular frequency Ω'. The figure may suggest that the phonon is moving, but this is not necessarily the case (recall from Section 3.1.2 that the phonon may actually be a vibrational quanta localized on a gas molecule).

The phonon modes in glass have about the same frequency as those of infrared photons and glass is found to absorb light strongly at some infrared wavelengths. It is this, combined with the transparency of glass at visible wavelengths, that results in the greenhouse effect.
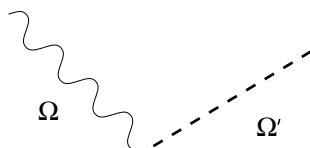
Figure 3.2: Diagram for the absorption of an infrared photon by a vibrational mode. The dashed line is meant to represent the created phonon.

3.2.2 Single photon emission

From the state $|e\rangle$, the electron may decay back to the ground state, emitting a photon (the reverse of single photon absorption). Note that the absorption and subsequent emission are independent events; the state $|e\rangle$ has a finite lifetime and calculations for absorption and emission proceed independently of one another. The emitted photon may not be emitted into the same mode from which it was absorbed. If the photon is emitted into a mode which is devoid of photons then the emission is described as spontaneous. The photon is preferentially emitted into modes which already contain photons. This enhancement is called stimulated emission.

3.2.3 Fluorescence

Fluorescence occurs when the electron which has been excited by single photon absorption to state $|e\rangle$ makes a transition to a second excited state $|f\rangle$ before decaying back to the ground state by single photon emission. If the state $|f\rangle$ has less energy than the state $|e\rangle$, then the energy of the emitted photon will be less than the energy of the absorbed photon. This is called Stokes fluorescence. The opposite case is called anti-Stokes fluorescence.

The fluorescence emission from glass exposed to visible light is extremely weak. However, in spontaneous Raman scattering experiments it can be a significant effect.

3.3   Two photon processes

These require second order perturbation theory and involve two photons.

3.3.1   Two photon absorption

A diagram depicting two photon absorption is shown in Figure 3.3.   The electron starts in the ground state $|g\rangle$ and ends in the excited state $|f\rangle$.   Two photons, with angular frequencies ω_1 and ω_2, are destroyed.   The two photons may come from the same mode or from distinct modes.   The probability of such a transition is found to depend on the product of the intensities of the beams at ω_1 and ω_2.   Because of this, two photon absorption comes under the heading of nonlinear optics.   Such phenomena only became experimentally accessible after the invention of the laser in about 1960.
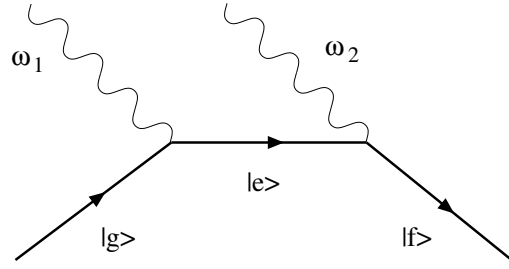
Figure 3.3: Diagram for two photon absorption.   Note that other diagrams are also possible (see text).

The diagram in Figure 3.3 differs from the one in Figure 3.1 in that it contains two vertices (a vertex is a point on the diagram where particles meet).   The state midway along the diagram in which the electron is in excited state $|e\rangle$ and one photon with angular frequency ω_1 has been destroyed is called a virtual state.   The diagram might give the impression that two photon absorption occurs in two steps; the system first making a transition from initial to virtual state, and then making a transition from virtual to final state.   This interpretation is not correct.   There is zero probability that measurement on the system will show it to be in the virtual state.   A correct interpretation of the diagram is that the virtual state provides the coupling necessary for transitions between initial and final state to occur.

As for single photon absorption, two photon absorption will only occur if energy is conserved overall, that is the initial and final state of the matter/light system must have approximately the same energy.   However, the

energy of the virtual state *need not* be the same as the energy of initial and final states. For example, it is *not* necessary that $\omega_1 \simeq \omega_e - \omega_g$. What is true is that, as the difference in energy between initial state and virtual state increases, then transitions become less and less probable. The reason for this will become apparent in Section A.5.1, and it will be a common feature of all the remaining processes discussed in this chapter.

Usually there will be more than one virtual state providing coupling between initial and final states. For example, if the two photons come from distinct modes, then the time order in which the photons are annihilated can be reversed. There may also be excited states other than $|e\rangle$ for the electron. A diagram can be drawn for each virtual state. Calculating the transition rate from initial to final state requires summation over all virtual states. In this respect, the diagrams can help keep track of terms in equations which soon become large and cumbersome. This will be become more apparent in Appendix A.

Neglecting for the moment that there may be excited states other than $|e\rangle$ for the electron, calculation of the transition probability for two photon absorption requires knowledge of the dipole moment between states $|g\rangle$ and $|e\rangle$ and states $|e\rangle$ and $|f\rangle$. Exactly what this quantity is will be explained more fully in Section A.11. A crucial point is that the dipole moment between $|g\rangle$ and $|e\rangle$ also appears in the probability for an electron to make a transition from $|g\rangle$ to $|e\rangle$ by the absorption of a single photon of angular frequency approximately $\omega_e - \omega_g$ (see Section 3.2.1). It is therefore possible, at least in principle, to predict the outcome of experiments in nonlinear optics entirely from data acquired in linear optics experiments. In practice, the presence of many excited states for the electron, in addition to the state $|e\rangle$, and the need for single photon absorption data for all of them, usually makes this forbiddingly difficult.

In fused silica optical fibres, germania is often added to the core region (see Section 4.10) to increase the refractive index. The presence of germania results in electronic levels about 5eV above the ground state energy. Electrons can be excited to these levels by the single photon absorption of ultraviolet light. Atkins [8] has measured the single photon absorption spectra of germania doped fibres and observed absorption bands at 330nm and 240nm, corresponding to electronic levels 3.8eV and 5.2eV above the ground state respectively, as well as absorption bands at shorter wavelengths. Note that there is some disagreement between Atkins' results and those in an earlier paper by Williams et al. [100]. The 5.2eV level can also be accessed by two photon absorption. Mizunami et al. [60] have measured the two photon absorption cross-section of a germania doped fibre at wavelengths of 440nm, 480nm, 520nm and 560nm. When electrons are excited to the 5.2eV

level, the bonding in the glass is no longer stable, the atoms rearrange and
the glass experiences a permanent change in chemical structure. This in
turn changes the optical properties of the glass (in particular its refractive
index). This is called photosensitivity and it can be useful for the fabrication
of fibre components (for review articles on photosensitivity see [44], [66], [70]
and [74]). The literature is less informative about the effects of excitation
to the 3.8eV level. In fact there are no reports of photosensitivity due to
absorption of 330nm light, and no reports of two photon absorption of red
light to this level. In this thesis an attempt was made to avoid photosen-
sitivity by using red (647.1nm) light from a krypton laser in preference to
green (514.5nm) light from an argon laser (this also had the advantage that
single mode fibres are easier to obtain for the red wavelengths thanks to the
prevalence of HeNe lasers operating at 632.8nm). However, some photosen-
sitivity was observed in one fibre (an elliptical core fibre made by the Andrew
Corporation). Photosensitivity will not be discussed further in this thesis.

3.3.2   The linear refractive index and dispersion

Figure 3.4a depicts a process in which an electron starts and finishes in its
ground state, a photon ω_1 is destroyed, and a second photon ω_2 created. As
discussed in Section 3.2.1, such a process will only occur if the energy of
initial and final states of the system are approximately the same. This will
certainly be the case if the photons are absorbed and re-emitted into the
same mode, since that will make the initial and final states the same. It is
this case that will be discussed in this section.

(a)   (b)
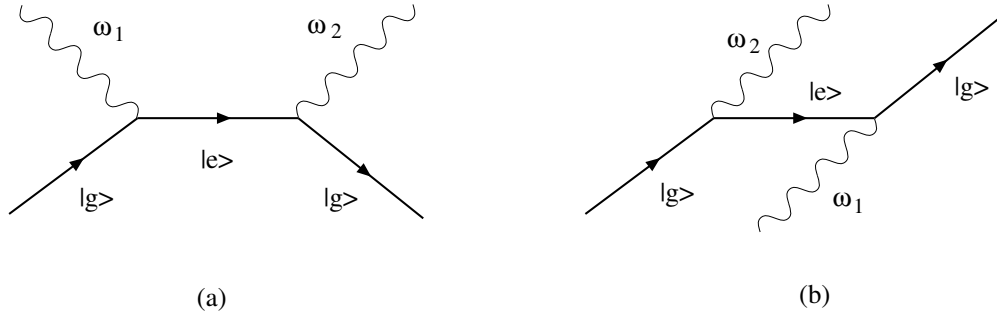
Figure 3.4: These diagrams contribute to either the linear refractive index or Rayleigh
scattering, depending on whether photons are being absorbed and then re-emitted into
the same mode, or being transferred from one mode to another.

If the system starts and finishes in the same state, then it no longer makes

sense to talk about transitions.   However, the coupling to the virtual state still has an important consequence; it decreases the energy of the system. The Schrödinger equation (Eqn A.7) shows that a decrease in energy will result in a reduction in frequency.   For the light this will mean a reduction in phase velocity (the wavelength is an invariant which is determined by the field mode).   Note that this does not mean that a light beam changes in frequency when it passes from vacuum into a material.   The correct interpretation is that, if a standing light wave could be confined between two lossless mirrors in a vacuum and all optical sources removed, then the addition of material into the region between the two mirrors would result in a reduction in the frequency of the light (with no change in wavelength).

So Figure 3.4a is responsible for the reduction in the speed of light associated with the usual refractive index (and hence Snell's law bending, Fresnel reflections, and so on).   Actually this is only partly true.   A second diagram also contributes.   This is shown in Figure 3.4b (there is also the requirement of summing over all excited electronic states).   Note that the difference in energy between virtual and initial/final states is always going to be larger for Figure 3.4b than Figure 3.4a, so Figure 3.4b will make a smaller contribution to the refractive index (for a discussion of the energy mismatch, see Section 3.3.1).   In the case of glass and visible light, the energy mismatch for the dominant diagram, Figure 3.4a, decreases as the wavelength of the light decreases from red through to blue.   Hence, the reduction in speed is larger for blue light than red light and the propagation of light through glass is dispersive.

3.3.3   Rayleigh scattering

In Figures 3.4a and 3.4b, it is not necessary to have the photons absorbed and emitted into the same mode to satisfy overall energy conservation.   The angular frequency of the two photons simply has to be approximately the same.   If different modes are involved then the two diagrams depict Rayleigh scattering; the elastic scattering of a photon.   Note that Rayleigh scattering can change the direction of light in ways which are inconsistent with geometrical optics.

As described in Section 3.3.2, Figure 3.4a will make a greater contribution to Rayleigh scattering than Figure 3.4b.   Also, in the case of glass, the probability of scattering for blue light is greater than the probability of scattering for red light, because, in the case of blue, the energy of the virtual state is closer to the energy of the initial/final states.   The lowest excited states for the electrons in air molecules are at similar energies to those in glass, so, in air, blue light also scatters more strongly than red.   This is the

primary reason for the characteristic blue colour of the sky.

3.3.4   Raman scattering

Figure 3.5 shows a diagram in which a photon ω_1 is destroyed and a photon ω_2 created. One of the electronic states is the ground state, but this need not be the case. Overall energy conservation requires that $\omega_2 \simeq \omega_1 - (\omega_f - \omega_g)$. This diagram contributes to the inelastic scattering of a non-relativistic photon, a phenomenon called Raman scattering. In particular, this diagram contributes to Stokes (scattered photon has less energy than incident photon), electronic (matter absorbs energy by a change in electronic state) Raman scattering.
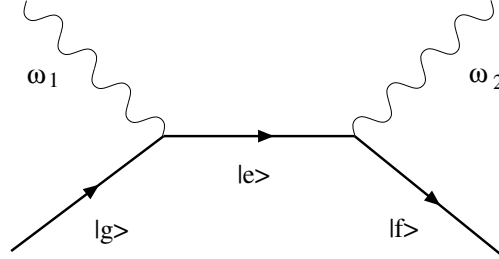
Figure 3.5: One of the diagrams which contribute to electronic Raman scattering.

Other types of scattering are also possible. For example, polyatomic gas molecules can absorb energy by a change in rotational state (called rotational Raman scattering). What is of interest in this thesis is vibrational Raman scattering, where the photon energy is absorbed into the vibrational motion of the atoms. All four diagrams which contribute to Stokes vibrational Raman scattering are shown in Figure 3.6 (all diagrams are drawn because they will be needed in Appendix A). Note that, since both infrared absorption (see Figure 3.2) and Raman scattering involve interaction with the vibrational motion, there is some relationship between the two processes.

In the diagrams in Figure 3.6 the electron starts and finishes in the ground state and a phonon Ω is created. Overall energy conservation requires that $\omega \simeq \omega_p - \Omega$. The angular frequency of the scattered photons is therefore determined by the angular frequency of atomic vibrations. In Raman spectroscopy, the light is resolved into its frequency components. The intensity of light as a function of frequency is called the Raman spectrum. In the case of glass there are vibrational modes at almost all frequencies, so the Raman spectrum appears broad and continuous.
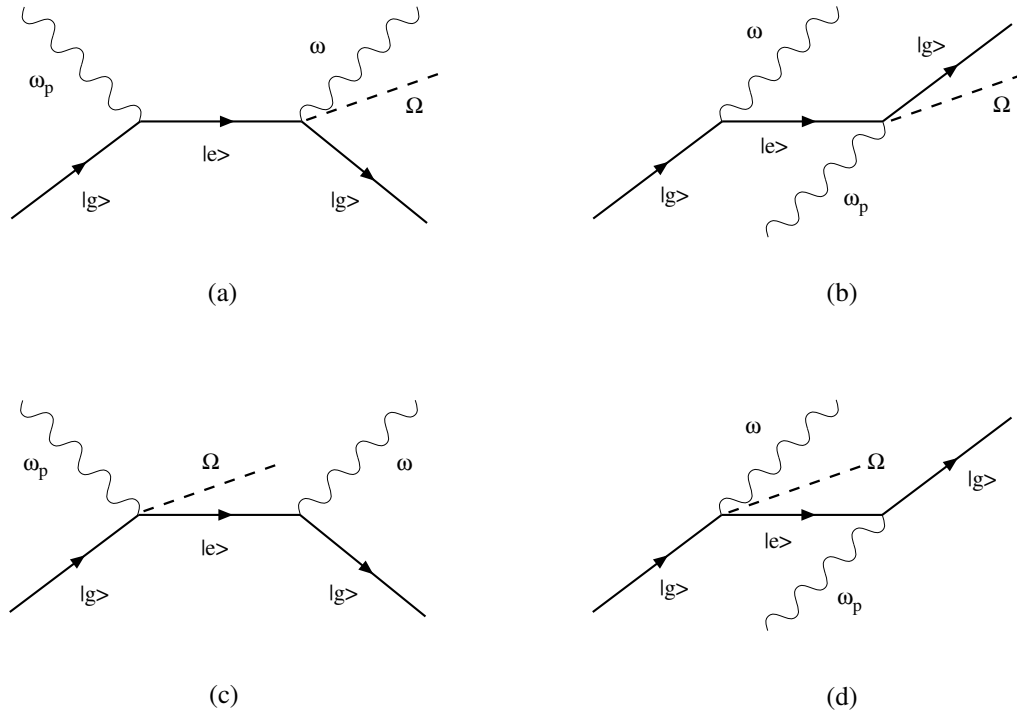
Figure 3.6: Neglecting the possibility of other excited electronic states, this is the complete set of diagrams which contribute to Stokes vibrational Raman scattering.

If the mode ω is initially empty of photons then the scattering is described as spontaneous. If the mode ω already contains some photons then the probability of scattering is enhanced. This is called stimulated scattering (the terminology parallels that for emission; see Section 3.2.1).

Some of the remarks made about Rayleigh scattering are also relevant here. The diagrams on the left, Figures 3.6a and 3.6b, make a greater contribution than the diagrams on the right. In glass, if the incident photon is of blue wavelength then it is more likely to Raman scatter than if it is of red wavelength. In practical terms, Raman scattering is almost always orders of magnitude weaker than Rayleigh scattering. The probability for an optical photon to Stokes Raman scatter during propagation through a 1m thickness of glass is of the order 10^{-4} (using data from [42]).

If in Figure 3.6, phonons are destroyed at vertices rather than created, then the diagrams become the four possible diagrams for anti-Stokes Raman scattering. The comments which have been made thus far for Stokes scattering can be adapted to the case of anti-Stokes scattering. For example, if mode ω is initially empty of photons then the scattering is described as spontaneous. In practice, spontaneous anti-Stokes scattering is always weaker than spontaneous Stokes scattering because it requires phonons to be available from thermal excitation of the material. Note that if ω_p and ω both contain photons then the overall transfer of photons between the two modes is obtained by summing the contributions of spontaneous and stimulated Stokes and spontaneous and stimulated anti-Stokes. If the number of photons in both modes is significantly greater than one, a net transfer of photons from the high frequency mode to the low frequency mode is guaranteed to occur.

3.3.5   Time response of Rayleigh and Raman scattering

If a laser pulse propagates through a piece of glass there is some probability that a photon Rayleigh scatters and some probability that a photon Raman scatters. The probability for Rayleigh scattering is found to be independent of the pulse duration. The probability for Raman scattering is found to be independent of the pulse duration only for pulses longer than about 500fs. Rayleigh scattering involves only the electrons and these have oscillation periods of about 1fs (see Section 3.1.2). In comparison to this, the intensity of even the shortest laser pulses is slowly varying in time. As will become clear in Section A.5.1, this is sufficient to make the scattering probability independent of pulse duration. On the other hand, Raman scattering also involves the phonons and these have oscillation periods of about 100fs. Hence if the pulse becomes shorter than about 500fs, the intensity of the pulse can no

longer be considered slowly varying and the probability for Raman scattering starts to become dependent on pulse duration.

Note that in scattering there is essentially no time delay between destruction of the incident photon and creation of the scattered photon. This is in contrast to the situation in fluorescence where there is always a time delay between absorption of the incident photon and emission of the fluorescence photon, although, in some cases, the time delay can be difficult to detect experimentally.

3.4 Three photon processes

These require third order perturbation theory and involve three photons.

3.4.1 Second harmonic generation

The diagram in Figure 3.7 is one possible diagram for a process in which photons ω_1 and ω_2 are destroyed and ω_3 created. Since the electron starts and finishes in the same state, overall energy conservation requires that $\omega_3 \simeq \omega_1 + \omega_2$. The process is called sum frequency generation. In the special case where $\omega_1 = \omega_2$ (the two photons need not come from the same mode) the process is called second harmonic generation (SHG). Like two photon absorption, the transition probability depends on the product of the intensity of the two beams ω_1 and ω_2, and SHG is only observed using the intense beams from laser sources.
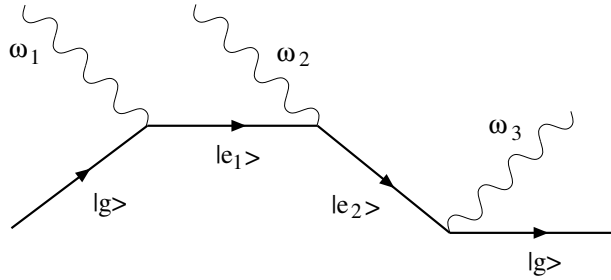
Figure 3.7: One of the diagrams which contributes to sum frequency generation (second harmonic generation if $\omega_1 = \omega_2$).

From a theoretical point of view, SHG is not expected to occur in materials like glass which have inversion symmetry (this will be discussed briefly in Section 3.7.4). However, when optical fibres are exposed to high peak

power pulses, the symmetry is somehow broken and SHG is observed to oc-
cur. The exact mechanism by which the symmetry is broken is still contested
(for recent discussion see [3], [4] and [21]).

More than ten years ago Valk et al. [93] observed SHG in fibres pumped
with a mode locked Kr^+ laser, operating with a wavelength of 647.1nm (the
same laser system used in this thesis). SHG was also observed in fibres during
the course of this thesis. Actually, this is not strictly correct; the presence of
SHG was inferred by the presence of fluorescence. The fluorescence spectrum
consists of at least two very broad peaks. One covers all the blue wavelengths
and extends into the green. The other starts in the red and extends into the
near infrared. Fibres from Andrew (elliptical core polarization maintaining
fibre type 48280-633S-1) and York (bow tie structure high birefringence fibre
type HB600, purchased through Newport) were found to fluoresce strongly.
Fibre from 3M (FS-SN-3224) fluoresced much more weakly. No fluorescence
was observed in the fibre manufactured by Stolen (see Section 7.4) although
this might not exclude the presence of SHG.

3.5   Four photon processes

These require fourth order perturbation theory and involve four photons.

3.5.1   Nonlinear refractive index and self- and cross-phase modulation

Figures 3.8a and 3.8b both depict a process in which photons ω_1 and ω_2 are
destroyed and photons ω_3 and ω_4 created. The matter starts and finishes in
the same state. There are really two classes of diagrams which contribute
to this same process. Figure 3.8a is an example from the first class and Fig-
ure 3.8b and example from the second class. Other diagrams are obtained, as
usual, by interchanging the time order in which the photons appear and/or
substituting different excited states for the electrons. The significance of
having two classes of diagrams contributing to the same process will be dis-
cussed in 3.5.3. In this section (and Section 3.5.2) the distinction between
the two classes of diagrams will not feature.

As for two photon absorption and second harmonic generation, the prob-
ability of such a process depends on the product of the intensities of beams ω_1
and ω_2, so the process will only be observable using the intensities available
from laser sources.

Overall energy conservation requires that $\omega_3 + \omega_4 \simeq \omega_1 + \omega_2$. This will
certainly be true if all four photons are absorbed/emitted into the same
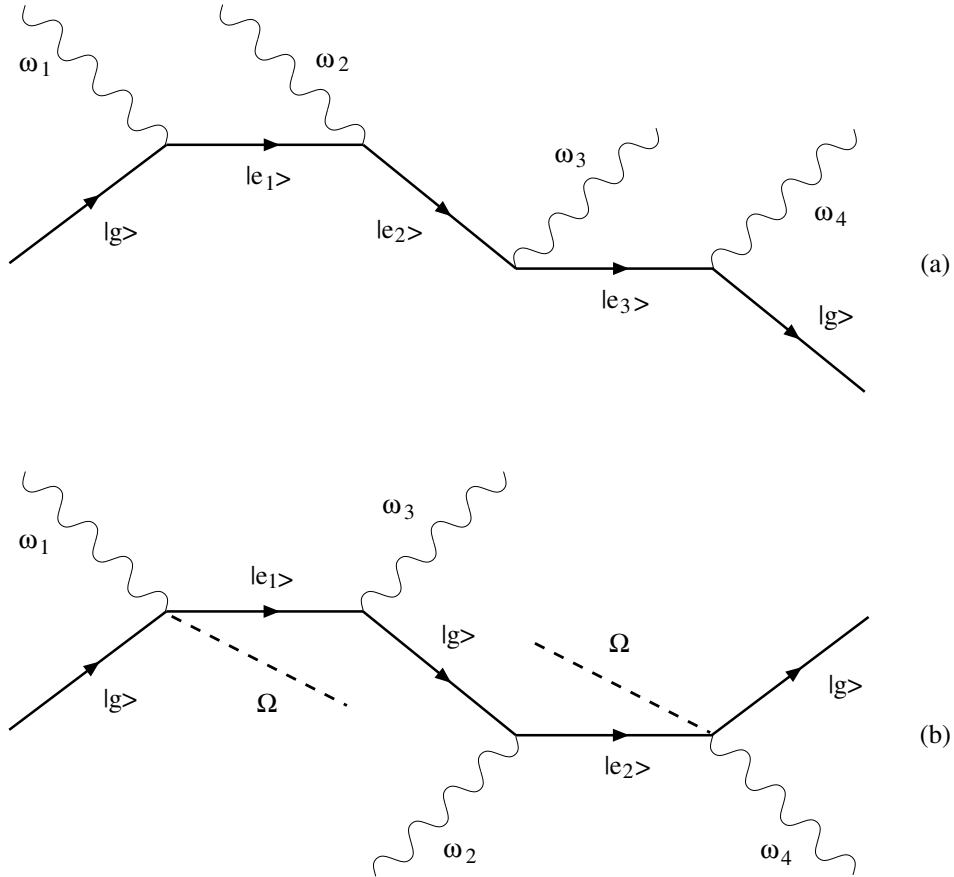
Figure 3.8: Examples of diagrams in which two photons are destroyed and two created. (a) A diagram which contributes to the electronic nonlinearity. (b) A diagram which contributes to the nuclear nonlinearity.

mode. In this case it no longer makes sense to talk about transitions since the light/matter system starts and finishes in the same state. The situation is similar to that discussed in Section 3.3.2 for the linear refractive index. Indeed, in this case the presence of the interactions in Figures 3.8a and 3.8b result in a reduction in the energy of the system and hence a further reduction in the speed of light. A more detailed analysis reveals that the reduction in speed depends on the intensity of light in the mode. In other words there is an intensity dependent refractive index. If the light intensity varies in time, this nonlinear refractive index can lead to the generation of new frequency components. This is actually quite difficult to explain in a quantum mechanical picture, but the basic mechanism resembles the example given in Section 3.3.2 of the standing wave between two mirrors, except that the refractive index is being changed by the changing intensity of the light rather than the addition of material into the cavity. The effect is called self-phase modulation. Agrawal [5] gives a good classical description.

Energy will also be conserved if photons ω_1 and ω_3 are absorbed/emitted into one mode (denoted by ω_1) and photons ω_2 and ω_4 are absorbed/emitted into a second mode (say ω_2). Consider the case where the light in ω_1 is of high intensity and the light in ω_2 of low intensity. Following the argument used in the previous paragraph, ω_2 will experience a change in refractive index due to the intensity of light in ω_1. If the intensity in ω_1 is varying in time then this will lead to the generation of new frequency components in ω_2. This is called cross-phase modulation and is also discussed by Agrawal [5].

3.5.2   Four wave mixing

In Figures 3.8a and 3.8b the photons may be emitted into different modes from which they were absorbed. The diagrams then describe true scattering. This scattering encompasses quite a number of phenomena which are only really superficially different from one another. For example, they may differ because they involve incident beams of identical wavelength as opposed to distinct wavelength, or they may differ in how phase matching (to be discussed in Section 3.7.5) is achieved. Common names encountered for the phenomena (and, unfortunately, different authors often use different names for the same phenomena) include four wave mixing, modulational instability, $\chi^{(3)}$ parametric amplification and, in the case where photons ω_1 and ω_2 come from the same mode, three wave mixing.

3.5.3 Electronic, nuclear and electrostrictive nonlinearity

The class of diagrams of which Figure 3.8a is an example, constitute what is called electronic nonlinearity. Similarly the class of diagrams of which Figure 3.8b is an example, constitute nuclear nonlinearity. As for Rayleigh and Raman scattering, the two nonlinearities have different time responses (see Section 3.3.5). The electronic nonlinearity is independent of pulse duration (assuming peak intensities stay the same) while the nuclear nonlinearity is only independent of pulse duration for pulses longer than about 500fs.

In experiments on nonlinear refraction or four wave mixing, involving pulses longer than about 500fs, it is not possible to separate the contributions made by electronic and nuclear nonlinearity. Rather, the only measurable quantity is the total nonlinearity, the sum of electronic and nuclear terms. However, note that Figure 3.8b looks like two Raman scattering diagrams (Figure 3.6) which have been concatenated. Hellwarth [42] and [43] has used this to infer the strength of the nuclear nonlinearity from spontaneous Raman scattering measurements. This is analogous to using measurement of single photon processes to predict the outcome of experiments involving two photon processes, as discussed in Section 3.3.1. In the case of fused silica, experiments by Hellwarth show that the electronic nonlinearity accounts for about 80% of the nonlinearity and nuclear nonlinearity the remaining 20%.

In optical fibres there is a third contribution to the nonlinear refractive index. Diagrams like Figure 3.4 not only influence the light, they also result in physical force acting on the glass. In the case of optical fibres, the very large intensity gradient in the xy plane (see Figure 4.1a) results in a compression of the core. This then changes the linear refractive index. The effect is called electrostriction and it is closely related to Brillouin scattering. The time scale for the electrostrictive nonlinearity is determined by the time it takes a sound wave to cross the fibre core. For pulses shorter than about 500ps, there is no spatial overlap between the pulse and the acoustic disturbance it generates. As a consequence the electrostrictive nonlinearity is negligible. For some recent data on electrostriction in fibres see [17], [18], [32] and [57].

3.6 Classical models

In this section the electrons will be treated as if they are charges held to the atoms by springs. The atoms will likewise be treated as if they are held to one another by springs. Both electrons and the atoms will be assumed

to obey Newton's laws of motion. Light will be treated as a classical wave whose energy can vary continuously.

3.6.1   Linear refractive index and Rayleigh scattering

If a light beam of angular frequency ω propagates through a material, the associated electric field will exert an oscillating force on the electrons. If the light beam is not too intense, and if the presence of the vibrational modes can be ignored, then the springs binding the electrons will behave as linear springs and the electrons will oscillate in sinusoidal motion, also at angular frequency ω. These oscillating electrons will act as a source of electromagnetic waves, again at angular frequency ω, which can spread out in all directions (actually in a dipole radiation pattern [40]). The waves emitted by different electrons interfere with one another. This will be discussed more fully in Section 3.7. The result is that a small amount of the total reradiated light has the dipole radiation pattern. This accounts for Rayleigh scattering. The remainder of the reradiated light is emitted in the same direction as the incident beam, but with a change in phase (if the motion of the electrons is damped, they will not oscillate in phase with the driving force). This phase shift accounts for the slowing down of the light, and hence the linear refractive index.

3.6.2   Raman scattering

In the classical model of Raman scattering, the strength of the spring holding an electron to an atom is assumed to depend on the position of the atom. If the atom is in vibrational motion with angular frequency Ω, then the spring constant is modulated at angular frequency Ω. If a light wave of angular frequency ω propagates through the material, the electron will oscillate in an amplitude modulated sinusoidal motion. The radiation generated by the electrons will therefore also be amplitude modulated. The angular frequency of carrier and modulation are ω and Ω respectively, so the radiation had components at $\omega \pm \Omega$, accounting for Stokes and anti-Stokes Raman scattering.

3.6.3   Electronic nonlinearity

The atomic motion is not important in the origin of electronic nonlinearity and can be neglected. If the incident light is sufficiently intense, then the springs holding the electrons to the atoms no longer behave as linear springs. This has two consequences. Firstly, the amplitude of motion of the electrons is no longer proportional to the amplitude of the incident light. This accounts

for the intensity dependent refractive index. Secondly, each electron/spring system no longer obeys the principle of superposition. This means that if two light beams with angular frequencies ω_1 and ω_2 are incident on the material, then the motion of an electron will have components at ω_1 and ω_2 and other angular frequencies as well. This accounts for four wave mixing.

3.6.4 Nuclear nonlinearity

This can be understood by returning to the scenario where the spring binding an electron behaves as a linear spring with a spring constant that depends on the position of the atoms. In such a system, an incident beam of light is able to exert force on the atoms by an indirect coupling through the electronic motion. If the light is sufficiently intense, the atoms will move. This in turn changes the amplitude of motion of the electrons and hence the refractive index. Because the effect is nonlinear, four wave mixing also results.

3.7 Emission from multiple sources

A macroscopic piece of material contains many microscopic sources (for the purposes of this chapter, these sources are assumed to be individual electrons; see Section 3.2.1). This section deals with how the radiation produced by the many sources is to be added together.

Before going further it is useful to reiterate the results of Young's double slit experiment. In a classical picture [40] each slit is a source of waves. If the two sources are mutually coherent (have the same frequency and a fixed phase relationship) then the waves from each source must be added coherently (the amplitudes of the waves are added). At some points on the screen, the two waves arrive in phase and the result is constructive interference. At other points on the screen, the two waves arrive in anti-phase and the result is destructive interference. The overall result is a pattern of fringes. If the two sources are mutually incoherent then the waves from each source are added incoherently (the intensities are added). No fringes result.

A difficulty for the classical picture is that interference still arises even if there is only a single photon incident on the slits. In a quantum mechanical picture [12] the interference arises because the same final outcome (the detection of a photon at a point on the screen) can be reached by more than one (in this case two) alternative pathways (the photon may go through one slit or the other). The phrase 'same final outcome' has a deep significance here. Since all pathways lead to the same final outcome, the system contains no record of which pathway was actually followed. If the experiment

is modified so that there are multiple outcomes, one for each pathway, then it is possible to determine which pathway was followed, but any interference is completely destroyed.

3.7.1   Linear refractive index and Rayleigh scattering

To begin with a classical picture, suppose that a light beam propagates through a material. In order to be a beam with a well defined propagation direction, the light waves must be spatially coherent over distances of a few wavelengths and temporally coherent over time scales of a few optical periods. The beam will drive the electrons into sinusoidal motion (see Section 3.6.1). Because of the coherence of the beam, the motion of any two electrons will have a fixed phase relationship provided they are located within a few wavelengths of one another. The electrons within small volumes therefore act as mutually coherent sources. For a homogeneous material (one which is invariant under translation in space), it can be shown that the summed emission from these electrons is perfectly destructive in all directions except one, namely the direction in which the original beam was propagating. In other words, the linear refractive index will arise but there will be no Rayleigh scattering. In practice, no material is perfectly homogeneous, the interference is not perfectly destructive, and Rayleigh scattering does occur. By increasing the material disorder, the strength of Rayleigh scattering can be increased.

The quantum mechanical picture of the Rayleigh scattering of a single photon is also analogous to the double slit experiment. There are multiple pathways (the scattered photon may have come from any of the electrons in the material) and these all lead to the same final state. Note that the final state is independent of pathway because, in the diagrams for Rayleigh scattering, the material starts and finishes in the same state (see Figure 3.4). Interference between the pathways can therefore occur. For a perfectly homogeneous material, destructive interference forbids the photon being absorbed from one mode and emitted into another, and there will be no Rayleigh scattering.

3.7.2   Brillouin scattering

When a sound wave propagates in a material it generates regions of compression and rarefaction, increasing the material disorder. The density fluctuations associated with the sound wave are time dependent, cycling with the frequency of the sound. According to Section 3.7.1, the additional density fluctuations are expected to increase the strength of Rayleigh scattering.

Because the disorder is time dependent, the scattered light is shifted in frequency by the frequency of the sound wave. This is the same amplitude modulation effect described in Section 3.6.2 for Raman scattering.

The scattering of light by sound waves is called Brillouin scattering. In optical fibres the effect can be very strong because the scattered light interferes with the original beam to generate a spatial modulation in intensity. This can then act to amplify the sound wave by the elasto-optic effect (electrostriction; see Section 3.5.3). Hence there is positive feedback inherent in the dynamics. On the other hand, the effect tends to be strongly suppressed if the linewidth of the optical beam exceeds about 100MHz [82]. The lasers used in this thesis had such linewidths so Brillouin scattering will not be discussed further.

3.7.3 Raman scattering

The situation in Raman scattering is completely different. Beginning with the classical picture, and referring closely to Section 3.6.2, the Stokes Raman radiation at $\omega - \Omega$ emitted by an electron has a phase which depends on both the phase of the carrier (incident light beam) and the phase of the modulation (phase of the atomic vibration). Since the phase of the atomic vibration differs from one atom to another, there is no fixed phase relationship between the Stokes radiation emitted by different electrons. The different electrons therefore act as mutually incoherent sources and there is no interference. Exactly the same is true for anti-Stokes scattering. The strength of Raman scattering is independent of the disorder of the material.

The absence of interference can also be understood in quantum mechanical terms. If a single photon is Raman scattered there are multiple pathways (the photon may have come from any of the electrons). But the final state is not independent of pathway. One of the vibrational modes will have gained (or lost) a phonon (see the diagrams in Figure 3.6). By measuring the number of phonons in each vibrational mode before and after the scattering event, the pathway followed can be unambiguously identified. Therefore there will be no interference.

The lack of interference between multiple sources in the Raman effect follows from the assumption that the vibrational modes of the atoms are in thermal equilibrium. In the classical picture this ensures that the motion of one atom has a random phase in relation to the motion of other atoms. In the quantum picture it ensures that the vibrational modes are in energy eigenstates, each with a well defined number of phonons. But in a Raman scattering experiment, the scattering does change the state of the atomic vibrations. It is therefore conceivable that an experimental regime might

exist in which the atomic vibrations are driven out of thermal equilibrium. If the vibrations could be driven into coherent motion, interference between different sources would become possible, and further Raman scattering would exhibit a fundamental change in behaviour. (In the quantum picture, coherent motion means that the number of phonons in a vibrational mode is no longer well defined, and, as a consequence, the phonon modes can no longer be used to identify the source of a Raman scattered photon.) The author is not aware of any discussion in the fibre optics literature about this assumption of thermal equilibrium, in particular there seems to be no attempt, either theoretically or experimentally, to identify the experimental regime where it might be expected to break down.

3.7.4 Second harmonic generation and inversion symmetry

At a distance scale of a few atoms, fused silica lacks inversion symmetry (is non-centrosymmetric). For example, a 10nm cube of fused silica would be non-centrosymmetric and therefore suitable for SHG. Larger 100nm cubes of fused silica (which are still small in comparison to the wavelength of light) will contain non-centrosymmetric 10nm units and their inversion twins. The SHG emission of each unit cancels the emission of its inversion twin. Hence glass is not expected to be suitable for SHG even though it lacks inversion symmetry at very small length scales.

3.7.5 Four wave mixing and phase matching

The diagrams for four wave mixing (Figure 3.8) are similar to those for Rayleigh scattering (Figure 3.4) in that the material starts and finishes in the same state. Interference between the microscopic sources therefore occurs. In some materials, it is possible to find modes for the four beams ω_1, ω_2, ω_3 and ω_4, such that the contribution of all sources adds constructively. This is called phase matching.

Chapter 4

Optical fibres

What is of interest in this thesis is step index, single mode fibres. There is already an excellent body of literature dedicated to the theory of light propagation in these fibres and their properties so only a brief summary will be given here. In preparing this chapter, the book by Neumann [65] was influential.

4.1 Structure

A single mode optical fibre is a thin (typically 125μm diameter) cylindrically shaped rod made from a highly purified glass (fused silica; see Section 3.1). Such a fibre is shown in a coordinate frame in Figure 4.1a. Let r be given by

$$r = \sqrt{x^2 + y^2}. \tag{4.1}$$

In other words r is the distance from the centre of the fibre in a radial direction. Dopant chemicals are added to the glass with a concentration that depends on radial distance, forming a refractive index profile in the radial direction. The profile is approximately that of a step (see Figure 4.1b). In a step index profile there are two distinct regions; a central region called the core (approximately 5μm in diameter for visible light propagation in single mode fibres) and the surrounding region, which is called the cladding. The core has a refractive index which is slightly greater ($\lesssim 1\%$) than the cladding. When light propagates down the rod there is typically 80% of the optical power in the core and the remaining 20% in the cladding. The refractive index profile results in a focussing effect which balances diffraction and the light propagates without diverging.

4.2   Transverse mode profile

An important concept in this thesis is the transverse mode profile. This is a function $f(x,y)$. For fixed z, the electric field amplitude at point (x,y,z) of a beam of light propagating down the fibre is proportional to $f(x,y)$. Note that $f(x,y)$ is a slowly varying function of the angular frequency of the beam. In this thesis the convention will be adopted that the transverse mode profile is normalized such that

$$\int_{-\infty}^{\infty} dx \int_{-\infty}^{\infty} dy \ |f|^2 = 1. \tag{4.2}$$

4.3   Cut-off wavelength

In step index fibres there is a cut-off wavelength (those involved in the manufacture of fibres have adopted the convention of using wavelength rather than angular frequency). For wavelengths longer than this cut-off wavelength, only one transverse mode profile is possible and, neglecting two orthogonal polarization states, the fibre is truly single mode.

4.4   Gaussian approximation

In step index fibres there is a wavelength range (which happens to coincide with the regime of typical operation) for which the transverse mode profile is Gaussian to good approximation. $f(x,y)$ is then given by

$$f(x,y) = \sqrt{\frac{2}{\pi}} \frac{1}{\hat{r}} \, e^{-\left(\frac{r}{\hat{r}}\right)^2} \tag{4.3}$$

where r is given by Equation 4.1 and $\hat{r}$ is called the spot size or, alternatively, the mode field radius. For a beam of light with angular frequency ω, the spot size is found to be approximately proportional to $1/\omega$

$$\hat{r}(\omega) \propto \frac{1}{\omega}. \tag{4.4}$$

Neumann [65, pg 74 and Table 5.1] gives some data for the validity of this approximation. For a step index fibre with a single mode cutoff at 550nm, the wavelengths 575nm and 775nm correspond to normalized frequencies (normalized frequency is often denoted V) of 2.3 and 1.7 respectively. Over this range of normalized frequencies, Equation 4.4 holds to within 3%.

4.5 Far field divergence angle

When light reaches the end of the fibre, approximately 4% is reflected (due to the index difference between air and glass) and the remaining light diffracts freely into the air (see Figure 4.2). The mode function f can be recovered exactly using an inverse Hankel transform of the far field transverse intensity profile [2]. However, since the transverse mode profile inside the fibre is approximately Gaussian, the transverse mode profile after the fibre will also be approximately Gaussian. The far field transverse intensity profile can then be related to the mode field radius using Gaussian beam propagation [103]. In the far field (for distances z greater than $\pi \hat{r}^2/\lambda \simeq 0.1$mm) the divergence angle θ is related to the mode field radius by

$$\theta = \frac{\lambda}{\pi \hat{r}} \,.$$

(4.5)

Here λ is the free space wavelength of the light.

4.6 Polarization preserving fibres

In high birefringence (HiBi) fibres, the cylindrical symmetry of the fibre is broken. The core may have an elliptical rather than circular cross-section or stress elements may be placed in the cladding. In either case the fibre then exhibits linear birefringence with two eigenaxes; a fast axis and an orthogonal slow axis. Light incident linearly polarized along the fast axis will remain on the fast axis as it propagates (and likewise for the slow axis). If light is incident on the fibre linearly polarized at 45^0 to the eigenaxes, then its polarization evolves under propagation. This evolution is periodic with distance. The distance required for evolution through a single cycle is called the beat length L_b.

It is also possible to make fibres with circular birefringence by twisting them, but these will not be considered in this thesis.

4.7 Gaussian approximation for HiBi fibres

In the case of HiBi fibres, the transverse mode profile may not have circular symmetry. It is then more appropriate to use

$$f\left(x, y\right) = \sqrt{\frac{2}{\pi}} \, \frac{1}{\sqrt{\hat{x}\hat{y}}} \, e^{-\left(\frac{x^2}{\hat{x}^2} + \frac{y^2}{\hat{y}^2}\right)}$$

(4.6)

in place of Equation 4.3. In Equation 4.6, $\hat{x}$ and $\hat{y}$ specify the mode field radii in the x and y directions respectively.
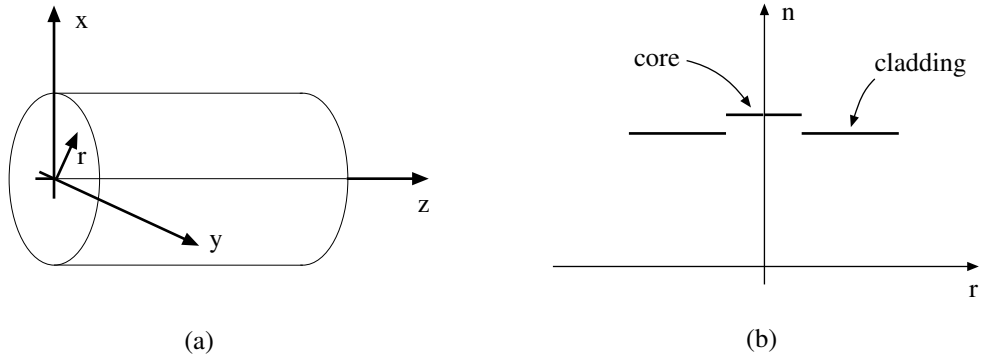
Figure 4.1: (a) An optical fibre in a coordinate frame. (b) The refractive index profile for a step index fibre.
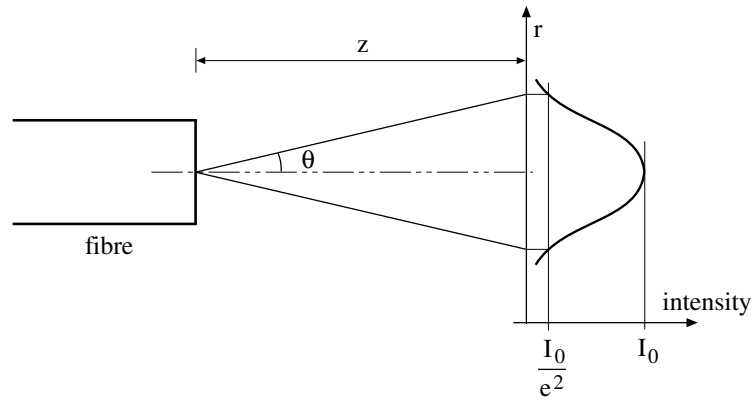
Figure 4.2: Light diffracting from the end of a single mode fibre.   The graph shows the transverse intensity profile at a distance z from the fibre end.

4.8 Effective area

If f_p is the transverse mode profile of a beam, and f the transverse mode profile of a second beam, then a quantity which appears in equations for light scattering between the two beams is the effective area of overlap between the two beams, A_{eff}, defined by

$$\frac{1}{A_{\text{eff}}} = \int_{-\infty}^{\infty} dx \int_{-\infty}^{\infty} dy \; |f_p|^2 \; |f|^2 \, . \tag{4.7}$$

Note that A_{eff} does have dimension area because of the normalization of f_p and f (Equation 4.2). In the case of polarization preserving fibres and the Gaussian approximation (see Equation 4.6), the effective area is given by

$$\frac{1}{A_{\text{eff}}} = \frac{2}{\pi} \left(\hat{x}_p^2 + \hat{x}^2 \right)^{-\frac{1}{2}} \left(\hat{y}_p^2 + \hat{y}^2 \right)^{-\frac{1}{2}} \, . \tag{4.8}$$

In this thesis the Gaussian approximation will be used to calculate the effective area. Stolen [84, p130] warns that, 'a Gaussian fit to the mode intensity in a step index fibre results in an effective area which is 10%-15% too large. This is because there is more energy in the tail of a Gaussian than in the corresponding step-index guide mode.'

4.9 Refractive index and dispersion

4.9.1 Refractive index of fused silica

Following Agrawal [5], the refractive index of fused silica $n(\omega)$ for light of angular frequency ω is well approximated by the Sellmeier equation

$$n^2(\omega) = 1 + \sum_{j=1}^{3} \frac{B_j \, \omega_j^2}{\omega_j^2 - \omega^2} \tag{4.9}$$

where the values of ω_j and B_j are listed in Table 4.1.

j	ω_j (in rad/s)	B_j
1	2.7556×10^{16}	0.6961663
2	1.6216×10^{16}	0.4079426
3	1.9047×10^{14}	0.8974794

Table 4.1: Sellmeier data for fused silica.

4.9.2   Effective refractive index for optical fibres

In an optical fibre what is of interest is an effective refractive index, which is the velocity of light in vacuum divided by the phase velocity of light propagating in the fibre. Since part of the light is in the core, and part in the cladding, it might be expected that the effective refractive index lies somewhere between the refractive indices of the core and cladding materials. This is found to be the case. The effective refractive index is therefore within 1% of the refractive index of fused silica.

4.9.3   Dispersion

Over the wavelength range 575nm to 775nm (the range over which measurements were made in this thesis) the refractive index of fused silica (see Section 4.9.1) varies by less than 0.4%.

4.10   Presence of dopants

Of the dopant chemicals used in fibres to form the refractive index profile, germania (GeO_2) is one of the most common. It is added to the core to increase the refractive index. Galeener et al. [34] have shown that the Raman scattering cross-section of pure GeO_2 is about 9.2 times that of pure SiO_2. Walrafen and Stone [99] have shown that SiO_2 doped with quite high concentrations (13% by weight) of GeO_2 does not have a Raman scattering spectrum which is a weighted sum of the spectra for pure SiO_2 and GeO_2. Stolen [86] comments that at the concentrations used in low loss fibres, the dopants are unlikely to have a significant effect on the Raman spectrum.

Chapter 5

Equations for the Raman effect

A full theoretical treatment of the Raman effect will be presented later in this thesis (Appendix A). This treatment will begin at the microscopic level, dealing with the interaction between the electromagnetic field and the charged particles which constitute atomic matter. From this treatment, equations will emerge which have significance at a macroscopic level, for example, equations which quantify the rate at which Raman scattering transfers power from one optical beam to another. The equations can be written in such a way that the microscopic material parameters (for example, electronic wave functions) are absorbed into a single parameter which characterizes the material. Such parameters can be quantified in light scattering experiments.

The purpose of this chapter is to present these macroscopic equations for the Raman effect. While this order of presentation may seem back to front, it is justified on two counts. Firstly, following on from the qualitative discussion of Chapter 3, the equations give an introduction to the quantitative features of the Raman effect. Secondly, it is hoped that the chapter will serve as a useful reference for applied physicists and engineers working in the field of fibre optics.

Sections 5.1 and 5.2 give the equations for spontaneous and stimulated scattering (respectively) in the bulk glass geometry. Note that multimode fibres are a good approximation to bulk glass and that the bulk glass equations have been used to describe multimode fibre experiments. Section 5.3 gives a unified treatment of spontaneous and stimulated scattering in the single mode fibre geometry. In these three sections the spontaneous scattering probabilities and stimulated gains for the two different geometries are defined. Section 5.5 deals with pulse propagation in fibres. A discussion of experimental complications, such as fibre loss, is deferred until Chapter 6.

Although the microscopic treatment of Appendix A is a full quantum treatment (both light and matter are described in quantum mechanical terms),

it is not free of simplifying assumptions. These assumptions may limit the validity of the macroscopic equations. If this chapter is to make a useful reference then these assumptions should be pointed out. This is done in Section 5.6. In addition, the experimental testing of the macroscopic equations is not yet comprehensive; this should become clear on reading Chapters 2 and 11.

5.1 Spontaneous scattering in bulk glass

Figure 5.1 shows the geometry of an idealized scattering experiment in bulk glass. An optical beam with angular frequency ω_p propagates in the $+z$ direction. This beam is referred to as the pump beam. The linewidth of the beam is assumed to be narrow in comparison to features in the Raman spectrum (this means less than about 100GHz; true for most lasers). The beam is assumed to be an infinite plane wave, unchanging with time, linearly polarized with its electric field $\mathbf{e}_p$ parallel to the x axis. Spontaneous Raman scattering changes the direction of propagation and angular frequency of a small fraction of the pump photons. The scattered photons emerge in a wide range of directions (although the scattering may not be isotropic) and, in the case of glass, they have a range of angular frequencies which form a broad and continuous spectrum. The polarization of the photons may or may not be preserved by the scattering.

Suppose that the power of the pump beam incident on the imaginary volume element dV is P_p and the number of photons at angular frequencies other than the pump frequency is small so that stimulated effects can be neglected. Let P be the power of Raman scattered light produced by dV with a propagation direction that lies inside the solid angle $d\Phi$, a linear polarization with electric field direction $\mathbf{e}$, and an angular frequency in the interval $[\omega, \omega + d\omega]$. Then

$$P = \frac{\omega}{\omega_p} P_p \, \hat{R} \, d\Phi \, dz \, d\omega. \tag{5.1}$$

P scales linearly with $d\Phi$, dz and $d\omega$ and $\hat{R}$ is a constant of proportionality.
Defining Ω by

$$\Omega = \omega_p - \omega \tag{5.2}$$

and $h(\Omega, T)$ by

$$h(\Omega, T) = \begin{cases} \left(1 - e^{-\frac{\hbar\Omega}{kT}}\right)^{-1} & \text{for } \Omega > 0 \text{ (Stokes)} \\ \left(e^{-\frac{\hbar\Omega}{kT}} - 1\right)^{-1} & \text{for } \Omega < 0 \text{ (anti-Stokes)}, \end{cases} \tag{5.3}$$
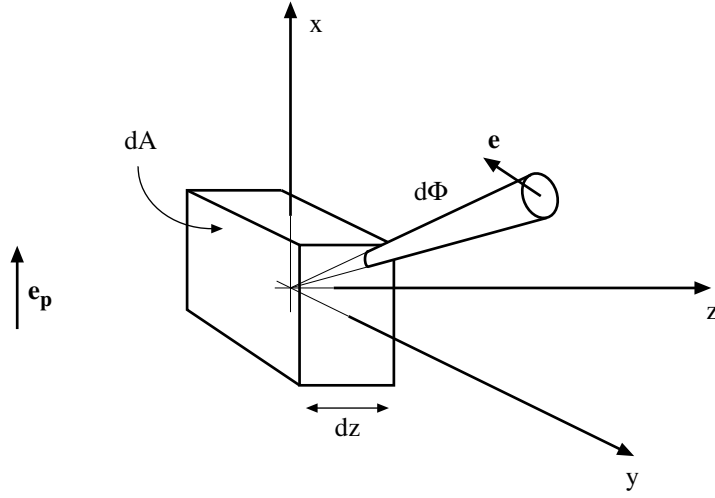
Figure 5.1: Geometry for scattering in bulk glass. The axes drawn are entirely embedded in glass (this is significant since the scattered light may experience Snell's law bending if it crosses an air/glass interface). The box is an imaginary boundary defining a small volume element $dV = dA\,dz$ of glass. The solid angle, $d\Phi$, is drawn here as a solid angle in three dimensional space. This is a little misleading; it is meant to represent a range of propagation directions for the scattered photons; only the orientation of $d\Phi$ has significance, the fact that it is centred at the origin is not relevant. Likewise only the orientation is significant for e_p and e, which specify the electric field directions of the pump beam and scattered photons respectively (both are assumed linearly polarized).

$\hat{R}$ is given by

$$\hat{R} = \frac{1}{32\pi^2\hbar\,\epsilon_0^2\,c^4}\,\frac{n\left(\omega\right)}{n\left(\omega_p\right)}\,\omega_p\,\omega^3\left[M_\parallel\left(|\Omega|\right)\cos^2\theta + M_\perp\left(|\Omega|\right)\sin^2\theta\right]h\left(\Omega, T\right).$$

(5.4)

Here ϵ_0 is the vacuum permittivity, c is the speed of light in vacuum, $n\left(\omega\right)$ is the refractive index for light of angular frequency ω (and similarly for $n\left(\omega_p\right)$), θ is the angle between $\mathbf{e}_p$ and $\mathbf{e}$, k is Boltzmann's constant and T is the absolute temperature of the glass. The functions of $|\Omega|$, $M_\parallel$ and $M_\perp$, depend on the nature of the material (for example, glass composition) as well as $|\Omega|$ (and they can be rapidly varying functions of $|\Omega|$) but they are approximately independent of other experimental parameters (temperature, ω_p, and so on). It is here that the microscopic parameters of the material (electronic wavefunctions, etc.) appear. To compute $M_\parallel$ and $M_\perp$ theoretically is difficult and a more practical approach is to calculate them from the results of light scattering experiments. A typical experiment involves measuring $\hat{R}$ as a function of Ω with ω_p held constant. This is what is usually meant by a Raman spectrum.

In this thesis, $M_\parallel$ and $M_\perp$ will be referred to as the material Raman functions.

Some features of the spontaneous scattering are immediately apparent from Equations 5.1 to 5.4. For a given $|\Omega|$

- the strength of the scattering scales approximately with ω_p^4 ($|\Omega|$ is much less than ω or ω_p).

- the anti-Stokes scattering is weaker than the Stokes scattering because of $h\left(\Omega, T\right)$.

- the strength of the scattering increases with temperature for both Stokes and anti-Stokes scattering.

- at high temperature, the strength of the anti-Stokes scattering approaches the strength of the Stokes scattering.

- at low temperature, the strength of the anti-Stokes scattering goes to zero, but the strength of the Stokes scattering limits to a constant value.

For a given $|\Omega|$ the ratio of the anti-Stokes power to Stokes power is given by

$$\frac{P\left(\text{anti-Stokes}\right)}{P\left(\text{Stokes}\right)} = \frac{n\left(\omega_p + |\Omega|\right)}{n\left(\omega_p - |\Omega|\right)}\,\frac{\left(\omega_p + |\Omega|\right)^4}{\left(\omega_p - |\Omega|\right)^4}\,e^{-\frac{\hbar|\Omega|}{kT}}.$$

(5.5)

The special cases of $\theta = 0$ and $\theta = \frac{\pi}{2}$ are referred to as parallel and perpendicular scattering respectively. Because of the transverse nature of electromagnetic radiation, the parallel scattered light is constrained to propagate in the yz plane. Hence, the most common experimental geometry is to observe the light scattered in the $+y$ direction. At the scale of a few atoms (e.g. 10nm), the structure of glass is not isotropic. At larger scales (e.g. 100nm) the structure consists of many of the smaller scale structures randomly oriented in space. In such a material [51]

$$0 \le M_\perp \le \frac{3}{4} M_\parallel. \tag{5.6}$$

Hence the parallel scattering is always stronger than the perpendicular scattering. Note that in some cases it is possible to deduce stronger relationships between $M_\perp$ and $M_\parallel$. For example, in the case of molecules whose equilibrium geometry has tetrahedral symmetry, any nuclear vibration which preserves this symmetry will have $M_\perp \equiv 0$ (see Section A.7).

Some authors refer to $\hat{R}$ as the differential cross-section for Raman scattering. This may seem rather peculiar as $\hat{R}$ does not appear to have the dimensions of area. But actually the terminology is correct. This becomes clear if Equation 5.1 is rewritten as

$$\frac{\left(\frac{P}{\hbar\omega}\right)}{\left(\frac{P_p}{\hbar\omega_p}\right)} = \hat{R} \frac{1}{dA} \, d\Phi \, dV \, d\omega. \tag{5.7}$$

The quantity on the left is the probability that a pump photon scatters and $\hat{R}$ now appears as the differential cross-section per unit volume of glass per unit angular frequency with dimensions $m^2 \, \text{sr}^{-1} \, \text{m}^{-3} \, (\text{rad/s})^{-1}$. In this thesis $\hat{R}$ will be referred to rather loosely as the bulk glass cross-section.

Note that the definition of cross-section in terms of the probability of a photon scattering is motivated by a particle picture of light. Some authors prefer to adopt the wave picture and work instead with the fraction of power scattered. This means that their equation analogous to Equation 5.1 is missing the factor of $\frac{\omega}{\omega_p}$.

5.2 Stimulated scattering in bulk glass

Again it is useful to refer to the glass bound coordinate frame in Figure 5.1. As in Section 5.1 there is an infinite plane wave, linearly polarized pump beam, with angular frequency ω_p (the same comments apply about its linewidth). In contrast to Section 5.1, the direction of propagation of the pump

beam is now taken to be arbitrary. Likewise the direction of linear polarization, $\mathbf{e}_p$, is also taken to be arbitrary (the transversality condition must still be satisfied). Let the intensity of the pump beam be denoted by I_p (the intensity of an optical beam is defined as the optical power per unit area incident on a plane normally oriented to the propagation direction of the beam). It is assumed that the pump beam is unchanging with time.

In addition to the pump beam there is now also a weaker beam which will be referred to as the signal beam. Like the pump, the signal is a linearly polarized, infinite plane wave, unchanging with time. The signal is assumed to be propagating in the $+z$ direction. No assumption is made about the linewidth of the signal beam.

The signal can be resolved into two components, a parallel component which has its electric field vector parallel to $\mathbf{e}_p$, and a perpendicular component which has its electric field vector perpendicular to $\mathbf{e}_p$. From the point of view of stimulated Raman scattering, these are best dealt with separately.

Let $\Lambda_\parallel(z)$ denote the intensity at position z of that part of the parallel component of the signal which has angular frequency inside the interval $[\omega, \omega + d\omega]$. If $\Lambda_\parallel$ is sufficiently great that spontaneous scattering can be neglected, then $\Lambda_\parallel$ evolves with distance due to stimulated scattering according to

$$\frac{d}{dz}\Lambda_\parallel(z) = \hat{g}_\parallel \, I_p \, \Lambda_\parallel(z).$$ (5.8)

$\hat{g}_\parallel \, I_p$ is referred to as the (parallel) Raman gain and $\hat{g}_\parallel$ as the (parallel) Raman gain coefficient. $\hat{g}_\parallel$ is given by

$$\hat{g}_\parallel = \frac{\Omega}{|\Omega|} \, \frac{\pi}{4 \, \hbar^2 \, \epsilon_0^2 \, c^2} \, \frac{\omega}{n(\omega_p) \, n(\omega)} \, M_\parallel(|\Omega|).$$ (5.9)

The symbols which appear here, are the same as those in Equation 5.4, and are intended to have the same meaning. In particular, it is the same $M_\parallel$ which appears in both Equations 5.4 and 5.9.

The intensity of that part of the perpendicular component of the signal which has angular frequency inside the interval $[\omega, \omega + d\omega]$, $\Lambda_\perp$, obeys two exactly analogous equations (just replace the $\parallel$ subscript with a $\perp$ subscript throughout Equations 5.8 and 5.9).

Stimulated scattering is the transfer of photons from one beam to a second, due to the presence of photons already in the second beam. Stimulated scattering is actually able to transfer photons from signal to pump as well as from pump to signal. In the case of Stokes scattering (signal at lower frequency than pump), there is a net transfer of photons from pump to signal (the gain coefficient is positive and the signal is amplified). In the case of anti-Stokes scattering (signal at higher frequency than pump), there is a

net transfer of photons from signal to pump (the gain coefficient is negative and the signal is attenuated). Note that the scattered photons inherit the properties of the beam they are scattered to.

The attenuation of signal in the case of anti-Stokes scattering is sometimes called the inverse Raman effect. In many experiments both Stokes and anti-Stokes beams are observed to grow. These experiments are often referred to as stimulated scattering experiments, but the growth of the anti-Stokes beam is actually due to four wave mixing (see Sections 3.5.2 and 3.5.3). The growth of the anti-Stokes beam is also the basis of a powerful spectroscopic technique called coherent anti-stokes Raman scattering (CARS).

In contrast to the spontaneous cross-section, the gain coefficient scales approximately linearly with ω_p and is independent of temperature.

5.3 Scattering in single mode optical fibres

In Sections 5.1 and 5.2, spontaneous and stimulated scattering were dealt with separately. In the case of bulk glass, the three dimensional nature of the problem makes a unified treatment rather difficult. When light propagates in the guided mode of a single mode fibre, Raman scattered photons can either be trapped in the guide or lost through the cladding. If only those photons which remain trapped in the guide are of interest, then the fibre problem appears quasi one dimensional and lends itself to a treatment in which the spontaneous and stimulated scattering are considered together. Such a unified treatment is given in this section. It should be pointed out that, in the case of spontaneous scattering, the scattered photons which remain in the guide are actually the minority; most scattered photons are lost through the cladding.

Suppose that a fibre is positioned in a coordinate frame such that z gives distance down the fibre (see Figure 4.1a). Also suppose that a linearly polarized pump beam with optical power P_p and angular frequency ω_p propagates down the fibre. The pump beam is assumed to be unchanging with time and unchanging with z and the remarks made about linewidth in Section 5.1 are also pertinent here. In what follows it makes no difference if the beam is propagating in the $+z$ or $-z$ directions. As well as the pump beam there may be weaker beams propagating in the fibre. These are also assumed to be unchanging with time.

Let $\Gamma_{\parallel}(z)$ denote the optical power per unit angular frequency at angular frequency ω (distinct from ω_p) and position z, propagating in the $+z$ direction and linearly polarized with electric field vector parallel to the electric field vector of the pump. The Raman effect causes $\Gamma_{\parallel}(z)$ to evolve with distance

according to

$$\frac{d}{dz}\Gamma_\parallel(z) = \left[\frac{\omega}{\omega_p}R_\parallel + g_\parallel\Gamma_\parallel(z)\right]P_p. \tag{5.10}$$

The quantity $R_\parallel\,d\omega\,dz$ is the probability that a pump photon spontaneously scatters on propagation through a section of fibre of length dz, such that, after scattering, the polarization of the photon is unchanged, it is propagating in the $+z$ direction and its angular frequency lies in the interval $[\omega,\omega+d\omega]$. Strictly speaking, $R_\parallel$ is not a cross-section and it will be referred to as the spontaneous scattering coefficient.   The quantity $g_\parallel\,P_p$ is the stimulated Raman gain, and $g_\parallel$ the gain coefficient. $R_\parallel$ and $g_\parallel$ are given by

$$R_\parallel = \frac{1}{8\hbar\,\epsilon_0^2\,c^2}\frac{\omega_p\,\omega}{n(\omega_p)\,n(\omega)}\,h(\Omega,T)\int_{-\infty}^{\infty}dx\int_{-\infty}^{\infty}dy\,M_\parallel(|\Omega|)\,|f_p|^2\,|f|^2. \tag{5.11}$$

$$g_\parallel = \frac{\Omega}{|\Omega|}\frac{\pi}{4\hbar^2\,\epsilon_0^2\,c^2}\frac{\omega}{n(\omega_p)\,n(\omega)}\int_{-\infty}^{\infty}dx\int_{-\infty}^{\infty}dy\,M_\parallel(|\Omega|)\,|f_p|^2\,|f|^2. \tag{5.12}$$

Here $n(\omega_p)$ and $n(\omega)$ are the effective refractive indices (see Section 4.9.2) for light polarized parallel to the pump with angular frequency ω_p and ω respectively. The functions $f_p(x,y)$ and $f(x,y)$ specify the transverse mode profiles (see Section 4.2) for light polarized parallel to the pump with angular frequencies ω_p and ω respectively. The remaining symbols in Equations 5.11 and 5.12 are the same as those in Equation 5.4 and have the same meaning. In particular, $M_\parallel$ takes the value that would be appropriate for a sample of bulk glass with the same composition as the glass at position (x,y) in the fibre (recall from Section 4.1 that the glass composition varies with position).

To obtain propagation equations for light propagating in the $+z$ direction but polarized orthogonally to the pump, simply replace the $\parallel$ subscript with a $\perp$ subscript in Equations 5.10 through 5.12 (note that $n(\omega)$ and $f(x,y)$ may also need to be replaced with appropriate values for light of angular frequency ω but orthogonal polarization to the pump).

From the propagation equations for light propagating in the $+z$ direction, analogous equations can be obtained for light propagating in the $-z$ direction by substituting $-z$ for z.

Comparison of the equations in this section with those in Sections 5.1 and 5.2, indicates that Raman scattering in fibres is essentially the same as Raman scattering in bulk glass. It may seem from Equations 5.10 and 5.11 that the spontaneous scattering in fibres scales approximately with ω_p^2 (as opposed to ω_p^4 in bulk glass), but this is not really true as the functions $f_p(x,y)$ and $f(x,y)$ are also angular frequency dependent (see Section 4.2). In the Gaussian approximation (see Section 4.4) the ω_p^4 behaviour is recovered (see Equation 4.4).

Equation 5.10 has an analytic solution. The value of $\Gamma_\parallel$ at any position z is related to the value of $\Gamma_\parallel$ at a fixed position z_0 (which may be chosen arbitrarily) according to

$$\Gamma_\parallel(z) = \left[\Gamma_\parallel(z_0) + \frac{\omega R_\parallel}{\omega_p g_\parallel}\right] e^{(z-z_0)g_\parallel P_p} - \frac{\omega R_\parallel}{\omega_p g_\parallel}. \tag{5.13}$$

In the special case where $z = 0$ corresponds to one end of the fibre (see Figure 4.1a) and the pump beam is the only beam incident on the fibre, $\Gamma_\parallel$ is given by

$$\Gamma_\parallel(z) = \frac{\omega R_\parallel}{\omega_p g_\parallel}\left[e^{g_\parallel P_p z} - 1\right]. \tag{5.14}$$

Note that $\Gamma_\parallel$ is only a function of the product $P_p z$.

5.4 Fibres which do not preserve polarization

If the light at the Raman scattered wavelength contains a sufficient number of photons (perhaps because a signal beam has been launched into the fibre as well as the pump), then spontaneous scattering is negligible, and Equation 5.10 simplifies to

$$\frac{d}{dz}\Gamma_\parallel(z) = g_\parallel \Gamma_\parallel(z) P_p. \tag{5.15}$$

Stolen [85] has investigated, both theoretically and experimentally, how this equation should be modified to describe experiments in ordinary single mode fibres where the polarization of light is not preserved. If linearly polarized signal and pump beams are launched into such a fibre, their linear polarization state is found to have decayed to random polarization after propagation through some distance. At this point, although the linear polarization is lost, the polarization of the two beams remains correlated. However, upon further propagation through the fibre, even this correlation in polarization is lost. If the fibre is long in comparison to this distance, then Stolen argues that the total (sum of x polarized and y polarized; see Figure 4.1) Raman light, Γ, is related to the total pump power, P_p, by an equation the same as Equation 5.15, except that $g_\parallel$ is replaced by $(g_\parallel + g_\perp)/2$. The same holds with multimode fibres; Λ and $(\hat{g}_\parallel + \hat{g}_\perp)/2$ replacing $\Lambda_\parallel$ and $\hat{g}_\parallel$ (respectively) in Equation 5.8.

Some authors have assumed from Stolen's work that Equation 5.10 can be adapted to suit fibres which do not preserve polarization by replacing $\Gamma_\parallel$ with Γ, $R_\parallel$ with $\left(R_\parallel + R_\perp\right)/2$ and $g_\parallel$ with $(g_\parallel + g_\perp)/2$. In other words, they

have assumed that both spontaneous and stimulated scattering coefficients will halve. In the context of fibre Raman amplifiers this means that the gain of the amplifier will be reduced, but there will also be a corresponding reduction in amplifier noise, with no overall loss in performance.

From a theoretical point of view, this assumption would seem to be incorrect, since the growth rate of the spontaneously scattered light is independent of the polarization of the pump. Only two experiments of relevence to this issue would seem to have been performed to date. Mochizuki et al. [61] measured the spontaneous scattering from a 53km length of normal (not polarization preserving fibre). Aoki [7] made similar measurements in a 3.5km length of fibre. Aoki's measurements extend into the range where stimulated scattering is important. Both authors also measured the gain coefficient of their fibres using a pump/signal arrangement. They then used their measured gain to predict the outcome of their spontaneous scattering experiments, assuming $R_\parallel \rightarrow \left(R_\parallel + R_\perp \right)/2$. Mochizuki et al. get good agreement, but Aoki's results clearly show a factor of two error.

Formulating correct equations for Raman scattering with beams of various polarizations is of some importance if Raman amplifiers are to be used in telecommunications applications. In current telecommunications networks the signals which require amplification are randomly polarized. In this case, a Raman amplifier may well produce less noise for the same gain if, instead of using a single, polarized laser as the pump, the power is shared between two, independent, orthogonally polarized lasers. This is an obvious candidate for further research, both theoretically and experimentally.

5.5   Pulses in fibres

The theory used to obtain the results in this chapter only requires that the light beams be slowly varying with time. To be precise, if the pump is pulsed then the frequency bandwidth of the pulses must be narrow in comparison to the frequency bandwidth of features in the Raman spectrum (see Section A.5.2). The Raman spectrum is approximately constant over frequency bandwidths of about 1THz (see Figures 9.3 and 9.6). Assuming the pulses are near transform limited, the theory will therefore be successful provided the pulses are longer than about 1ps.

In the absence of any Raman interaction, and neglecting dispersion (acceptable for picosecond pulses and fibres only a few metres long), a signal pulse at angular frequency ω propagates in the $+z$ direction according to

$$\frac{\partial}{\partial z}\Gamma_\parallel \left(z,t \right) = -\frac{1}{v}\,\frac{\partial}{\partial t}\Gamma_\parallel \left(z,t \right) \tag{5.16}$$

where v is the group velocity at angular frequency ω. The presence of the Raman interaction requires an additional evolution with position according to Equation 5.10, so the quasi cw propagation equation for pulses is

$$\frac{\partial}{\partial z}\Gamma_\parallel(z,t) = \left[\frac{\omega}{\omega_p}R_\parallel + g_\parallel\Gamma_\parallel(z,t)\right]P_p(z,t) - \frac{1}{v}\frac{\partial}{\partial t}\Gamma_\parallel(z,t) \qquad (5.17)$$

where $R_\parallel$ and $g_\parallel$ are as given by Equations 5.11 and 5.12.

5.6 Assumptions

These are the assumptions which have been made in Appendix A in order to obtain the equations in this chapter. Note that it might be possible to obtain the same equations without recourse to all these assumptions.

1. The matter is modelled as discrete molecules, randomly oriented in space.

2. The molecules are assumed to be small in comparison to the wavelength of light (which means that the phonons are localized in comparison to the optical wavelength [77]).

3. The molecules are assumed to all be slightly different so that there is a near continuum of phonon frequencies (inhomogeneous broadening).

4. Optical frequency electromagnetic radiation is assumed to interact with the molecules only through the electric dipole moment associated with motion of the electrons (this is why it is appropriate to work with a basis of linear polarizations for the light). Any magnetic effects, for example, are completely ignored.

5. There are assumptions of linear behaviour.

   - The nuclei are assumed to be held in position by harmonic potentials. This means that there exists a basis of harmonic normal modes for the collective motion of the nuclei (the phonons are the quanta of these modes).
   - The dipole moment associated with electronic motion (polarizability) is assumed to vary linearly with the amplitude of any normal mode.

These assumptions mean that the equations are only appropriate for fundamental Raman transitions.   Overtones and combination bands can have a different temperature dependence (see Section A.11). Note that the main peak in the Raman spectrum at about 450cm^{-1} (see Figure 9.3) is a fundamental transition but that some of the other peaks, such as the peak at about 1600cm^{-1}, are overtones or combination bands (see Section 9.4).

6. The phonon frequencies (typically less than 50THz) are assumed to be small in comparison to the optical frequencies (typically about 450THz) which, in turn, are assumed to be small in comparison to the frequency separation between ground and excited electronic states (the band gap in fused silica is about 10eV [11, Fig. 7.1], corresponding to a frequency of 2400THz).   Note that, in this context, x is small in comparison to y if $x + y \simeq y$.

7. The phonon modes are assumed to be in thermal equilibrium (each phonon mode has a well defined number of phonons, but the number varies from one mode to another in a statistical fashion). This assumption is of great importance as it means that the Raman light generated by different molecules adds incoherently (which implies there are no phase matching requirements).   The occurrence of Raman scattering does modify the state of the phonon modes but this is assumed negligible.   The validity of this last assumption is difficult to quantify.

8. It is assumed that the pump can be treated classically, which requires that it contain a large number of photons.   In practical terms, and assuming red wavelengths, this means it must have an optical power per unit angular frequency well in excess of $5 \times 10^{-20}\text{W}/\left(\text{rad/s}\right)$ (see Section A.6), which corresponds to a power per unit wavelength of 220nW/nm.   The pump is also assumed to be unchanged by the scattering, which means that the pump power must be orders of magnitude greater than the Raman power.

9. The electromagnetic field modes associated with signal frequencies are assumed to be in number states.   Comments made by Loudon [53, p177] suggest that this is not a necessary assumption.   However, it would be nice to pursue this further.

10. All optical beams are assumed to be slowly varying, which means that, in the case of pulses, the pulses must be longer than about 1ps.

11. The only physical processes included are Raman scattering and the linear refractive index (although dispersion is neglected in the propagation of the signal in Equation 5.17). Interaction between the phonon modes is ignored (such interaction presumably maintains the phonon modes in thermal equilibrium; see 7). Four wave mixing and cross-phase modulation are ignored (and noticeably absent from Equations 5.10 and 5.17). The omission of four wave mixing may be a serious error in the limit of high pump power for anti-Stokes scattering (see Chapters 10 and 11). Brillouin scattering is ignored, but this is probably valid unless the linewidth of the pump laser is less than a few hundred MHz [82].

Chapter 6

Relating theory to experiment

Experimental testing of the Raman scattering equations for fibres (see Sections 5.3 and 5.5) would seem to be a simple matter of launching a pump beam into an optical fibre (and possibly also a signal beam, although this will not be the case in this thesis), measuring the pump power, P_p, and the power per unit angular frequency, Γ, produced at frequencies distinct from the pump frequency. However, as with all experiments, complications arise; powers cannot actually be measured inside the fibre, there are losses, and so on. This chapter deals with how the equations in Sections 5.3 and 5.5 must be modified in order to describe the experiments reported in this thesis.

6.1   Spontaneous scattering experiments

If Γ is sufficiently small, which is true in the limit of low pump power, then stimulated scattering can be neglected. In the case of a cw experiment, Equations 5.10 and 5.14 reduce to

$$\frac{d}{dz}\Gamma_{\parallel}\left(z\right) = \frac{\omega}{\omega_p}\,R_{\parallel}\,P_p \tag{6.1}$$

and

$$\Gamma_{\parallel}\left(z\right) = \frac{\omega}{\omega_p}\,R_{\parallel}\,P_p\,z \tag{6.2}$$

respectively. All the cw experiments performed in this thesis are in the limit of low pump power and Equations 6.1 and 6.2 are appropriate.

In the case of pulses and low pump power, Equation 5.17 reduces to

$$\frac{\partial}{\partial z}\Gamma_{\parallel}\left(z,t\right) = \frac{\omega}{\omega_p}\,R_{\parallel}\,P_p\left(z,t\right) - \frac{1}{v}\,\frac{\partial}{\partial t}\Gamma_{\parallel}\left(z,t\right). \tag{6.3}$$

In the pulsed experiments, all quantities measured are time averages. Assuming the pump laser produces pulses periodically, then long time averages are the same as averages over one period. Averaging both sides of Equation 6.3 over one period gives

$$\frac{d}{dz} \left\langle \Gamma_\parallel (z,t) \right\rangle_t = \frac{\omega}{\omega_p} R_\parallel \left\langle P_p (z,t) \right\rangle_t \tag{6.4}$$

where $\langle x \rangle_t$ denotes time average of quantity x and use has been made of the result that, if the pump produces pulses periodically, then $\Gamma_\parallel$ will be periodic, and the time average of $\frac{\partial}{\partial t} \Gamma_\parallel$ over one period will therefore be zero. Comparison of Equation 6.4 with Equation 6.1 reveals that spontaneous scattering experiments with cw and pulsed pumps are indistinguishable, provided only time averages are measured (and provided the pulses are longer than a few picoseconds; see Section 5.5).

6.2 Stimulated scattering experiments

In some of the experiments with pulses, the pump power was sufficiently great that stimulated scattering could not be neglected. In order to compare theory with experiment, a solution to Equation 5.17 is therefore required. It is convenient to assume that the input end of the fibre is at $z = 0$ (see Figure 4.1a). Following Agrawal [5], it helps to change coordinate from laboratory time t to retarded time T, where T is given by

$$T = t - \frac{z}{v}. \tag{6.5}$$

In the new coordinate frame, Equation 5.17 becomes

$$\frac{\partial}{\partial z} \Gamma_\parallel (z,T) = \left[\frac{\omega}{\omega_p} R_\parallel + g_\parallel \Gamma_\parallel (z,T) \right] P_p (z,T). \tag{6.6}$$

6.2.1 Propagation of pump pulses

In general, the pump pulses will evolve on propagation. Even if the pump is undepleted by the scattering and there is no loss, dispersion can broaden the pulses in time. Temporal broadening is most severe at high pump powers because self-phase modulation causes the spectrum of the pulses to broaden. Note that, from the point of view of Raman scattering, self-phase modulation is otherwise insignificant, provided the spectral width of the pulses remains narrow in comparison to features in the Raman spectrum (which in practice means less than about 10^{12}rad/s).

The stimulated scattering experiments reported in this thesis involved 60ps duration (intensity FWHM), near transform limited pulses with a $sech^2$ intensity profile and peak power no greater than about 450W. The temporal broadening experienced by these pulses on propagation through 3m of fibre (the length used in the experiments) can be estimated by following Agrawal [5, Second Edition]. The $sech^2$ intensity profile can be approximated by a Gaussian. For a transform limited Gaussian pulse with temporal power FWHM, T_F, the spectral power FWHM, ω_F, is given by

$$\omega_F = \frac{4\ln 2}{T_F} = 4.6 \times 10^{10} \text{rad/s.} \tag{6.7}$$

Agrawal defines the dispersion parameter β_2 by [5, Eq. (1.2.12)]

$$\beta_2 = \frac{d}{d\omega}\left(\frac{1}{v_g}\right). \tag{6.8}$$

Here v_g is the group velocity. For red wavelengths the value of β_2 is about $50 \times 10^{-27}\, (\text{m/s})^{-1}\,(\text{rad/s})^{-1}$ [5, Fig. 1.5].

Assuming no SPM, the high frequency and low frequency components of the pulse will take different times to travel along a length z of fibre. The difference between the times is given by

$$\triangle t = z\,\frac{d}{d\omega}\left(\frac{1}{v_g}\right)\omega_F = z\,\beta_2\,\omega_F. \tag{6.9}$$

Using values for the pulse gives $\triangle t = 6.9$fs, which is completely negligible in comparison to the pulse duration.

In the absence of dispersion, SPM causes the pulse spectrum to broaden to a new spectral power FWHM, ω'_F, approximately given by [5, Eqs. (4.1.16) and (4.1.6)]

$$\omega'_F \simeq \omega_F \left(1 + \frac{4}{3\sqrt{3}}\,(\gamma P z)^2\right)^{\frac{1}{2}} \tag{6.10}$$

where P is the peak power. For red wavelengths, $\gamma \simeq 0.025/\,(\text{Wm})$ [63] so $\omega'_F \simeq 1.3 \times 10^{12}$rad/s (which is only just consistent with the assumption that the linewidth is narrow in comparison to features in the Raman spectrum). This is the spectral width at the end of the fibre. Assuming a pulse with this spectral width was launched into the fibre, and also assuming no SPM, Equation 6.9 can be used to predict the expected separation in time between high and low frequency components at the end of the fibre. The result is 200fs which is still negligible in comparison to the pulse duration.

In the experiments, the duration of the pump pulses was also measured before and after propagation through the fibre. The results were the same

within experimental error, providing further support that the pulses do not change shape on propagation through 3m of fibre.

6.2.2   Walk off between pump and Raman

If the pump pulses do not change shape on propagation, $P_p(z,t)$ can be written in the form

$$P_p(z,t) = P_p\left(0, t - \frac{z}{v_p}\right) = P_p\left(0, T + \left(\frac{1}{v} - \frac{1}{v_p}\right)z\right) = P_p(0, T - \beta_2\,\Omega\,z)$$

(6.11)

where v_p is the group velocity for the pump (and v is the group velocity for the Raman light) and Ω is given by Equation 5.2.   At the peak of the Raman spectrum (see Figure 9.5), Ω is about 80×10^{12}rad/s.   It then follows that $\beta_2\,\Omega\,z \leq$ 12ps.   Since the pump pulse has duration 60ps, it does not change appreciably over time intervals shorter than 12ps, so the approximation $P_p(0, T - \beta_2\,\Omega\,z) \simeq P_p(0, T)$ may be made.   Physically this corresponds to the pump pulse and the Raman light it generates remaining together during propagation down the fibre.

6.2.3   Time averaging

Neglecting the walk off reduces Equation 6.6 to

$$\frac{\partial}{\partial z}\Gamma_\parallel(z, T) = \left[\frac{\omega}{\omega_p}R_\parallel + g_\parallel\,\Gamma_\parallel(z, T)\right]P_p(0, T).$$

(6.12)

T now appears as a parameter, and the equation can be solved analytically. Assuming $\Gamma_\parallel(0, T) \equiv 0$ (the pump beam is the only beam incident on the fibre), the solution is

$$\Gamma_\parallel(z, T) = \frac{\omega\,R_\parallel}{\omega_p\,g_\parallel}\left[e^{g_\parallel P_p(0,T)\,z} - 1\right].$$

(6.13)

(Compare this with Equation 5.14.)

In the experiments what is measured are long time averages.   Assuming the laser produces pulses periodically (with a time between pulses of T_R), long time averages are the same as averages over one period.   The long time average of the pump power, $\langle P_p\rangle_t$, is given by

$$\langle P_p\rangle_t = \frac{1}{T_R}\int\limits_{T_R} dT\,P_p(0, T).$$

(6.14)

Similarly the long time average of $\Gamma_\parallel (z, T)$ is given by

$$\langle \Gamma_\parallel (z) \rangle_t = \frac{1}{T_R} \int\limits_{T_R} dT \, \frac{\omega \, R_\parallel}{\omega_p \, g_\parallel} \left[e^{g_\parallel P_p(0,T) \, z} - 1 \right] . \qquad (6.15)$$

6.2.4 $sech^2$ pulse shape

If the pump pulses have a $sech^2$ pulse shape then the integral in Equation 6.14 can be evaluated analytically. This can be used to obtain the result

$$P_p (0, T) = \frac{1.7627}{2} \frac{T_R}{T_F} \langle P_p \rangle_t \, sech^2 \left(1.7627 \frac{T}{T_F} \right) . \qquad (6.16)$$

With this pulse profile, the integral in Equation 6.15 does not have an analytic solution and it must be evaluated numerically.

6.3 Collection efficiency, filter function, bandwidth and centre wavelength for monochromator and PM tube

Measurement of the power per unit angular frequency, Γ, is accomplished in the experiments by passing the broadband light emerging from the output end of the fibre through a narrow band optical filter (monochromator) and then measuring the optical power after the filter with a detector (in this case, with a photon counting photomultiplier (PM) tube). Note that Γ is a function (and possibly a rapidly varying function) of angular frequency. In this section this dependence will be made explicit by writing $\Gamma (\omega')$.

The fraction of photons leaving the end of the fibre, with angular frequency ω', which result in a count at the PM tube, can be written as $\eta F (\omega')$ where η is a constant and $F (\omega')$ is normalized so that its maximum value is unity. $F (\omega')$ is proportional to (but not equal to) the transmission of the monochromator to light of angular frequency ω', and will be referred to as the filter function of the monochromator. η is the fraction of photons which result in a count in the special case of a monochromatic beam whose angular frequency is chosen to give optimum transmission through the monochromator. η will be referred to as the collection efficiency of the monochromator/PM tube. Note that η takes into account losses in both the optics and the detector.

With these definitions, the count rate at the photomultiplier tube, C, in units of counts per second (cps), is given by

$$C = \int d\omega' \, \eta F(\omega') \, \frac{\Gamma(\omega')}{\hbar\omega'}. \tag{6.17}$$

If $F(\omega')$ is non-zero only over a small interval centred at ω (corresponding to a wavelength of λ_c which will be referred to as the centre wavelength of the monochromator), and if $\Gamma(\omega')$ is approximately constant over this interval, then Equation 6.17 simplifies to

$$\Gamma(\omega) = \frac{\hbar\omega \, C}{\eta \int d\omega' \, F(\omega')} \tag{6.18}$$

With optical filters, it is customary to work with wavelength rather than angular frequency, so Equation 6.18 is then most usefully written

$$\Gamma(\omega) = \frac{2\pi c \hbar \, C}{\omega \eta \int d\lambda \, F(\lambda)} \tag{6.19}$$

In obtaining Equation 6.19, the property of $F(\omega')$ that it is non-zero only over a small interval centred at ω, has been used. The quantity $\int d\lambda \, F(\lambda)$ will be referred to as the bandwidth ($F(\lambda)$ is dimensionless because it is normalized).

From Equation 6.19 it is clear that, if the collection efficiency and bandwidth are known, then Γ can be determined by measuring the count rate. In the experiments the filter could be tuned to different centre wavelengths by realigning the monochromator. This allowed measurement of Γ at different angular frequencies (spectra). Note that tuning the filter changed both the collection efficiency and the bandwidth, as well as the centre wavelength.

6.4   Fibre homogeneity and material Raman functions

In Equations 5.11 and 5.12, the material Raman function $M_\parallel(|\Omega|)$ is assumed to be a function of position. Strictly speaking this is necessary, since the glass composition of a fibre is not uniform (see Section 4.1). However, if the material Raman functions for the core and cladding glasses are approximately equal (which is a expected to be true for most fibres because the concentration of dopant chemicals is low), then the position dependence of $M_\parallel(|\Omega|)$ can be

neglected. The integral which appears in Equations 5.11 and 5.12 can then be approximated using

$$\int_{-\infty}^{\infty} dx \int_{-\infty}^{\infty} dy \, M_{\parallel}\left(|\Omega|\right) |f_p|^2 \, |f|^2 \simeq$$

$$M_{\parallel}\left(|\Omega|\right) \int_{-\infty}^{\infty} dx \int_{-\infty}^{\infty} dy \, |f_p|^2 \, |f|^2 = \frac{M_{\parallel}\left(|\Omega|\right)}{A_{\mathrm{eff}}}. \tag{6.20}$$

6.5 Fibre loss in spontaneous scattering experiments

In the regime of low intensity, the dominant loss mechanisms are elastic scattering and single photon absorption (loss due to spontaneous Raman scattering is negligible in comparison). In the presence of loss, the pump power evolves with distance according to

$$\frac{d}{dz} P_p\left(z\right) = -\alpha_p P_p\left(z\right) \tag{6.21}$$

where α_p is the fibre loss at the pump angular frequency. Similarly, the spontaneous Raman light evolves according to

$$\frac{d}{dz} \Gamma_{\parallel}\left(z\right) = \frac{\omega}{\omega_p} \, R_{\parallel} \, P_p\left(z\right) - \alpha \, \Gamma_{\parallel}\left(z\right) \tag{6.22}$$

where α is the fibre loss at angular frequency ω (compare this with Equation 6.1).

Equations 6.21 and 6.22 form a system of coupled differential equations which can be solved analytically. Assuming the start of the fibre is at $z = 0$ (see Figure 4.1a) and the pump beam is the only beam incident on the fibre, the solution for $\Gamma_{\parallel}\left(z\right)$ is

$$\Gamma_{\parallel}\left(z\right) = \frac{\omega}{\omega_p} \frac{R_{\parallel}}{\alpha - \alpha_p} \left(1 - e^{(\alpha_p - \alpha)z}\right) P_p\left(z\right). \tag{6.23}$$

In the limit $\alpha \to \alpha_p$, Equation 6.23 reduces to

$$\Gamma_{\parallel}\left(z\right) = \frac{\omega}{\omega_p} \, R_{\parallel} \, P_p\left(z\right) \, z \tag{6.24}$$

and the outcome of a spontaneous Raman scattering experiment is found to be independent of loss, provided the loss is independent of angular frequency and provided P_p and $\Gamma_{\parallel}$ are measured at the same position (in a typical

experiment this is true, since they are both measured at the end of the fibre).

If $\alpha \neq \alpha_p$ then Equation 6.23 reduces to Equation 6.24 only in the limit of short fibre length. Since the disparity between the two equations increases with distance, it is interesting to substitute some numbers for the longest fibre used in the experiments (40m of FS-HB-3611; see Section 7.4). If the loss mechanism is Rayleigh scattering, then α will vary with ω according to the relation

$$\alpha\left(\omega\right) = \left(\frac{\omega}{\omega_p}\right)^4 \alpha_p \qquad (6.25)$$

The loss of the fibre quoted by the manufacturer was 34dB/km at a wavelength of 630nm which gives $\alpha_p = 7.034 \times 10^{-3}/$m (647.1nm). At the peak of the Raman spectrum ($\Omega = 83 \times 10^{12}$rad/s; see Figure 9.5) the value for $\Gamma_\parallel$ predicted by Equation 6.24 differs from the prediction of Equation 6.23 by 1.5% (which is negligible). At the largest frequency shifts measured in this thesis, 647.1nm to 736.8nm which corresponds to $\Omega = 355 \times 10^{12}$rad/s, and 647.1nm to 576.5nm which corresponds to $\Omega = -357 \times 10^{12}$rad/s, this difference increases to 5.7% and 8.3% respectively (which is just becoming significant). This would seem to justify the use of Equation 6.24 in place of Equation 6.23, an approach which will be adopted in this thesis.

Some caution is required here. Synthetic silicas can have losses as low as about 10dB/km at 630nm [23, Fig. 11.8] and stress induced birefringent fibres are available with losses this low (the HB600 from Fibrecore has a loss of 12dB/km at 630nm), so the loss of the FS-HB-3611 fibre is very high. Rough experimental measurement of the loss (by comparing the transmission at 647nm of two pieces of the fibre, one of length 40m and the other of length 6.5m) tended to support the high loss quoted by the manufacturer. It might be that the fibre simply has a high concentration of imperfections that can act as Rayleigh scatterers, but there is also the possibility that the loss is due to absorption. Drawing induced defects are known to have an absorption band at about 630nm [11, p172] [66, Section 5]. Likewise transition metal impurities, such as Cr, V and Co, are known to cause absorption at red wavelengths [11, p174] [26]. In the presence of absorption, the fibre loss may have a stronger frequency dependence than Equation 6.25 predicts. This would further increase the divergence between Equations 6.23 and 6.24. A worst case scenario for Stokes scattering [23, Fig. 11.8], might be to have a loss of 30dB/km at 647nm due to drawing induced defects, and a loss of only 5dB/km at 736nm (which is about the minimum loss at this wavelength achievable with fused silica). For a 40m piece of fibre and scattering from 647nm to 736nm, the difference between the values of $\Gamma_\parallel$ predicted by

Equations 6.24 and 6.23 is then about 12%.

In this thesis, Equation 6.24 will be used in place of Equation 6.23. This introduces an error which cannot be quantified without data on the wavelengths dependence of the fibre loss. It is unlikely that this error is significant for small angular frequency shifts. But the same may not be true for large frequency shifts.

6.6 Sources of background in spontaneous scattering experiments

Equation 6.2 give the power per unit angular frequency assuming Raman scattering is the only source of detected light. In a real experiment there are other sources (background sources) and a more realistic relation is

$$\Gamma_{\parallel}(z) = \left(\frac{\omega}{\omega_p} R_{\parallel} z + b_p\right) P_p + b_0. \tag{6.26}$$

Here b_0 accounts for sources of background which are independent of the pump (for example, room lights and dark counts), whilst b_p accounts for sources of background which are proportional to the pump (for example, scattered pump light which reaches the PM tube). A plot of $\Gamma_{\parallel}$ verses P_p will therefore be a straight line with gradient

$$\mathrm{grad}\left(\Gamma_{\parallel} \text{ vs } P_p\right) = \frac{\omega}{\omega_p} R_{\parallel} z + b_p \tag{6.27}$$

and a plot of $\mathrm{grad}\left(\Gamma_{\parallel} \text{ vs } P_p\right)$ verses z will also be a straight line with gradient

$$\mathrm{grad}\left(\mathrm{grad}\left(\Gamma_{\parallel} \text{ vs } P_p\right) \text{ vs } z\right) = \frac{\omega}{\omega_p} R_{\parallel} \tag{6.28}$$

which allows $R_{\parallel}$ to be recovered.

Chapter 7

Apparatus overview

As mentioned in the introduction to Chapter 6, experimental testing of the Raman scattering equations would seem a simple matter of launching a pump beam into an optical fibre, measuring its power and then measuring the Raman power produced in a frequency interval, shifted in frequency from the pump. However, the apparatus required is still rather complicated. The complication arises because the Raman power is very low and many orders of magnitude weaker than the pump power. An overview of the apparatus is given in this chapter. Further details, such as specifications, calibration, and alignment procedures can be found in Chapter 8.

7.1 Pump lasers

Two pump lasers were used in the experiments. The first laser was a small frame, krypton ion laser. This was operated using a linear cavity with high reflecting mirror and output coupling mirror. An intracavity prism at the high reflector end restricted laser action to one atomic transition. In this configuration the laser produced a linearly polarized, continuous wave output. In most of the experiments the 647.088nm transition was used but some results were also obtained with the 676.488nm transition (for details of the atomic transitions see[56]). The cavity length was approximately 1.4m and no attempt was made to restrict the number of longitudinal modes oscillating. The linewidth for both wavelengths is greater than 1GHz. The maximum output power used in the experiments was about 150mW, considerably less than the maximum power available from such a laser system.

The second laser was identical to the first, except that the intracavity prism incorporated an acousto-optic mode locker and an acousto-optic cavity dumper was used in place of the output coupling mirror. The laser

was linearly polarized with the same polarization direction as the first laser and was operated only on the 647nm transition. The mode locker (Coherent model 467-SEM) forces a pulse to circulate in the cavity. The round trip frequency for the pulse was about 2×37.644MHz (cavity length approximately 2m). The cavity dumper (Coherent model 7200) acts as a mirror with a transmission that can be rapidly switched. In operation, the transmission is essentially zero and a pulse circulates in the cavity, growing in intensity. After a number of round trips specified by the divide by number in the drive electronics, the transmission is abruptly switched to about 70% and a single pulse is dumped out of the cavity. The transmission then returns to zero, and the light that remains in the cavity grows into the next pulse. Typically the divide by number used was 32 which means that a pulse completes 64 cavity round trips before being dumped. This gives a pulse repetition rate for the laser of 37.644MHz/32. It is known that the pulses produced by this laser have an approximately $sech^2$ shape (optical power as a function of time), a duration (full width at half maximum) of about 60ps and a nearly transform limited frequency spectrum. The pulse duration could be measured using a 25GHz photodiode (Newport model 1431) and digitizing oscilloscope (Hewlett Packard 34GHz test set model 54123A and mainframe model 54120B). The maximum average power available from the laser was about 90mW which corresponds to peak powers in excess of 1kW. Further details relating to the pulsed laser can be found in [31], [45] and [63].

7.2 Input optics

The optics used to guide light from the laser to the fibre under test are shown in Figure 7.1. The laser mirror was a high reflector designed for the 647nm and 676nm krypton lines with a radius of curvature of 3m. The curvature was useful in collimating the beam, reducing spot size at the microscope objective and improving coupling with the fibre. The prism (Broomer part number 20-1101) was made of highly dispersive dense flint glass. Combined with apertures #a, #b and #c, the prism forms a simple monochromator [52], allowing only a narrow range of wavelengths (including the pump) to pass from the laser to the fibre (a monochromatic source is required for these experiments and the laser produces a significant amount of white light due to the recombination of free electrons and ions in the plasma tube). The polarization of the beam was such that it met the prism at an angle very close to Brewster's angle, giving minimal loss. Reflecting the beam back through the prism is a convenient means of doubling the angular dispersion [52, p98]. The apertures #b and #c also provided a convenient means of
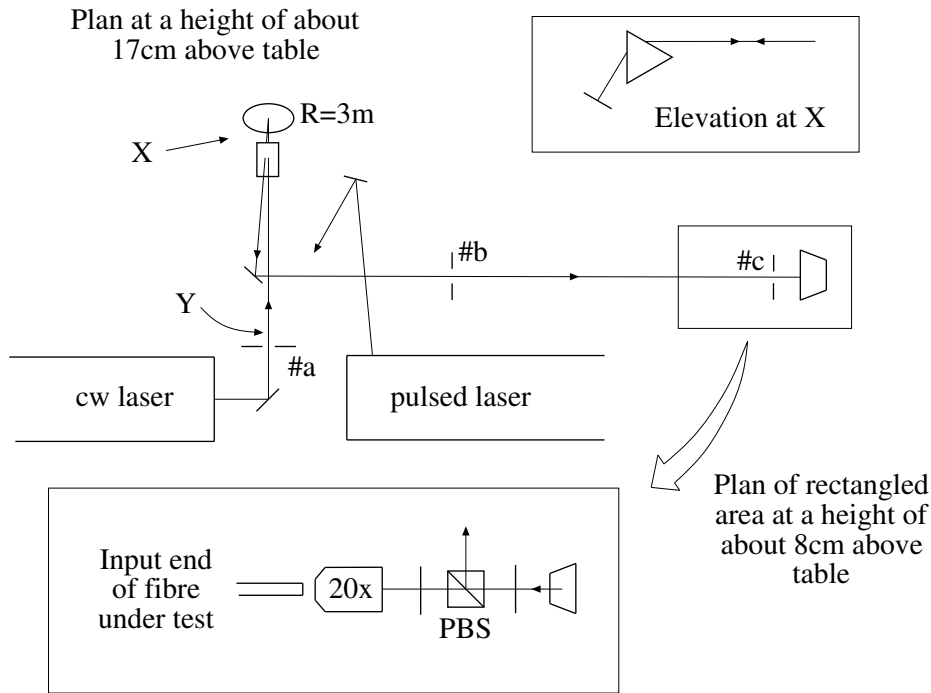
Figure 7.1: Input optics. Plan means view from above. Elevation means view from the side. #a, #b and #c are circular apertures with a diameter of about 2.5mm. R=3m is a laser mirror. Adjacent to R=3m is an equilateral prism. After aperture #c, the beam hits an aluminium mirror tilted at 45^0 to reflect the beam vertically downwards. A second aluminium mirror reflects the beam back to the horizontal plane. All other mirrors were of the dielectric type, designed for use across the visible spectrum. PBS denotes polarizing beam splitter. The PBS is flanked on either side by half wave plates. 20x denotes a 20x microscope objective. Some approximate distances are:- 60cm from #a to prism, 40cm from prism to 45^0 mirror, 80cm from 45^0 mirror to #b, 120cm from #b to #c and 25cm from lower aluminium mirror to 20x. To use the pulsed beam in place of the cw beam (shown), a dielectric mirror was inserted at Y, reflecting the pulsed beam towards the prism.

aligning other sources to the fibre (see Section 7.3).

The half wave plate in front of the 20x was used to align the polarization of the pump with the axes of the fibre (this will be discussed further in Section 7.5). The PBS (Newport part 05FC16PB.5, a dielectric cube type designed for the wavelength range 620nm to 1000nm) combined with the remaining half wave plate to make a variable attenuator (the beam leaving the right angled port of the PBS terminated at a beam stop). In some experiments additional attenuation was obtained by placing a semi-silvered microscope slide in front of the 20x. In some experiments involving the FS-HB-3611 fibre (a fibre which has very lossy cladding modes; see Section 7.4) attenuators were dispensed with all together and the pump power propagating in the fibre was controlled by misaligning the fibre input.

7.3   White light source

A white light source was necessary both for alignment and calibration. The source used is shown in Figure 7.2. The white light power, measured after the 20x objective, was typically about 70nW (this is difficult to measure because of the broad spectrum). About 30nW of this could be coupled into the test fibre.

It might be worth pointing out that the amount of light which can be coupled by a system of lenses from a source into a single mode fibre, is ultimately limited only by the radiance [68, p11] of the source (to see this apply the principle of reversibility of light [68, p36]). For a thermal source, the radiance is determined by the temperature. Hence the choice of a tungsten/halogen bulb. Much greater radiances can be obtained using the fluorescence from a dye or titanium sapphire laser but at a cost of much increased complexity.

7.4   Test fibres

Measurements were made using two fibres, both of which preserved polarization.

The first fibre was a polarization preserving (HiBi) manufactured by 3M (part number FS-HB-3611). The fibre was designed for the HeNe wavelength (632.8nm) with manufacturer's specifications (taken from the fibre spool) of

- Attenuation of 34dB per kilometre at a wavelength of 630nm.

- Mode field diameter of 3.7μm.

- Numerical aperture of 0.13 (nominal).
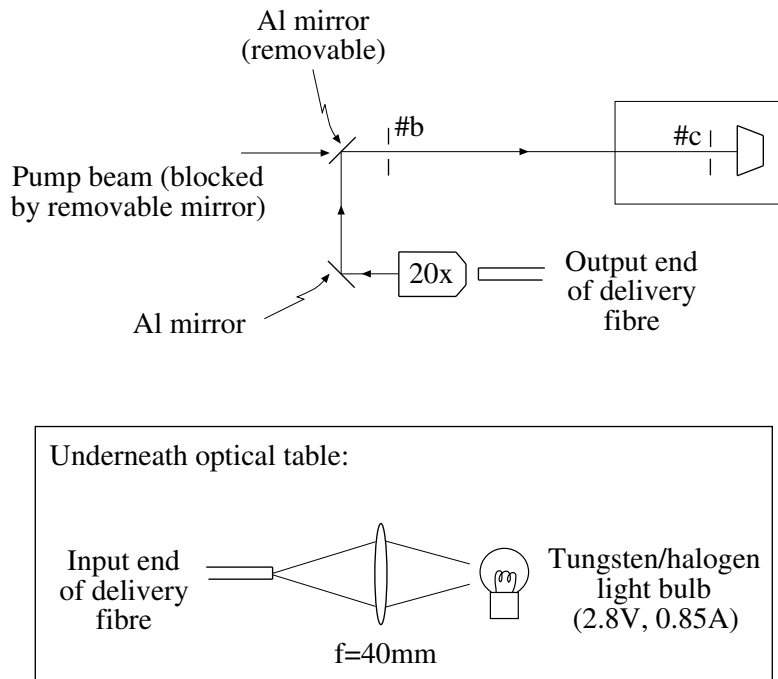
Figure 7.2: Plan showing white light source. #b and #c are the same apertures which appear in Figure 7.1. The delivery fibre was 4.8m of FS-SN-3224 (manufacturer is 3M) which is a single mode, non-polarization preserving fibre, designed for the HeNe wavelength. The input end of the fibre was located underneath the optical table, partly to save table space, but also to help reduce stray light.

- Birefringence of 4×10^{-4}.

- Single mode cut-off at 550nm.

Unfortunately, this was the only information provided with this fibre. It is believed that the fibre was manufactured using 3M's 'shaped cladding' technique (see the catalogue published by 3M entitled '3M speciality single-mode fiber products'). This results in an elliptically shaped stress element in the cladding while preserving a circular core. Comments made in [29] suggest that the fibre has a core with a low level of Ge doping (perhaps as low as 2%), the cladding having a refractive index reduced in comparison to fused silica.

The fast and slow axes of the fibre could be identified unambiguously using cross-phase modulation instability (XPMI, see [30] and [71]). This is a type of four wave mixing which produces a Stokes beam and an anti-Stokes beam from two beams, degenerate in wavelength, propagating on the linear polarization axes of the fibre. The Stokes beam grows on the slow axis and the anti-Stokes beam on the fast axis, allowing the axes to be identified. Experimentally it was found that the fibre preserved polarization well across the entire visible spectrum (see Section 8.6). The cladding modes of the fibre were confirmed to be very lossy (with 8mW of pump light leaving a 40m length of fibre at optimal input coupling, small misalignment of the input reduced the output power to 10nW, even though the same amount of optical power was incident on the cladding front face).

At wavelengths below 670nm the transmission of the two axes of the fibre were found to be nearly equal. However, for wavelengths above 730nm, the transmission of the fast axis relative to the slow axis was essentially zero (that is the fibre acted as a polarizer). Such behaviour has been observed previously (see [79] and [94]). It is *assumed* that the transmission of the slow axis did not have such a strong wavelength dependence (note from Section 6.5 that wavelength independent loss will be assumed when interpreting the data from Raman experiments).

The second fibre was an experimental fibre made by Stolen at the Bell Telephone Laboratories. No data from the manufacturing stage was available for this fibre. The fast and slow axes of the fibre could be identified using polarization modulation instability (PMI, see [62] and [96]). This is a four wave mixing process which produces Stokes and anti-Stokes beams on the fast axes of the fibre from a single beam propagating on the slow axis of the fibre. From the measured frequency separation of the Stokes and anti-Stokes beams, the birefringence was inferred to be 5×10^5 [63]. Note that some pieces of fibre produced weaker Stokes and anti-Stokes beams than other pieces of the

same length, suggesting that the original drawn fibre was not uniform along its length. Measurements of the mode field radii (see Section 8.8) suggest the fibre has an approximately circular core. Unlike commercial fibres, the cladding of the Stolen fibre acted as a low loss, multimode waveguide. Light originating from the cladding modes could be used to form an image of the output end of the fibre. This image suggested that the cladding contains an elliptical element. In the Raman experiments, a cladding mode stripper was positioned near the input end of the fibre. The stripper was fabricated by first removing about 5cm of the fibre jacket, coating the exposed cladding with glycerol (which has a refractive index nearly equal to fused silica) and then resleeving the section of fibre with black plastic tubing (the jacket from an electrical cable). Most of the light launched into the cladding modes is then absorbed by the black plastic.

In all experiments care was taken to avoid excessive bending of the fibres.

7.5 Polarization selection

The optics after the fibre are shown in Figure 7.3. The fibre output was collimated with a 10x microscope objective. This was anti-reflection coated (presumably for visible wavelengths) and had a measured transmission of 96% at a wavelength of 647nm. The PBS after the 10x was a Thompson prism (Melles Griot part number 03 PTB 001/A) This has a very broad wavelength range (350nm to 2.3μm) and was anti-reflection coated for visible wavelengths. The output end of the fibre was oriented so that light from one fibre axis (take, for example, the fast axis) passed undeflected through the PBS and into a beam dump. Light from the slow axis continued on for measurement. The half-wave plate in front of the 20x could be used to launch the pump on either the slow axis (for parallel scattering experiments) or fast axis (for perpendicular scattering experiments).

7.6 Measurement of pump power

The pump power was measured using a photodiode based power meter (Newport 818-UV photodiode, 883-UV filter and 815 meter box). The diode and filter were positioned between the 10x and PBS during a power measurement. It was necessary to keep the power incident on the 818-UV below about 90μm or its response became nonlinear (see Section 8.3.3).
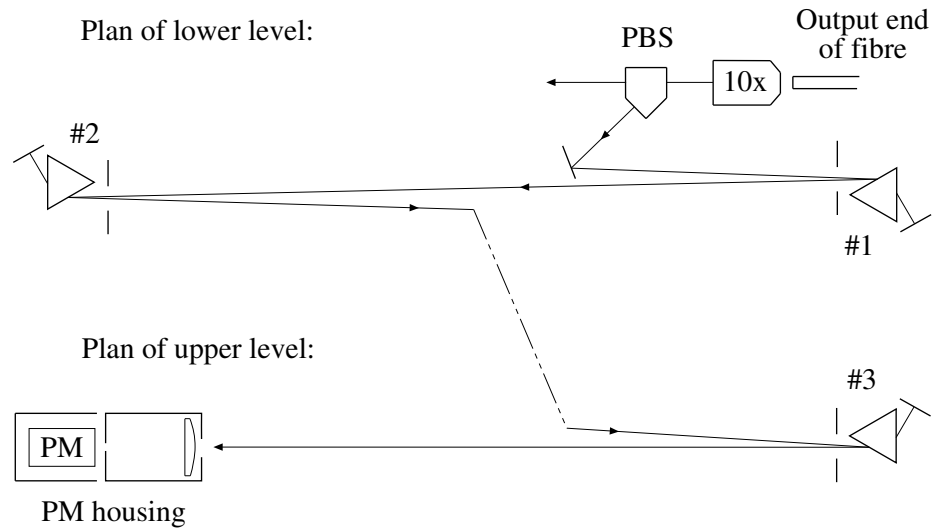
Figure 7.3: Output optics.   The output optics were constructed on two levels, the upper level being directly above the lower level.   In this view from above an artificial sideways displacement has been introduced. In reality the PM housing was directly above assembly #2, and assembly #3 directly above assembly #1. 10x denotes 10x microscope objective.   PBS denotes polarizing beam splitter.   PM denotes photomultiplier.   Note that the PM housing consists of two separable halves, all the optics being in the front half. Approximate beam heights above the table at some locations are:- 8cm at fibre output and PBS, 8.5cm at #1, 11.5cm at #2, 17.5cm at #3 and 18cm at the PM housing. Approximate horizontal separations between components are:- 10cm 10x to PBS, 10cm PBS to angled mirror, 110cm angled mirror to #1, 300cm from #1 to #2 (and likewise for #2 to #3 and #3 to PM housing).

7.7 Monochromator

The remaining optics in Figure 7.3 consists of dielectric mirrors (all designed for operation across the visible spectrum), prisms (all Broomer 20-1101; see Section 7.2), apertures and the front half of the PM housing. The polarization of the light was such that it met the surfaces of the prisms at approximately Brewster's angle, giving minimal loss. The apertures at #1, #2 and #3 were rectangular slits with long sides oriented vertically and short sides of approximate length 5.5mm, 4.5mm and 5mm (respectively). The aperture at the front of the PM housing was circular with a diameter of about 6mm. The plano-convex lens inside the housing had a focal length of 25cm and was anti-reflection coated for visible wavelengths. A second circular aperture of diameter 1mm was positioned in the housing 25cm behind this lens. The active area of the PM tube (2.5mm diameter) was located immediately behind this 1mm aperture.

The optics constitute three prism monochromators (see Section 7.2) in cascade (a triple monochromator). In operation, all three monochromators are aligned to the same centre wavelength. This allows a narrow range of wavelengths (chosen to exclude the pump) to reach the photomultiplier. The photomultiplier can then be used to measure the optical power of any Raman scattered light in this wavelength interval (assuming that Raman scattering is the only source of frequency shifted light).

Three monochromators are necessary because not all the pump light propagates as geometrical optics would suggest (some is diffracted and some is scattered). This means that at each monochromator stage, a small fraction of the pump light which enters the stage, emerges propagating colinearly with the wavelength range of interest. Three stages are required to achieve adequate suppression of this scattered pump light (the pump power leaving the fibre can be 12 orders of magnitude greater than the Raman power at the photomultiplier).

7.8 Neutral density filters

In some experiments the Raman light arriving at the PM housing had sufficient intensity to damage the PM tube (the Raman light is always weak but the PM tube is a very sensitive detector). To avoid damage, the intensity of the Raman light was reduced using neutral density filters. These were held in a rack positioned immediately in front of the PM housing. Three filters were available; Edmund 30934 (32% transmission), Edmund 30936 (5% transmission) and Edmund 30938 (1% transmission). The rack allowed the

filters to be used either singly or in any combination.

It would seem appropriate to add a caution about the reliability of these filters. With short coherence length sources (such as the spectrally filtered Raman light) their transmission is reliable. However, it is not wise to use these filters with long coherence length sources (such as lasers) since Fabry-Perot effects can cause the transmission to vary strongly with tilt angle and temperature. For example, with a HeNe laser the transmission of the 1% filter was found to vary by about 30% with changes in tilt angle of only a few degrees.

7.9   Photomultiplier tube and electronics

The photomultiplier used was an EMI 9863A/100 (serial 54686). This tube has a high gain (14 dynodes) so that it can be used to count single photons. In addition, the dynodes are arranged in the linearly focussed geometry, giving a small spread in transit times for the secondary electron. This means that the tube can time the arrival of single photons with sub-nanosecond resolution. The photocathode is of the S20 material (giving appreciable sensitivity in the red and near infrared) and its diameter is reduced to 2.5mm by internal focussing (a small sensitive area is not a limitation for experiments involving well collimated beams, and it has the advantage of low dark counts). The dynode material is BeCu.

The PM tube was installed in a PM housing (Pacific Precision Instruments model 3262RF). This housing was for room temperature operation only. The housing also contained a mu-metal shield to minimize the effects of external magnetic fields and a voltage divider to charge the dynodes to the appropriate potential. The voltage divider is drawn in Figure 7.4.

The high voltage power supply used was a Fluke 415B set at -1950V. The choice of supply was important; an Ortec 446, supplied from the mains by an auto transformer, had to be removed from the experiment because it introduced too much noise into the electronics. The pulses produced at 'signal' by weak, cw light incident on the PM tube, were observed by connecting a 50Ω, 500ps per division, analogue oscilloscope. The pulses were observed to have a FWHM of about 3.5ns. The amplitude of the pulses varied stochastically with a maximum amplitude of about -80mV.

A schematic of the electronics used to process the pulses is shown in Figure 7.5. The signal was first amplified by a 10x, 2ns pulse amplifier based on the LeCroy VV100B integrated circuit. The amplified signal was then passed to a constant fraction discriminator (CFD) (Tennelec TC455). CFDs are usually used to improve timing precision. In this experiment this was
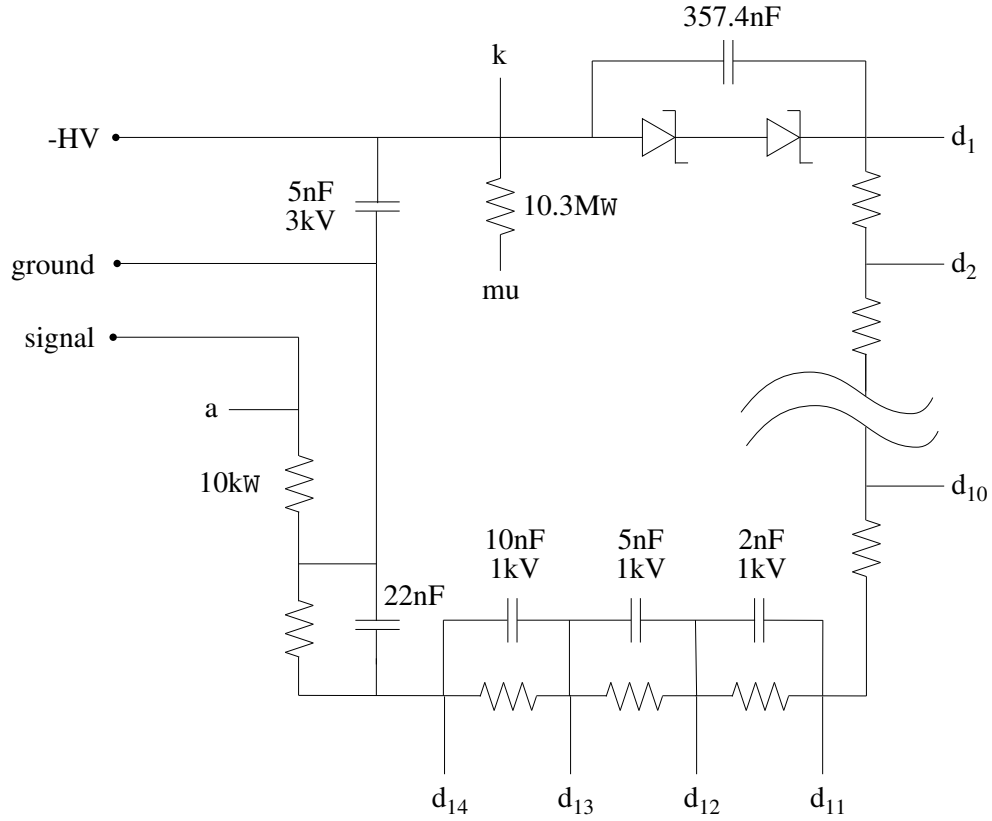
Figure 7.4: Voltage divider used with photomultiplier. The following abbreviations are used:- HV for the live terminal of a high voltage power supply, k for cathode, d_j for the jth dynode, a for anode and mu for mu shield. The zener diodes are 1N5276 (Zener voltage of 150V). Unless otherwise stated, the resistors are $200k\Omega$, $\frac{1}{4}$W. The ground is common to both the signal and the high voltage power supply.

not particularly important but the CFD was still useful for three reasons. Firstly, it converted the amplified pulses (which vary in shape stochastically from pulse to pulse) to a standard voltage pulse (-1V amplitude and 100ns duration). Secondly, it provided a threshold discrimination (set to the minimum of 5mV) so that small pulses of electrical noise would not be interpreted as counts. Thirdly, it had an adjustable blocking width, set to 100ns, which meant that, after a pulse was registered, 100ns elapsed during which time any subsequent pulses were ignored, providing good immunity to PM afterpulsing and to electrical reflections caused by small impedance mismatches in the electronic circuits. The standard pulses were then sent to an Ortec 430 scaler for counting. The scaler was under the control of an Ortec 773 timer/counter, providing a convenient means of measuring the number of counts in a predetermined sample time (usually 1s).

A second, independent signal from the CFD was sent to the pulse averager shown in Figure 7.6. This provided a continuous read out, proportional to the count rate at the PM. The least significant digit on the DVM corresponded to a precision of 0.1mV.

With this tube and electronics the dark count rate was typically of the order 30cps (counts per second), and the DVM would read 0.0mV.

The manufacturer specifies a number of ratings which, if exceeded, will result in damage to the tube. The most relevant when using the voltage divider shown in Figure 7.4 is the maximum anode current, specified as 200μA. Assuming the pulses at 'signal' have an amplitude of 50mV and duration 3.5ns, this corresponds to a count rate of approximately 50×10^6cps. In a preliminary experiment the count rate was allowed to reach 500×10^3cps. This was found to cause a small, temporary increase in the count rate. As a consequence, in all subsequent measurements, the count rate was kept below 100×10^3cps (corresponding to about 23.0mV on the DVM).
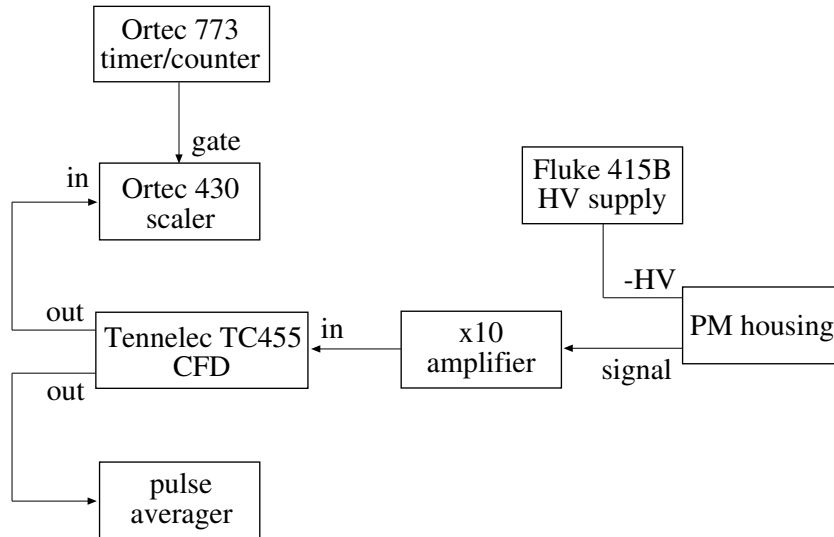
Figure 7.5: Schematic of the electronics used to process the signal from the PM. HV is high voltage. CFD is short for constant fraction discriminator. The arrows indicate the direction of information flow.
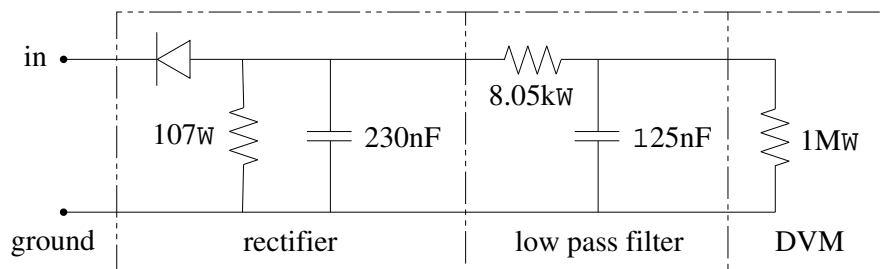
Figure 7.6: Circuit diagram for pulse averager. DVM stands for digital voltmeter.

Chapter 8

Apparatus calibration

This chapter is mainly concerned with calibration of the apparatus described in Chapter 7. The exceptions are Section 8.2, which discusses apparatus performance, and Section 8.5, which discusses experimental procedure. Note that the uncertainties quoted are estimates of standard deviation, rather than 90% confidence limits.

8.1 Output coupling loss

In the experiments, all quantities were measured after the 10x objective (see Figure 7.3). The objective had a measured loss at 647nm of 4% (there was also a 4% reflection loss at the end of the fibre due to Fresnel reflection). These losses represent small corrections. It therefore makes sense to make an approximation that they are independent of wavelength. The losses then cancel for spontaneous scattering experiments (see Section 6.5). In the stimulated scattering experiments, the measured pump powers and PM count rates have been multiplied by 1.085 to correct for these losses.

8.2 Monochromator pump extinction, transmission and dispersion

The monochromator shown in Figure 7.3 was the culmination of a sequence of experiments investigating pump extinction in different monochromator designs. In these experiments, a single beam with wavelength components at both 632.8nm and 647.1nm was utilized. This beam came from the output port of a beam splitter which had a HeNe beam incident on one input port and the cw pump laser incident on the other input port. Prior to the beam

	Double	Triple
Count rate with beam stop inside pump laser cavity.	1.40×10^3cps	350cps
Count rate and laser power entering monochromator.	400×10^3cps 1.3mW	1.54×10^3cps 43.8mW
Fraction of pump photons entering monochromator which reach PM.	2.7×10^{-9}	3.1×10^{-13}

Table 8.1: Comparison of pump extinction between double and triple monochromators. The count rates are the count rates recorded by the PM. For the first row of the table, the beam stop was placed inside the laser cavity at the high reflector end. This prevented laser action but meant that the laser still acted as a source of white light. In the third row of the table a quantum efficiency of 3.5% has been assumed for the PM (see Section 8.4.1).

splitter, the HeNe beam was collimated using a beam expander (two plano-convex lenses of focal length 20mm and 100mm) and the pump beam had any white light removed (as discussed in Section 7.2). The dual wavelength beam was reflected into the monochromator by a mirror inserted after the PBS in Figure 7.3. No fibre was used in these experiments.

The monochromator was aligned to 632.8nm by directing the HeNe component of the dual wavelength beam through the centre of the apertures at #1, #2, #3 and the front of the PM housing (the PM housing had an internal beam stop to protect the PM from the intense light). The HeNe beam was then switched off and the count rate at the photomultiplier recorded. Since the only light source in the lab was the pump laser, any counts must come from scattered pump light (the dark counts turn out to be negligible). Results obtained with the triple monochromator in Figure 7.3 and also with a 'double' monochromator are summarized in Table 8.1. The design of the double monochromator was identical to that of the triple monochromator; it just had one fewer stage.

These results, when compared with some preliminary Raman data, demonstrated, firstly, that a triple monochromator was going to be essential for Raman measurements, and secondly, that the monochromator design in Figure 7.3 would be adequate. The experiments also demonstrated that good pump extinction is only obtained when the prisms and mirrors are kept clean and the apertures kept as small as possible (the apertures must not diffract the pump). In addition it was necessary to position black cardboard screens to shade the PM from the strongest sources of Rayleigh scattered light (for example, a screen was necessary along the line of sight between the PM and assembly #1).

The high pump extinction was also obtained without incurring significant

loss. With a laser coupled into the slow axis of the test fibre, the monochromator aligned to the laser wavelength, and the back half of the PM housing removed, the transmission from after the 10x to behind the PM housing could be measured. The transmission was found to be approximately the same for laser wavelengths of 632.8nm (HeNe), 647.1nm (pump) and 676.5nm (pump) with an average value of 82.4%.

The dual wavelength beam also allowed the angular dispersion of a single monochromator stage to be measured. After reflecting a distance of 265cm from #1, the 632.8nm and 647.1nm components were found to have separated by a distance of 18mm, giving a figure of 4.7×10^{-4}rad/nm for the angular dispersion.

8.3 Calibration of Newport power meter

8.3.1 815 meter box (serial 1463)

When the 818-UV photodiode is exposed to light it acts as a current source. The 815 meter box is essentially just an ammeter. A trim pot on the 815 (labelled 'cal') can be used to change the calibration of the meter's scale. The position of the trim pot can be monitored by disconnecting the photodiode and pushing the button labelled 'cal'. Throughout the experiments the trim pot was adjusted so that cal=309.

The 815 was calibrated by connecting a series circuit consisting of it, the 818-UV and an ammeter. The amount of light incident on the 818-UV was then varied and a graph of 815 reading verses ammeter reading constructed.

When the 815 was operated on the 10μW range, the graph was found to be a straight line through the origin with gradient 3.134W/A. On the 1μW range the same graph had a gradient steeper by about 1 part in 300. Similarly on the 100μW range the same graph had a gradient shallower by about 1 part in 300.

The uncertainty in these results is less than one percent. For the purposes of this thesis, this uncertainty is not significant and may be neglected.

8.3.2 883-UV filter (serial 0800)

The transmission of the 883-UV filter was calibrated as follows. With a laser coupled into the fibre, the 818-UV photodiode was positioned after the 10x microscope objective (see Figure 7.3) and the signal measured with the 815 meter box. The 883-UV filter was then attached to the 818-UV and the signal remeasured. The optical power was then varied by misaligning the

input to the fibre and a graph of signal with the filter verses signal without the filter constructed. The graph was a straight line with gradient equal to the transmission of the filter. The results obtained are shown in Table 8.2.

Laser	Wavelength	Transmission of 883-UV
Kr+	647.1nm	0.8620×10^{-3}
Kr+	676.5nm	0.8294×10^{-3}
Laser diode	774.5nm	0.9728×10^{-3}

Table 8.2: Measured transmission of 883-UV filter.

The transmission of the filter shows a weak dependence on its tilt angle relative to the incident beam. This makes the values of the transmission uncertain by about 1%.

8.3.3   818-UV photodiode (serial 0800)

A detector calibration report was available for the 818-UV photodiode. This was prepared by the manufacturer and specified the responsivity of the 818-UV in terms of A/W. Notice that if the responsivity of the 818-UV is known then the 818-UV and 815 can be used together to make absolute measurements of optical power (since the reading on the 815 can be converted to a current which can in turn be related through the responsivity to the optical power incident on the 818-UV).

The detector calibration report specifies the responsivity for wavelengths from 250nm to 1100nm in steps of 10nm (the responsivity at arbitrary wavelengths can be found by interpolation). The accuracy of the calibration report is ±2% for a specified time period (11.11.94 to 11.11.95). Unfortunately the Raman measurements were made after this period had elapsed.

The accuracy of the manufacturer's calibration report can be checked by comparing the response of the 818-UV with that of a reference detector. Two reference detectors were available.

The first reference was a Newport 818-SL photodiode (serial 7004). At the time of use, the manufacturer's calibration report for this photodiode was still valid. As for the 818-UV, the calibration report specifies the responsivity at 10nm intervals with a quoted accuracy of ±2%.

The responsivity of the 818-UV can be measured using the 818-SL as follows. A laser is coupled into the fibre, the 818-UV connected to the 815 meter box, and the 818-UV positioned after the 10x objective (see Figure 7.3). The signal indicated by the 815 is recorded. The 818-UV is then exchanged for the 818-SL and the signal recorded again. The laser power was varied

and a graph plotted. The graph was found to depart from linearity when the current flowing in the 818-UV exceeded about $28\mu A$ (the exact point of departure depending on the area of the 818-UV illuminated). The gradient of the linear part of the graph gives the ratio of the responsivities of the two photodiodes. Hence, if the 818-SL calibration report is assumed correct, the responsivity of the 818-UV can be inferred.

The second reference was a Laser Precision Corp RkP-545 (serial 183) / Rk-5100 (serial 198) pyroelectric radiometer. This has a response which is nominally independent of wavelength. The instrument was calibrated by the manufacturer with a quoted accuracy of $\pm 1.5\%$. Unfortunately this calibration was performed in 1979 and was only valid for six months.

By measuring the power of a laser beam leaving the fibre with, first, the radiometer and, second, the 818-UV/883-UV/815 combination, the responsivity of the 818-UV was measured. As always a graph was plotted and the gradient taken. The radiometer was unable to measure beams weaker than $100\mu W$ and this made it necessary to use the 883-UV filter with the photodiode. Note that using the filter increases the random error (see Section 8.3.2).

The responsivity values are summarized in Table 8.3.

Laser	HeNe	Kr$^+$	Kr$^+$	laser diode
Wavelength	632.8nm	647.1nm	676.5nm	774.5nm
Cal sheet	0.4245	0.4360	0.4569	0.4884
First ref	0.4027	0.4133	0.4316	0.4802
Second ref	-	0.4236	0.4412	0.5018
mean	0.4136	0.4243	0.4432	0.4901

Table 8.3: Responsivity values for the 818-UV photodiode. The units are A/W. The first row of values are those taken from the manufacturer's calibration sheet. The second row of values are measurements made using the 818-SL. The third row of values are measurements made using the pyroelectric radiometer.

If the uncertainties quoted by the manufacturers represent one standard deviation then these values are just consistent. It therefore seems sensible to average the responsivities at each wavelength but retain the same uncertainty (i.e. $\pm 2\%$).

8.4 Calibration of monochromator and PM tube

For the purposes of this section the test fibre is the FS-HB-3611 oriented with its output end such that light from the slow axis of the fibre was directed by

the PBS into the monochromator (see Figure 7.3).

8.4.1   Collection efficiency

As discussed in Section 6.3, the collection efficiency, η, is the product of two factors, the transmission of the optics and the quantum efficiency (QE) of the PM tube (quantum efficiency is the fraction of photons incident on the sensitive area of the tube which actually result in a count). The measured transmission of the optics at red wavelengths is 82.4% (see Sections 8.1 and 8.2). The manufacturer's estimate of the QE of the S20 photocathode is shown in Figure 8.1. Combining these two pieces of information gives the circles in Figure 8.2.
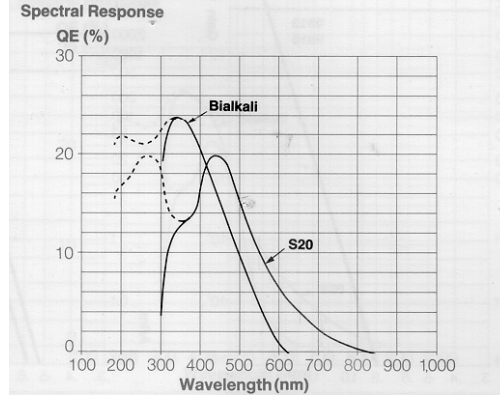
Figure 8.1: Quantum efficiency of photocathode (S20) for EMI 9863 photomultiplier tube (from data provided by the manufacturer).

There are two problems with this approach. Firstly, the monochromator was constructed using optics for visible wavelengths (reflective and anti-reflective dielectric coatings), so 82.4% might not be an appropriate value for the transmission of the optics at near infrared wavelengths. Secondly, while the manufacturer's graph of QE can be read with reasonable precision for wavelengths in the green and yellow, the same cannot be said for wavelengths in the red and infrared. With these problems in mind, measurement of the collection efficiency at some wavelengths in the red and infrared was felt to be essential.

The measurements were made by aligning a laser to the slow axis of the fibre and then aligning the monochromator to the wavelength of the laser. Measurement of the optical power after the 10x objective with the Newport

818-UV/815 allowed the photon flux at this point to be calculated using $E = h\nu$. Comparison with the count rate at the photomultiplier allowed the collection efficiency to be determined. Because fluxes measurable with the PM tube do not overlap with fluxes measurable with the 818-UV, it was necessary to use optical filters in front of the PM tube housing. These filters must have a stable transmission when used with monochromatic sources (see Section 7.8) and be free of wedge. The filters were spaced apart by about 20cm so that the 818-UV could be positioned on either side of each filter and its transmission determined. A combination of poor input alignment and optical filters positioned in front of the 20x objective was used to restrict the laser power propagating in the fibre to of the order 1μW.

The measurements made and the results obtained are summarized in Table 8.4.

Laser	HeNe	Kr$^+$	Kr$^+$	laser diode
Wavelength	632.8nm	647.1nm	676.5nm	774.5nm
Filters	30GN25	30GN25	30GN25	30GN25
used and	1.157×10^{-3}	1.270×10^{-3}	2.148×10^{-3}	5.807×10^{-3}
their	blue	blue	blue	03FNQ069
measured	12.89×10^{-3}	6.497×10^{-3}	1.865×10^{-3}	2.061×10^{-3}
trans-	VG 9	VG 9	VG 9	
mission	16.86×10^{-3}	10.21×10^{-3}	4.986×10^{-3}	
η	0.03921	0.03618	0.03031	0.007023

Table 8.4: Results for the collection efficiency measurements. 30GN25 is an absorption type filter from Comar. 03FNQ069 is a semi-silvered type filter from Melles Griot. The blue filter was an absorption type device. VG 9 is a green absorption filter from Spindler and Hoyer.

The random error in the collection efficiency values was found to be of the order 2% (the HeNe value has a larger error, perhaps 3%, because of intensity noise with the HeNe laser). However, the measurements also inherit the 2% uncertainty in the calibration of the 818-UV (see Section 8.3.3) so the overall error is more like 3%.

The collection efficiencies in Table 8.4 are plotted as crosses in Figure 8.2. The curve is a best fit for the collection efficiency. This curve was used in processing data from Raman experiments. The uncertainty in the curve for wavelengths between 700nm and 750nm is obviously greater than 3%.

The transmission of the monochromator (from after the 10x objective to in front of the PM housing) was also measured at 774.5nm and found to be about 68%.
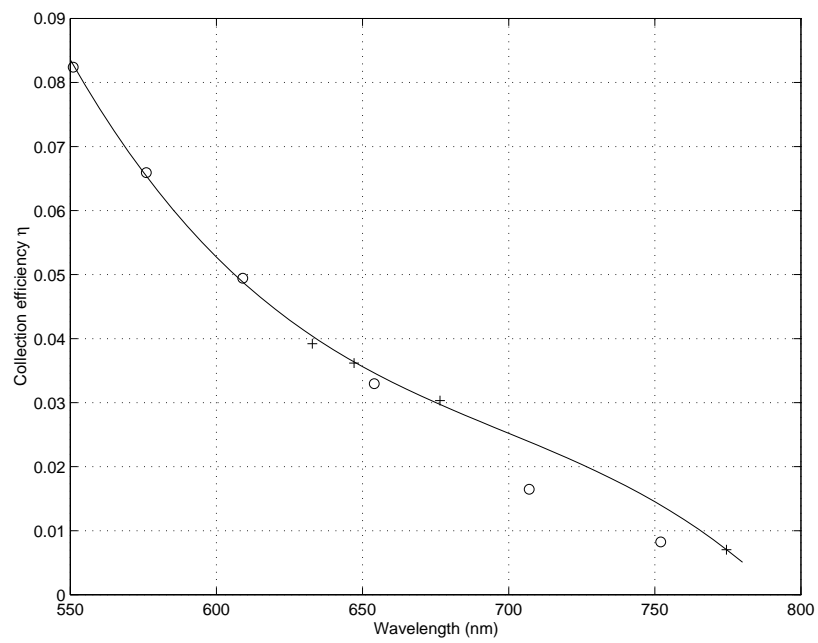
Figure 8.2: Collection efficiency η of monochromator and PM tube. Circles are the transmission of the optics at red wavelengths multiplied by quantum efficiencies taken from Figure 8.1. Crosses are measured values.

8.4.2 Centre wavelength (preliminary estimates)

The mirror mounts at #1, #2 and #3 (see Figure 7.3) consisted of a metal plate held by springs against three pivot points. One pivot point was a ball bearing, the other two, micrometers with a pitch of 500μm per revolution. One micrometer tilted the metal plate about a vertical axis (horizontal adjust) and the other about a horizontal axis (vertical adjust). The spacing between a micrometer pivot and ball bearing pivot was about 4.5cm. Reading the micrometers allowed the alignment of the mirrors to be quantified.

With the rear half of the PM housing removed (see Figure 7.3), the pump beam (647.1nm) coupled into the fibre under test, and the monochromator aligned so that the beam passed through the centre of the apertures of #1, #2, #3, and PM housing, the position of the micrometers was recorded. This was then repeated with five other laser wavelengths (676.5nm and 568.2nm from the krypton laser, 514.5nm from an argon ion laser, 632.8nm from a HeNe laser and 793nm from a laser diode). Note that it was possible to get good alignment by adjusting only mirrors#1, #2 and #3; the optics in the PM housing did not need to be touched. The data from these experiments was used to construct preliminary calibration curves (wavelength verses micrometer reading) for all six micrometers. The quantity specified in the calibration curves is the position of the micrometers at wavelength λ *relative* to the position of the micrometers at 647.1nm. The setting of the horizontal adjust of the mirror at #1 (which will be denoted ha#1) is of particular interest, since it determines the centre wavelength of the monochromator.
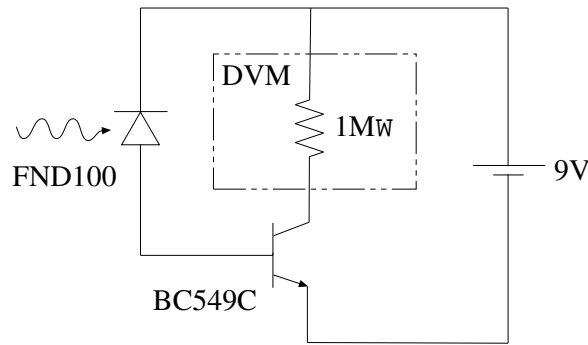
Figure 8.3: Schematic for photodetector. FND100 is a silicon photodiode manufactured by EG&G. DVM is digital voltmeter.

8.4.3   Centre wavelength and bandwidth

Following on from Section 8.4.2, the white light source (see Section 7.3) was coupled into the test fibre and ha#1 set arbitrarily to −0.22mm. The rest of the monochromator was then aligned using the preliminary calibration curves. The alignment was then optimized by adjusting iteratively (sometimes called 'walking'), first, the horizontal adjust of mirror #3, then, second, the horizontal adjust of mirror #2, until the optical power at the back of the PM housing was maximized. A schematic for the photodetector used to measure the power at the back of the housing is shown in Figure 8.3.
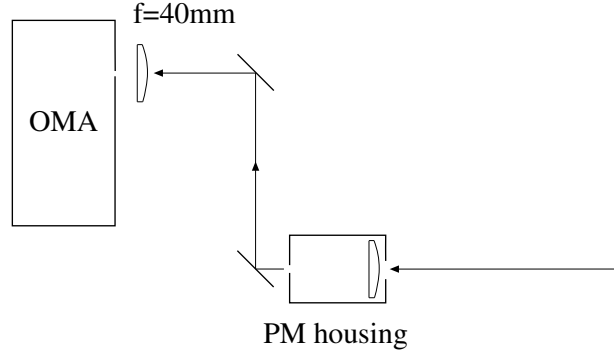
Figure 8.4: Plan of apparatus used to measure spectrum of white light after propagation through the monochromator. OMA is optical multichannel analyser. The f=40mm planoconvex lens focussed the light onto the entrance slit of the OMA. With this arrangement, the transmission of the slit to a monochromatic beam from the fibre was about 95%. The two mirrors used were aluminium and were about 50cm apart. The distance between the second mirror and the f=40mm lens was about 20cm.

Once the alignment had been optimized, the photodetector was removed and the spectrum of white light leaving the monochromator optics measured with the apparatus shown in Figure 8.4.   The OMA used consisted of a grating spectrometer (Thermo Jarell Ash Corp monospec 27) and a silicon photodiode array (EG&G PARC 1453A). The entrance slit on the monospec 27 was 50μm wide and the grating used was grating number 3 on the turret. For red wavelengths this gave a separation between pixels of about 0.03nm and an impulse response of about 0.2nm (this is the measured FWHM of the spectral lines of a low pressure Neon lamp held in front of the entrance slit; these spectral lines were also used to calibrate the wavelength axis). The photodiode array was operated with an integration time of 0.3s and each measurement was made five times and the results averaged. The resulting
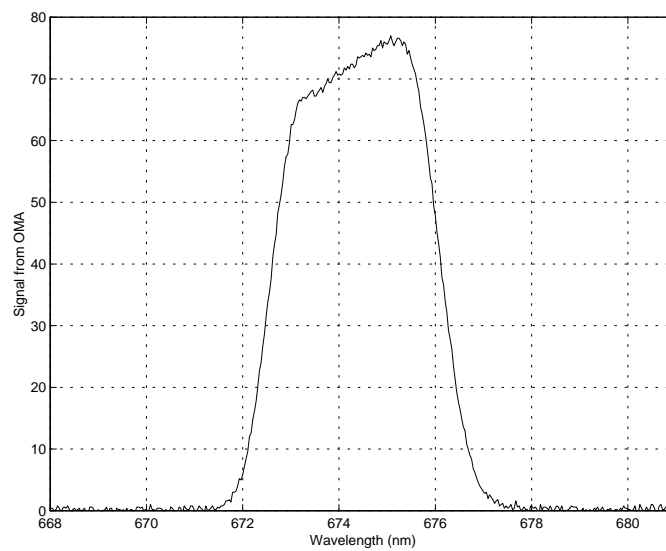
Figure 8.5: Spectrum of white light after passing through the monochromator as recorded by the OMA. The OMA signal is presumably in mV.

spectrum is shown in Figure 8.5. Two Al mirrors were then added to bypass the monochromator, as indicated in Figure 8.6, and a second spectrum recorded. This spectrum was found to be approximately flat. Dividing the first spectrum by the second spectrum and normalizing the result, gives the filter function of the monochromator, $F(\lambda)$, shown in Figure 8.7.

A horizontal line drawn across $F(\lambda)$ at approximately half its height allows the centre wavelength to be determined using $\lambda_c = (\lambda_1 + \lambda_2)/2$ (see Figure 8.7). The bandwidth of the monochromator (see Section 6.3) is obtained by integrating the curve. Note that since the curve vaguely resembles a top hat function, the bandwidth is approximately equal to the FWHM of the curve.

This entire procedure was then repeated for a number of settings of ha#1 (chosen arbitrarily). The results are summarized in Figures 8.8 and 8.9. The polynomial fits were used to calibrate the results of Raman scattering experiments.

From Figure 8.9, the random error in the bandwidth is estimated to be about 2%. As the measured bandwidths are of the order of a few nanometers, any correction due to the finite impulse response of the OMA (of order 0.2nm) is negligible. A more serious concern is that the spectrum of light may have been modified by the entrance slit of the OMA. In some experiments performed with the Stolen fibre (see Section. 10.2.1), the slit was found to reduce the bandwidth by about 11%. It is therefore possible that the bandwidths in Figure 8.9 are about 11% too small.

During the course of these experiments the signal recorded by the photodetector in Figure 8.3 was found to vary from a maximum of 40.1mV at 773nm to a minimum of 3.1mV at 575nm.

8.5 Alignment during experiments

During the Raman scattering experiments, the monochromator was first aligned using the preliminary calibration curves (see Section 8.4.2). The alignment was then optimized by coupling the white light source into the fibre and iteratively adjusted the horizontal adjusts of the mirrors at #2 and #3 until the count rate at the PM tube was maximized.

8.6 Test fibre polarization preservation

The white light source was also useful in testing how well the fibres preserved polarization. The white light source was coupled into the fibre and a sheet

of polaroid placed in front of the 20x objective (see Figure 7.1). The light leaving the PBS (see Figure 7.3) was shone directly into the eye and the polaroid sheet slowly rotated. If the light intensity was modulated (perhaps by a factor of ten; difficult to judge by eye), but the colour (spectrum) invariant, then this indicated that the fibre preserved polarization well across the visible spectrum. The FS-HB-3611 fibre passed this test, but other HiBi fibres failed, even though they appeared to preserve the polarization of a monochromatic beam.

8.7 Calibration of neutral density filters

The transmission of the Edmund neutral density filters was measured using a Shimadzu UV-3101PC spectrophotometer. The results are shown in Figure 8.10.

In analyzing the data in the experiments the transmissions were assumed to have the values 1.27%, 5.27% and 32.7%, independent of wavelength. For the Stokes data (650nm to 740nm) this introduces systematic errors of at most 1% (1% filter), 2.4% (5% filter) and 1.4% (32% filter).

8.8 Fibre mode field radius

The mode field radius (see Section 4.4) of the FS-HB-3611 fibre was determined by measuring the far field intensity distribution, as suggested by Figure 4.2. The cw pump laser on either 647.1nm or 676.5nm was used as the source. The intensity was measured using the 818-UV detector fitted with a 100μm diameter pinhole. The distance z between fibre and pinhole was typically of the order 20cm. The detector/pinhole was translated in the radial (r) direction in steps of about 4mm to build up the profile. The shape of the profile depended on whether the pump was aligned to the slow or fast axis and whether the detector was scanned in a direction parallel or perpendicular to the electric field vector of the light, **E**. Closest agreement with Gaussian behaviour was found when illuminating on the slow axis and scanning parallel to **E**, whilst poorest agreement occurred when illuminating on the fast axis and scanning parallel to **E** (see Figure 8.11).

Fitting Gaussians to the data gives the far field divergence angles listed in Table 8.5. The random error in these values is about 1%. Using Gaussian beam propagation (see Section 4.5), the corresponding mode field radii are as listed in Table 8.6.

The mode field radii of the Stolen fibre were measured in the same way. A

Illumination	Fast axis		Slow axis	
wavelength	$\parallel$ **E**	$\perp$ **E**	$\parallel$ **E**	$\perp$ **E**
647.1nm	0.07773	0.08178	0.08392	0.07987
676.5nm	0.07635	0.08070	0.08337	0.07976

Table 8.5: Far field divergence angles (in radians) for FS-HB-3611 fibre. $\parallel$ **E** denotes scanning the detector in a direction parallel to the electric field of the light. Similarly, $\perp$ **E** denotes scanning the detector in a direction perpendicular to the electric field of the light.

Illumination	Fast axis		Slow axis	
wavelength	$\parallel$ **E**	$\perp$ **E**	$\parallel$ **E**	$\perp$ **E**
647.1nm	2.650	2.519	2.455	2.579
676.5nm	2.820	2.668	2.583	2.700

Table 8.6: Mode field radii (in microns) for FS-HB-3611 fibre. $\parallel$ **E** denotes radius in a direction parallel to the electric field of the light. Similarly, $\perp$ **E** denotes radius in a direction perpendicular to the electric field of the light.

1m length of fibre was used. Better results might have been obtained with a longer length. The results are summarized in Table 8.7. Note that Stolen's comments about the error introduced into the effective area by using the Gaussian approximation (see Section 4.8) are based on experience with fibres of this type. The far field intensity distributions obtained with the Stolen fibre were less Gaussian than those shown in Figure 8.11. This suggests that Stolen's estimate of 10% to 15% for the error in the effective area is probably too large in the case of the FS-HB-3611 fibre. What is a little disturbing is that, even if the error in the effective area is as large as 15%, the error in the mode field radius would only be about 7%, but the measured mode field of the FS-HB-3611 at 647.1nm differs from the value quoted by the manufacturer on the fibre spool by about 30%. The value quoted by the manufacturer is presumably for 633nm and the mode field radius is expected to vary with wavelength (see Equation 4.4), but any wavelength dependence is insufficient to account for such a large discrepancy.

8.9 Measurement of pulse duration

This will be discussed in Section 10.2.2.

Illumination wavelength	Fast axis		Slow axis	
	$\parallel$ **E**	$\perp$ **E**	$\parallel$ **E**	$\perp$ **E**
647.1nm	2.167	2.276	2.125	2.101
676.5nm	-	-	-	2.333

Table 8.7: Mode field radii (in microns) for the Stolen fibre. $\parallel$ **E** denotes radius in a direction parallel to the electric field of the light. Similarly, $\perp$ **E** denotes radius in a direction perpendicular to the electric field of the light. The dashed values were not measured.
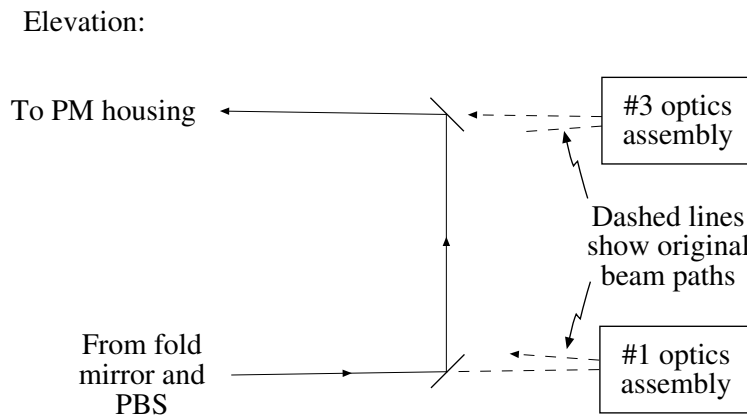
Figure 8.6: Elevation showing two aluminium mirrors added to bypass monochromator. Refer also to Figure 7.3.
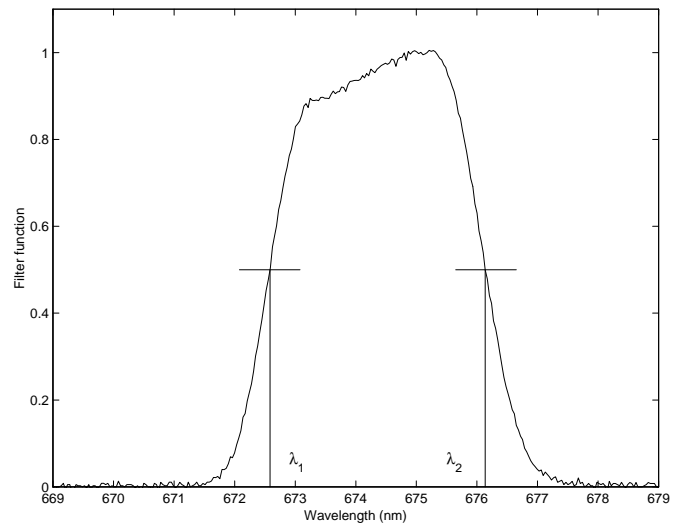
Figure 8.7: Filter function, $F(\lambda)$, of monochromator verses wavelength, λ, for ha#1=-0.22mm.
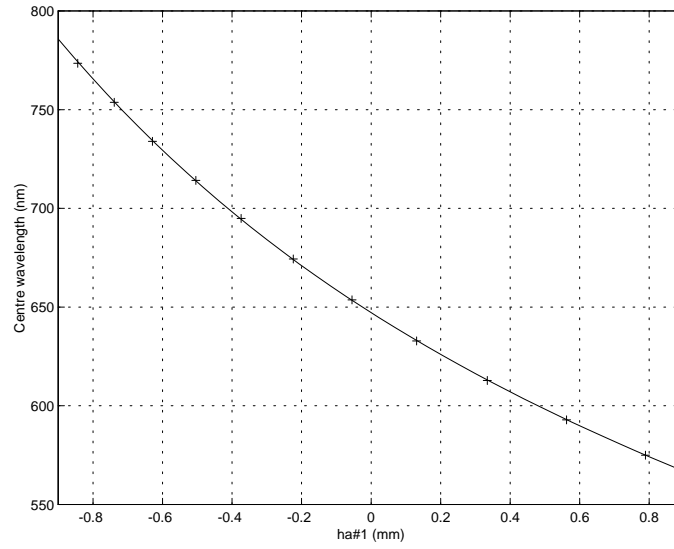
Figure 8.8: Relationship between centre wavelength, λ_c, and setting of horizontal adjust micrometer for mirror at #1, ha#1, for monochromator. The crosses are experimentally measured points. The curve is a fourth order polynomial fit through the points.
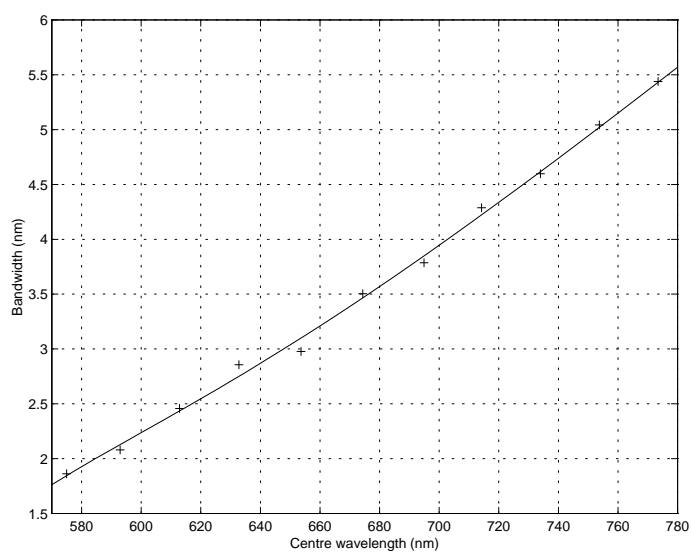
Figure 8.9: Bandwidth of monochromator verses centre wavelength of monochromator. The crosses are experimentally measured points. The curve is a fourth order polynomial fit through the points.
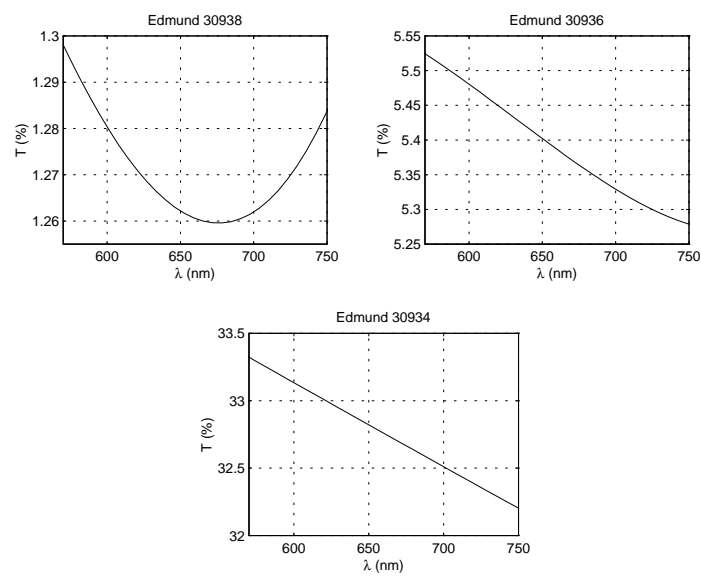
Figure 8.10: Measured transmission of Edmund neutral density filters.
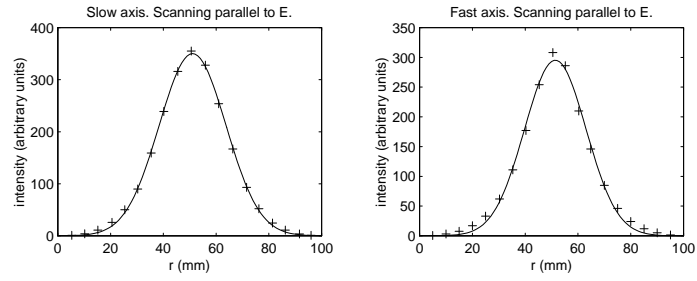
Figure 8.11: Far field transverse intensity profiles for FS-HB-3611 fibre. For the definition of r see Figure 4.2. The crosses are experimental measurements using 647.1nm illumination and a separation between end of fibre and pinhole on photodetector of 301mm. The curves are Gaussian fits to the measured points.

Chapter 9

Spontaneous scattering experiments

This chapter details the results of spontaneous scattering experiments (those experiments where the number of Raman scattered photons remains sufficiently small that stimulated scattering may be neglected; see Section 6.1). Unless explicitly stated otherwise, the experiments were performed with the FS-HB-3611 fibre (Section 7.4) and the cw pump laser (Section 7.1). All experiments undertaken in this thesis were conducted at room temperature. The uncertainties quoted are estimates of standard deviation.

9.1 Scattered power per unit angular frequency Γ verses pump power P_p

In a preliminary experiment, 6.95m of FS-HB-3611 was used as test fibre. The output of the fibre was oriented so that light from the fast axis (Section 7.4) entered the monochromator (Section 7.5). The transmission of the fibre and two microscope objectives, measured with a 647.1nm beam, was 60%. The monochromator was aligned to a centre wavelength of 624.15nm (Section 8.5). A cw 647.1nm beam was aligned to the slow axis of the fibre (orientation for perpendicular scattering; see Section 5.3). Figure 9.1 shows measurements of scattered power per unit angular frequency, $\Gamma_\perp$, at about 624.15nm (see Section 6.3) verses pump power, P_p (both quantities determined at the end of the fibre; see Section 8.1).

The data in Figure 9.1 is not a straight line as Equation 6.26 suggests it should be. The reason for the curvature is that there is fluorescence as well as Raman scattering. At low pump powers (less than about 1mW) fluorescence is the dominant source of photons at about 624nm. The lifetime of one of the
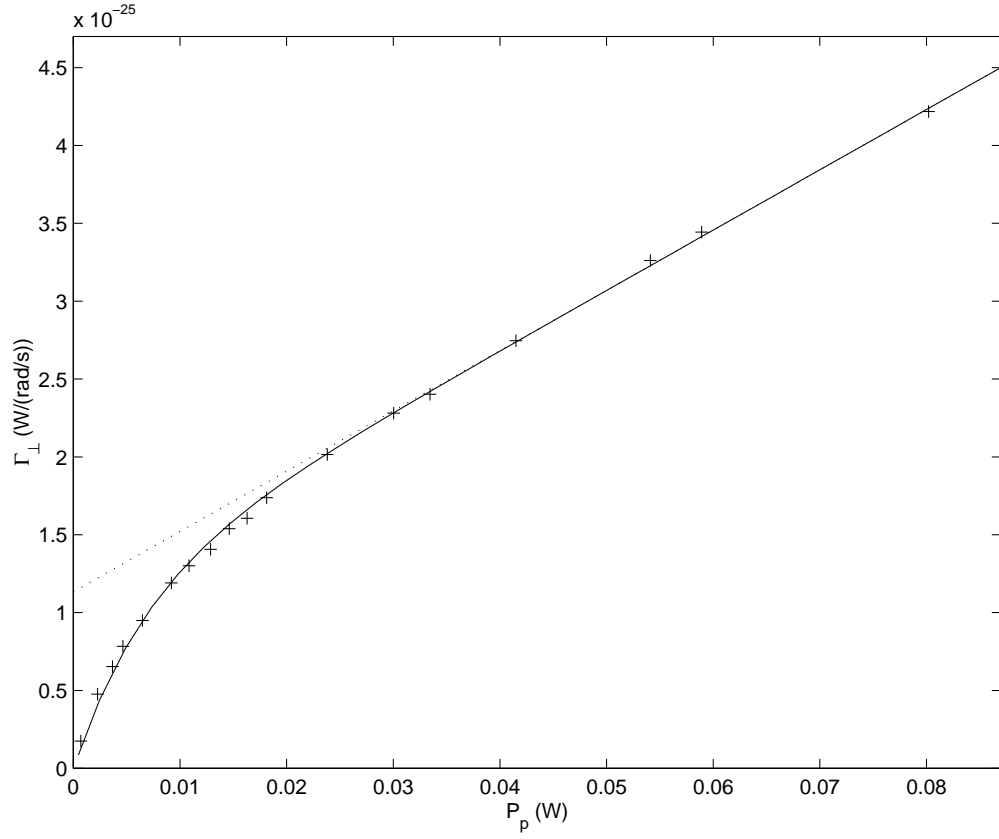
Figure 9.1: Power of perpendicularly scattered light per unit angular frequency at 624.15nm as a function of pump power at 647.1nm for 6.95m of FS-HB-3611 fibre. The crosses are experimental measurements. The dotted line is a straight line fit to the data for $P_p > 27$mW (note that two data points at 92mW and 105mW are not shown as they only confirmed the straight line behaviour in the high power limit). The solid line is Equation 9.1.

excited states associated with the fluorescence is long, so that, as the pump intensity is increased to about 10mW, the fluorescence saturates (all the electrons associated with the fluorescence are pumped into long lived excited states). Once the fluorescence is completely saturated (pump powers greater than about 40mW), the graph becomes linear, as expected for spontaneous Raman scattering. The dynamics is well modelled by the relation

$$\Gamma_\perp = 3.87 \times 10^{-24} P_p + 1.13 \times 10^{-25} \left(1 - e^{-147 P_p}\right). \tag{9.1}$$

The fluorescence will be further discussed in Section 9.12.

9.2 Spontaneous scattering coefficients $R_\parallel$ and $R_\perp$

Assuming the background term b_p (Section 6.6) is negligible (this will be discussed further in a moment), the gradient of the straight line fit to the data in Figure 9.1 can be used with Equation 6.27 to recover the spontaneous scattering coefficient (Section 5.3) $R_\perp$ (for scattering from 647.1nm to 624nm). Graphs similar to Figure 9.1 were plotted for both parallel and perpendicular scattering and for a wide range of wavelengths. Each graph had at least four data points spanning part of the linear region. From these graphs the gradients and intercepts were determined (the intercepts give some information about the fluorescence and will be discussed in Section 9.12). From the gradients, values for $R_\parallel$ and $R_\perp$ were calculated. The results are shown in Figure 9.2. Note that the wavelength separation between adjacent samples is about 3/4 the bandwidth for anti-Stokes wavelengths (left half of figure) and 1/2 the bandwidth for Stokes wavelengths (right half of figure).

In Figure 9.2 the data for wavelengths between 600nm and 684nm was obtained using the 6.95m length of fibre, oriented as described in Section 9.1. At the wavelengths nearest the pump, 641nm and 652.5nm, which correspond to values of Ω of -27.7×10^{12}rad/s and 24.1×10^{12}rad/s respectively, $R_\parallel$ seems to jump abruptly. It is known [38] that at room temperature, $R_\parallel$ in fused silica does have a peak at about $|\Omega| \simeq 11.3 \times 10^{12}$rad/s. This peak arises, not because of a peak in $M_\parallel(\Omega)$, but because the function $h(\Omega, T)$ increases as $|\Omega| \to 0$ (see Equations 5.11 and 5.3). However, this peak is too small to account for the observed jump and it is likely that, at these wavelengths, pump light is reaching the PM tube (also, there is no corresponding jump in $R_\perp$).

The data for wavelengths longer than 684nm was obtained using a 38.6m length of fibre, oriented with its slow axis aligned to the monochromator.

Figure 9.2: Parallel spontaneous scattering coefficient $R_\parallel$ (open circles) and perpendicular spontaneous scattering coefficient $R_\perp$ (dots) for the FS-HB-3611 fibre and a pump wavlength of 647.1nm (indicated by the vertical line near the centre of the graph).

The transmission of this fibre and the two microscope objectives, measured with a 647.1nm beam, was 45%. Some measurements were also made with this fibre for the case of parallel scattering at wavelengths near 666nm (which corresponds to maximum scattering). The measurements made with the two pieces of fibre in the vicinity of maximum scattering were found to be equal within experimental error, suggesting that the background term b_p is negligible at this wavelength. The approximate maximum value of $R_\parallel$ is

$$5 \times 10^{-22} \text{m}^{-1} \, (\text{rad/s})^{-1}$$

and this occurs at a wavelength of about

$$666\text{nm}$$

which corresponds to

$$\Omega = 83 \times 10^{12} \text{rad/s}.$$

The maximum scattering data will be discussed further in Section 9.8.

It is expected that the background term b_p will become more significant at wavelengths where the scattering is weak. With this in mind, $R_\parallel$ at 606nm was measured with the 38.6m length of fibre and compared to the result obtained with the 6.95m length of fibre. The value obtained with the shorter fibre was about 17% larger. This means that the value of $R_\parallel$ at 606nm in Figure 9.2, which was obtained with the 6.95m and is uncorrected for b_p, is too large by about 20%.

Measurements were also made with a third piece of fibre. This had length 5.30m and was oriented in the same way as the 38.6m piece of fibre. Values of $R_\parallel$ at wavelengths of 701nm and 722.5nm measured with the 5.30m were found to be smaller than those measured with the 38.6m fibre by about 20% and 13% respectively. This is rather alarming since the background term, b_p, should cause values for $R_\parallel$ measured in short fibres to appear larger than values measured in long fibres. One possible explanation is that the fibre loss has a stronger variation with wavelength than Rayleigh scattering (see Section 6.5, in particular, Equation 6.23) However, these errors are larger than would be expected if the loss is due to drawing induced defects (there is still the possibility of loss due to transition metal impurities). The errors suggest that the values of R shown in Figure 9.2 for wavelengths longer than about 700nm (which are values obtained with the 38.6m piece of fibre without any correction for b_p or fibre loss) may be too large by about 20%.

Values of $R_\parallel$ and $R_\perp$ for wavelengths shorter than 600nm were measured with both the 5.30m and 38.6m fibres. The values measured with the short piece of fibre were nearly four times as large as those measured with the long
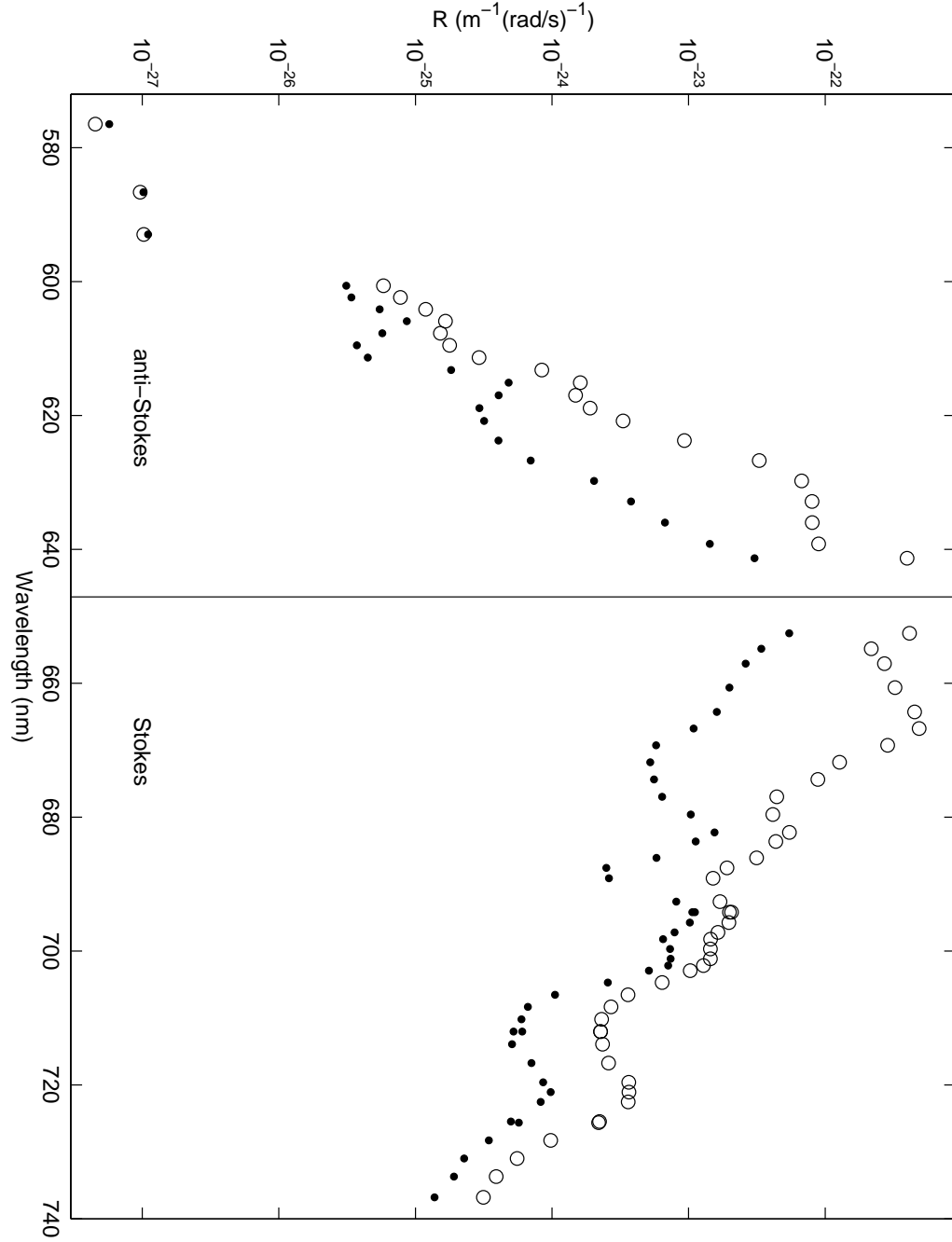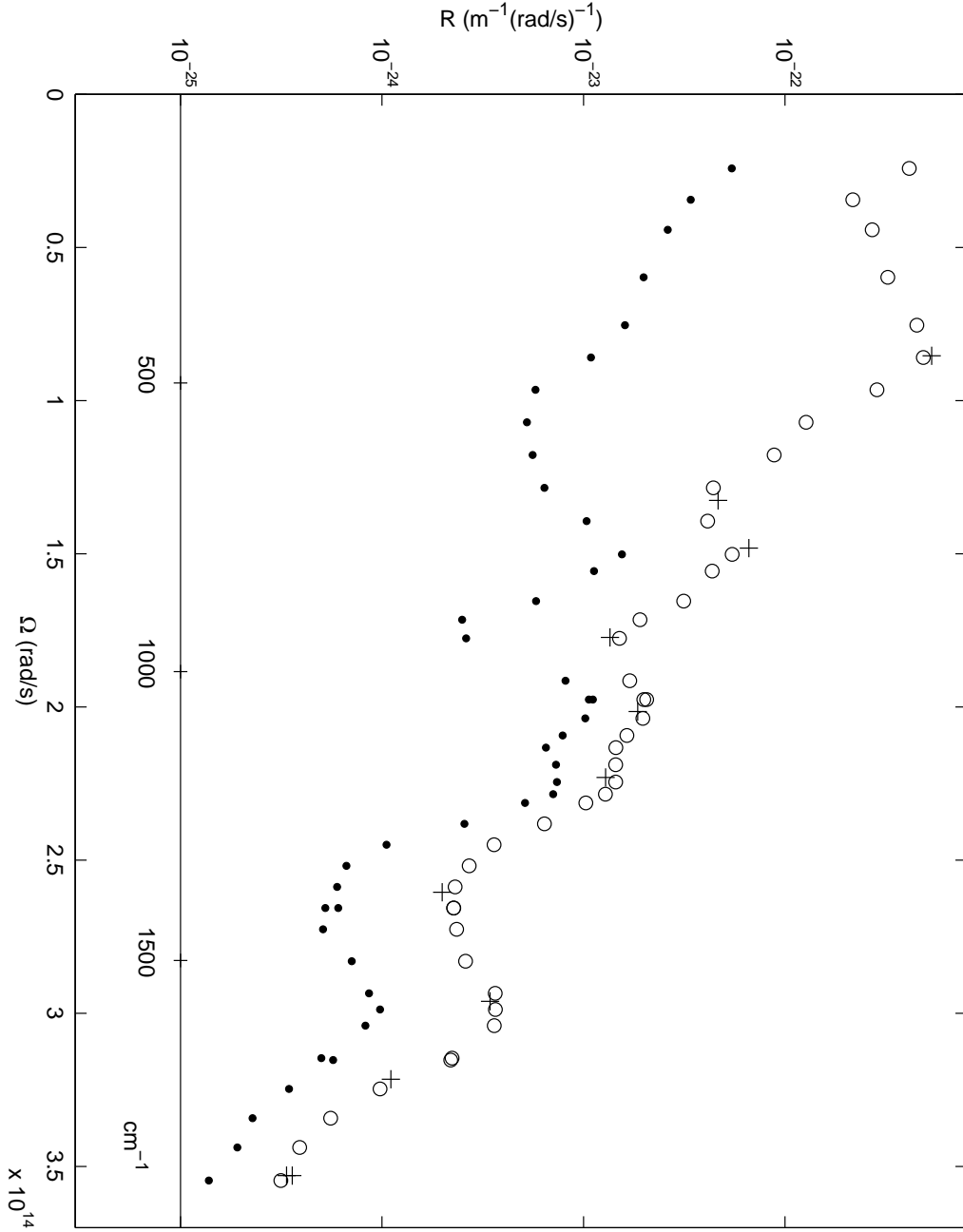
Figure 9.3: Parallel spontaneous scattering coefficient $R_\parallel$ (open circles) and perpendicular spontaneous scattering coefficient $R_\perp$ (dots) for the FS-HB-3611 fibre and a pump wavlength of 647.1nm. The crosses are predictions for $R_\parallel$ based on data obtained with a 676.5nm pump (see Section 9.3).

piece of fibre. This may be due to b_p or it might be due to fibre loss (if the loss mechanism has a much stronger wavelength dependence than Rayleigh scattering). For the purposes of Figure 9.2 it has been assumed that the discrepancy is due to b_p. The values shown in the figure have been obtained using data from both fibres and Equation 6.28. Note that $R_\perp > R_\parallel$, in violation of Equation 5.6 (the fibre preserved polarization across the visible spectrum; see Section 8.6) and that the values of R do not seem to be strong functions of wavelength as might be expected for Raman scattering. It is possible to envisage sources of background that are proportional to *both* the pump power and the length of the fibre (for example, a fraction of the pump light which Rayleigh scatters out of the fibre through the cladding), and it might well be that the data on Figure 9.2 for wavelengths less than 600nm should be interpreted as the noise floor of the method rather than values of R.

Figure 9.3 shows the Stokes data from Figure 9.2 plotted against Ω (see Equation 5.6).

In Raman spectroscopy it is common practice to express difference in frequency between pump and scattered light in terms of wavenumber, often denoted $\bar{\nu}$. The relation between Ω and $\bar{\nu}$ is

$$\bar{\nu} = \frac{\Omega}{2\pi c}. \tag{9.2}$$

$\bar{\nu}$ is usually quoted in units of cm^{-1}, in which case, c in Equation 9.2 should be the vacuum speed of light in cm/s. For convenience, a wavenumber scale has also been included in Figure 9.3.

9.3 Changing the pump wavelength

Changing pump frequency (wavelength) is a useful method of distinguishing Raman scattering from fluorescence. Both processes produce photons, shifted in frequency from the pump, with a characteristic frequency spectrum. In the case of fluorescence, the frequencies at which spectral peaks are observed, coincides with the frequencies of particle motion in the material. On the other hand, in Raman scattering, the frequencies of the spectral peaks are related to the frequency of the pump beam, as well as to the frequencies of particle motion. Only in the case of Raman scattering will a change in frequency of the pump produce an equal shift in position of all the spectral peaks.

For a given angular frequency separation Ω between pump and scattered light, the value of R obtained with a pump of angular frequency ω_p (which will

be denoted in this section R_p) can be related to the value of R obtained with a pump of angular frequency ω_q (which will be denoted in this section R_q) using Equation 5.11. If the effective refractive index is assumed independent of angular frequency (see Section 4.9.3), and if the fibre is assumed homogeneous (see Equation 6.20), and if the spot size is assumed inversely proportional to angular frequency (see Equation 4.4), then using Equations 5.11, 5.2 and 4.8, R_p and R_q are related by

$$R_p = \frac{\omega_p\left(\omega_p - \Omega\right)}{\omega_q\left(\omega_q - \Omega\right)} \frac{\left(\frac{1}{\omega_q}\right)^2 + \left(\frac{1}{\omega_q - \Omega}\right)^2}{\left(\frac{1}{\omega_p}\right)^2 + \left(\frac{1}{\omega_p - \Omega}\right)^2} R_q. \qquad (9.3)$$

Using the 38.6m piece of fibre, oriented as described in Section 9.2, values of R were measured for scattering from a 676.5nm wavelength pump to wavelengths between 697nm and 775nm. The results for parallel scattering have been used with Equation 9.3 to predict the values of $R_\parallel$ expected for a 647.1nm pump. The predictions have been included in Figure 9.3 as crosses. Note that there is excellent agreement between the predictions and the actual values obtained when pumping with 647.1nm. In the case of perpendicular scattering, the predictions were consistently too large. This is consistent with the fast axis of the fibre having significantly greater loss for a 676.5nm pump than a 647.1nm pump (see the comments about the loss of the fast axis in Section 7.4).

9.4   Assignment of peaks

Changing the pump wavelength confirms that the spectral peaks in Figure 9.3 are indeed due to Raman scattering. There has been considerable effort by previous authors to identify which vibrational motions of the nuclei in the glass have angular frequencies coincident with peaks in the spectra [11, p172]. The peaks at approximately 450cm^{-1}, 800cm^{-1}, 1050cm^{-1} and 1200cm^{-1} are all associated with the vibrational normal modes of SiO_4 tetrahedra, while the remaining peak at approximately 1600cm^{-1} is an overtone of the peak at 800cm^{-1} [49].

9.5   Ratio of parallel to perpendicular scattering

Except for the three data at wavelengths below 600nm, all the data in Figure 9.2 is observed to satisfy Equation 5.6. In the case of perpendicular

scattering, the pump power deflected by the PBS into the monochromator
(see Section 7.3) was about 1% to 2% of the power measured after the 10x
objective. In Figure 9.3, the perpendicular scattering shows a slight shoul-
der at $\Omega \simeq 85 \times 10^{12}$rad/s. At this angular frequency, the value of $R_\perp$ is
about 2% the value of $R_\parallel$. It is therefore likely that the shoulder is due to
the inability of the fibre to preserve the polarization of the much stronger,
parallel scattered light.

9.6 Anti-Stokes/Stokes ratio

Since the material Raman functions $M_\parallel\left(|\Omega|\right)$ and $M_\perp\left(|\Omega|\right)$ are even functions
of Ω, there is a relation between the anti-Stokes scattering at a given $|\Omega|$ and
the Stokes scattering at the same $|\Omega|$. Using the approximations mentioned,
and equations referenced, in Section 9.3, the relation between the value of
R for anti-Stokes scattering (which will be denoted in this section R_{aS}) and
the corresponding value for Stokes scattering (which will be denoted in this
section R_S) is

$$\frac{R_{aS}}{R_S} = \frac{\omega_p + |\Omega|}{\omega_p - |\Omega|}\, e^{-\frac{\hbar|\Omega|}{kT}}\, \frac{\left(\frac{1}{\omega_p}\right)^2 + \left(\frac{1}{\omega_p - |\Omega|}\right)^2}{\left(\frac{1}{\omega_p}\right)^2 + \left(\frac{1}{\omega_p + |\Omega|}\right)^2}. \tag{9.4}$$

Values for R_{aS} are available from Figure 9.2. Values for R_S at corresponding
values of $|\Omega|$ can be obtained from Figure 9.3 using linear interpolation. Fig-
ure 9.4 shows the resulting values for R_{aS}/R_S in the case of parallel scattering
(circles). Also included in the figure is the prediction of Equation 9.4.

Note that, although Equation 5.11 is not necessarily correct for overtones
and combination bands (see Section 5.6), Equation 9.4 *is* correct (from a
theoretical point of view, the potential errors in Equation 5.11 in the case of
overtones and combinations, affect both anti-Stokes and Stokes, cancelling
overall in Equation 9.4). The agreement between theory and experiment in
Figure 9.4 is excellent, except for the three points at large $|\Omega|$. These points
originate from the anti-Stokes measurements for wavelengths shorter than
600nm in Figure 9.2, which is further evidence that these points probably
provide more information about the noise floor of the method than they do
information about Raman scattering in the fibre.
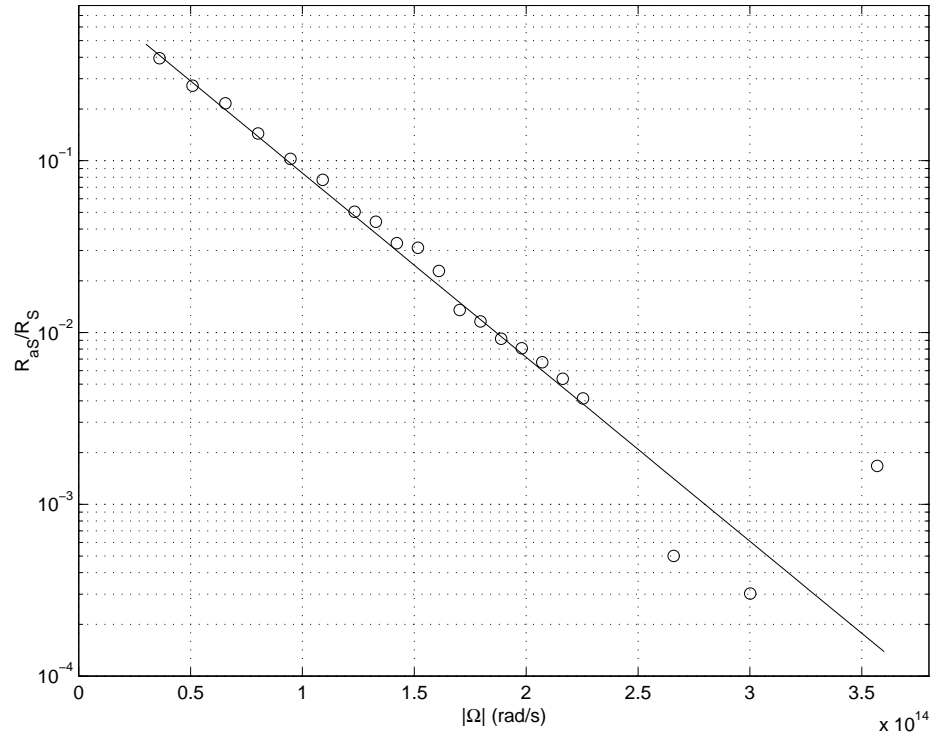
Figure 9.4: Ratio of anti-Stokes to Stokes scattering. The circles are experimental values (for parallel scattering) based on the anti-Stokes results in Figure 9.2 and the Stokes results in Figure 9.3. The solid line is the prediction of Equation 9.4.

9.7   The material Raman functions $M_\parallel$ and $M_\perp$

Using Equations 6.20 and 4.8, Equation 5.11 can be rewritten as

$$M_\parallel \left(|\Omega|\right) = 8\hbar\epsilon_0^2 c^2 \, \frac{n\left(\omega_p\right) n\left(\omega\right)}{\omega_p \, \omega} \, \frac{1}{h\left(\Omega, T\right)} \, \frac{\pi}{2} \sqrt{\hat{x}_p^2 + \hat{x}^2} \sqrt{\hat{y}_p^2 + \hat{y}^2} \, R_\parallel. \qquad (9.5)$$

Using Equation 4.4, $\hat{x}$ can be approximated by

$$\hat{x} = \hat{x}_p^* \, \frac{\omega_p}{\omega} \qquad (9.6)$$

where $\hat{x}_p^*$ is the mode field radius in the x direction for light with the pump angular frequency but the polarization of the scattered light (in the case of parallel scattering, this is the same as $\hat{x}_p$, but, in the case of perpendicular scattering, there is a distinction). A similar equation holds for $\hat{y}$.

Figure 9.5 shows values for $M_\parallel$ and $M_\perp$ obtained from the data in Figure 9.3 using Equations 9.5 and 9.6, refractive indices from Section 4.9.1, and the measured mode fields of the FS-HB-3611 fibre at 647.1nm (see Section 8.8). Note that, although the results shown in Figure 9.5 have been obtained from measurements made at room temperature with the FS-HB-3611 fibre and a 647.1nm wavelength, the material Raman functions should depend only on the nature of the glass (see Section 5.1). In addition, the Raman gain coefficients $g_\parallel$ and $g_\perp$, are more closely related to the material Raman functions than to the values of $R_\parallel$ and $R_\perp$ since $h\left(\Omega, T\right)$ does not appear in Equation 5.12.

9.8   The maximum value of $M_\parallel$

As discussed briefly in Section 9.2, measurements of parallel scattering from 647.1nm to wavelengths in the vicinity of 666nm (maximum scattering) were made with both 6.95m and 38.6m fibre lengths. The values of $M_\parallel$ recovered from the measurements are shown in Figure 9.6. These values have been obtained using Equation 9.5 and linear interpolation between the measured mode fields at 647.1nm and 676.5nm (see Section 8.8) to estimate the mode field at the wavelength of the scattered light.

Figure 9.6 shows good agreement between the data obtained with the two fibre lengths. This suggests that for scattering to ~ 660nm with these fibre lengths, the background term b_p is negligible and any wavelength dependence of the fibre loss is insignificant. From Figure 9.6, $M_\parallel$ is observed to have its maximum at

$$\Omega = (84 \pm 3) \times 10^{12} \text{rad/s}$$
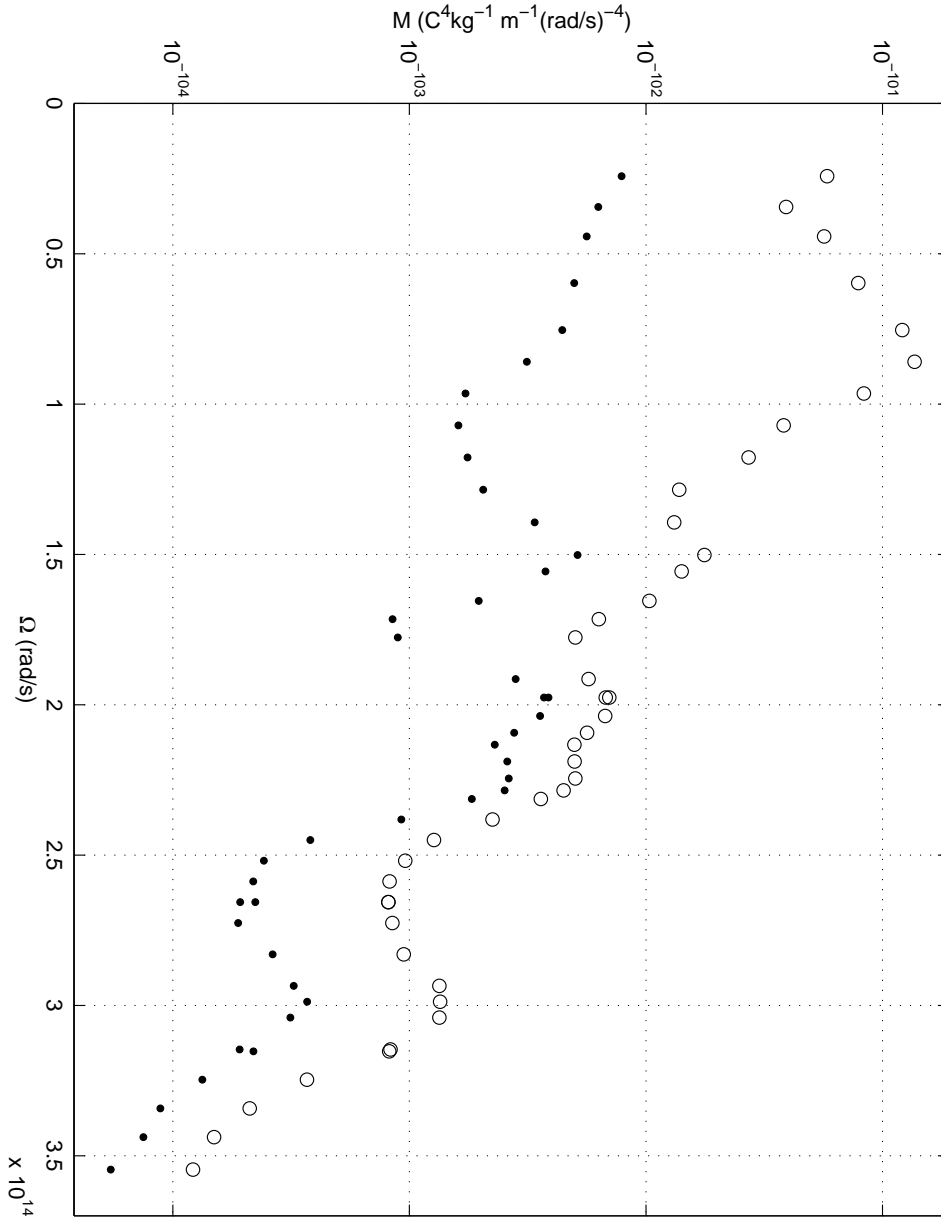
Figure 9.5: Measured values for the material Raman functions $M_\parallel(\Omega)$ (open circles) and $M_\perp(\Omega)$ (dots), deduced from the Stokes scattering data in Figure 9.3.
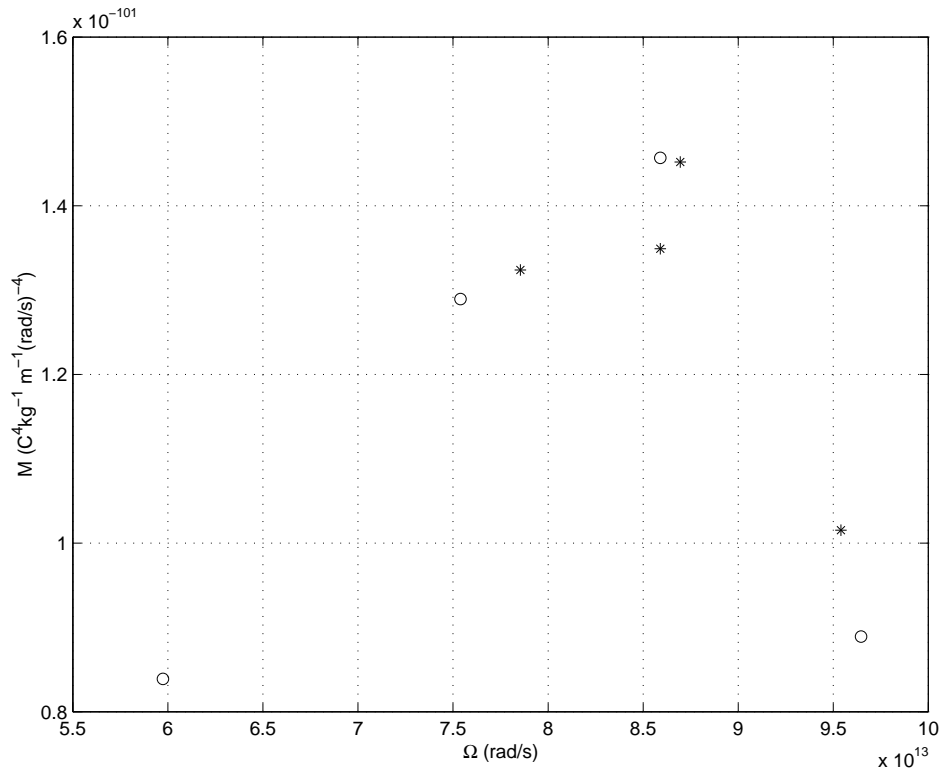
Figure 9.6: Detail from Figure 9.5 in the vicinity of maximum scattering. The circles are the values of $M_\parallel$ obtained with the 6.95m length of fibre. The asterisks are additional values for $M_\parallel$, not shown in Figure 9.5, which were obtained with a 38.6m length of fibre.

which corresponds to 13.4 ± 0.5THz or

$$\bar{\nu} = 445 \pm 16 \text{cm}^{-1}.$$

The uncertainty here is just an estimate of the uncertainty involved in locating the maximum on the graph.   The maximum value for $M_\parallel$ is

$$1.43 \times 10^{-101} \text{C}^4\text{kg}^{-1}\text{m}^{-1}\,(\text{rad/s})^{-4} \pm 4\%$$

The uncertainty here is given by

$$4\% = \sqrt{1\%^2 + 2\%^2 + 2\%^2 + 3\%^2}. \qquad (9.7)$$

On the right hand side of Equation 9.7 is a 1% random error from the transmission of the 883-UV filter (see Section 8.3.2), a 2% random error from the collection efficiency of the monochromator and PM tube (see Section 8.4.1), another 2% random error from the bandwidth of the monochromator (see Section 8.4.3), and a 3% uncertainty which is an estimate of the uncertainty in locating the maximum in Figure 9.6.   Note that, if the calibration error in the responsivity of the 818-UV photodiode (see Section 8.3.3) is assumed the same at 647.1nm and ~ 666nm (a reasonable assumption), then the error enters twice in the determination of M (once in measurement of the pump power and once in calibrating the collection efficiency), cancelling out overall.

Equation 9.7 does not include the systematic errors.   These arise from

- calibration of the Edmund neutral density filters (see Section 8.7); known to be negligible.

- the assumption that the loss of the fibre at ~ 666nm equals the loss at 647.1nm (see Section 6.5).

- the slit on the OMA may have introduced an error into the calibration of the monochromator bandwidth (see Section 8.4.3).   This systematic error would result in the values of M being overestimated by possibly as much as 11%.

- using the Gaussian approximation to determine the effective area, A_{eff}, may result in values for M being overestimated by as much as $10 - 15\%$ (see Section 4.8), although it is hoped that the error is not that large in the case of the FS-HB-3611 fibre (see Section 8.8).

Note that the uncertainty quoted in Equation 9.7 is appropriate for Stokes scattering and $\Omega \simeq 80$rad/s.   For other values of Ω, especially values greater

than about 220×10^{12}rad/s (which corresponds to scattering from 647.1nm to wavelengths greater than 700nm), the uncertainty in the values of M in Figure 9.5 is larger than 4%. This is because, at the longer wavelengths, there is greater uncertainty in the calibration of the collection efficiency of the monochromator/PM tube (see Section 8.4.1), the calibration of the mode field radii (see Section 8.8) and the effects of fibre loss (see Section 6.5).

9.9 Comparison with measurements made in other fibres

The spontaneous scattering was also measured using the Stolen fibre (see Section 7.4). The resulting spectrum had the same spectral peaks as shown in Figure 9.2. Since the apparatus was not calibrated using the Stolen fibre, the full spectrum is not reproduced here. Using 2.85m of the Stolen fibre the value of $R_{\parallel}$ for $\Omega = 82.7 \times 10^{12}$rad/s was found to be $R_{\parallel} = 6.52 \times 10^{-22}$m^{-1}(rad/s)$^{-1} \pm 1.5\%$ (see Section 10.3.1). Using Equations 9.5 and 9.6, refractive indices from Section 4.9.1, and the measured mode fields of the Stolen fibre at 647.1nm (see Section 8.8), this corresponds to

$$M_{\parallel} = 1.41 \times 10^{-101}\text{C}^4\text{kg}^{-1}\text{m}^{-1}\,(\text{rad/s})^{-4}$$

Since $\Omega = 82.7 \times 10^{12}$rad/s corresponds approximately to maximum scattering, this should agree with the value in Section 9.8 (assuming the fibres have the same glass composition). The difference is less than 2% and consistent with the estimated random error. Of course, this good agreement should be treated with some caution, since any systematic errors will be common to both values, cancelling overall.

9.10 Time response

Theory predicts that a spontaneous Raman scattering experiment, performed with a pump laser which produces 60ps pulses, should give identical results to an experiment performed with a cw pump laser, provided only time averages are measured (see Section 6.1). This was tested experimentally using the two pump lasers available (see Section 7.1) and the Stolen fibre (see Section 7.4). Note that the Stolen fibre was selected for these experiments since it produces no observable fluorescence or SHG (see Sections 9.12 and 3.4.1). Results for parallel scattering from 647.1nm to wavelengths of 629.3nm, 635.8nm, 658.9nm, 666nm and 686.1nm will be presented in Chapter 10, but measurements were also made for parallel scattering from 647.1nm to 694.3nm

and 720.9nm, and parallel and perpendicular scattering from 647.1nm to 681.6nm, 687.8nm and 700.9nm. In all cases, results obtained with pulsed and cw lasers were found to agree within experimental uncertainty. Note that this only applies in the low power limit, where stimulated scattering can be neglected.

9.11 Comparison with measurements made by other authors

In discussing the results of a Raman scattering experiment, it would seem sensible to quote values for the material Raman functions, $M_\parallel$ and $M_\perp$, since these depend (to good approximation) only on the material. Despite this, many authors quote their results in terms of the bulk glass gain coefficients, $\hat{g}_\parallel$ and $\hat{g}_\perp$, which have the disadvantage that they are functions both of the material and the pump wavelength. Values for bulk glass gain coefficients can be quoted irrespective of what has actually been measured (spontaneous scattering in bulk glass, stimulated gain in fibres, etc) since the equations in Chapter 5 allow the various measurable quantities to be related to one another.

9.11.1 Spontaneous scattering in bulk glass

Stolen and Ippen [83] have measured spectra for $\hat{R}_\parallel$ (see Section 5.1) in fused quartz using a 514.5nm wavelength pump. They express their results in terms of the predicted Raman gain coefficient $\hat{g}_\parallel$ (see Section 5.2) for a 526nm wavelength pump. Their maximum value for $\hat{g}_\parallel$ is

$$1.88 \times 10^{-13}\mathrm{m/W} \pm 10\%$$

Using refractive indices from Section 4.9.1, and Equation 5.9, the corresponding maximum value for $M_\parallel$ is

$$1.15 \times 10^{-101}\mathrm{C^4 kg^{-1} m^{-1}\,(rad/s)^{-4}} \pm 10\%$$

Hellwarth et al. [42] have measured spectra for $\hat{R}_\parallel$ and $\hat{R}_\perp$ in fused quartz using a 514.5nm wavelength pump. Their maximum value of $\hat{R}_\parallel$ is

$$2.24 \times 10^{-10}\mathrm{cm^{-1}Sr^{-1}\left(cm^{-1}\right)^{-1}} \pm 10\%$$

where they are measuring the distance dz and frequency interval $d\omega$ (see Equation 5.1) in centimetres and wavenumber.(see Equation 9.2) respectively.

This is equivalent to

$$1.19 \times 10^{-19} \text{m}^{-1} \text{Sr}^{-1} \, (\text{rad/s})^{-1} \pm 10\%$$

where dz is now in metres and $d\omega$ in rad/s. Using refractive indices from Section 4.9.1, and Equation 5.4, the corresponding value for $M_\parallel$ is

$$1.33 \times 10^{-101} \text{C}^4 \text{kg}^{-1} \text{m}^{-1} \, (\text{rad/s})^{-4} \pm 10\%$$

9.11.2 Stimulated scattering in single mode fibres

Stolen and Ippen [83] also used a pump/signal type experiment to measure the stimulated gain coefficient $g_\parallel$ (see Section 5.3) in a single mode fibre at a frequency shift of 330cm^{-1}. The result agreed well with their spontaneous scattering measurement in bulk glass (see Section 9.11.1). A pump/signal experiment has also been performed by Mochizuki et al. [61] using a pump wavelength of 1.51μm and a signal wavelength of 1.62μm and 53km of standard (not polarization preserving fibre). They have expressed their result in terms of the bulk glass gain as $\hat{g}_\parallel = 4.8 \times 10^{-14}$m/W (note that they have used the results of Section 5.4 and the assumption that $\hat{g}_\perp \ll \hat{g}_\parallel$). Using Equation 5.9, this gives a value for $M_\parallel$ about 3/4 of Stolen's value. Dougherty et al. [29] have also conducted a pump/signal experiment. They used a pump wavelength of 795.5nm and a 700m length of polarization maintaining fibre. They quote the result of their measurement as $\hat{g}_\parallel = (1.2 \pm 0.1) \times 10^{-13}$m/W, which gives a value for $M_\parallel$ about 3% smaller than Stolen's value.

Mahgerefteh et al. [55] have used the dependence of Raman power on pump pulse duration to determine the stimulated gain in a single mode fibre. The fibre they used was 10.1km of ordinary (not polarization preserving) fibre, so they have used the results of Section 5.4 and the assumption that $\hat{g}_\perp \ll \hat{g}_\parallel$ to interpret their measurements. They obtain a value for $M_\parallel$ which is 0.95 of Stolen's value.

9.11.3 Stimulated scattering in multimode fibres

Rothschild and Abad [72] have used the nonlinear dependence of Raman power on pump power to measured the bulk glass gain in a 49m length of multimode fibre using a pump wavelength of 337.1nm. Their result is $\hat{g}_\parallel = 2.9 \times 10^{-13}m/W\pm 10\%$ (note that some depolarization would be expected in the multimode fibre, but this is not discussed). Using Equation 5.9, this gives a value for $M_\parallel$ within 1% of Stolen's value. A similar experiment has been performed by Pini et al. [69]. Using a pump wavelength of 308nm and a 15m length of fibre they obtain $\hat{g} = 1.6 \times 10^{-13}$m/W. Assuming this is

$\left(\hat{g}_\parallel + \hat{g}_\perp\right)/2$ (see Section 5.4) and that $\hat{g}_\perp \ll \hat{g}_\parallel$ at the peak of the gain (see Figure 9.3), then, using Equation 5.9, this gives a value for $M_\parallel$ about 2% larger than Stolen's value.   Mizunami et al. [59], in a similar experiment, obtain a value smaller than that observed by Pini et al. by a factor of 0.63.

9.12   Fluorescence

In Raman scattering experiments in silica optical fibres, Walrafen and Stone [99] observed a broad fluorescence, centred at about 635nm, when pumping with either the 488nm or 514nm lines of an argon ion laser.   In Raman scattering experiments in bulk samples of fused silica, Hellwarth et al. [42] observed no fluorescence pumping with 514nm (they may not have looked at long enough wavelengths), but did observe fluorescence pumping with the 647nm krypton line.   More recently, Canning and Sceats [19] have made measurements on the fluorescence from bulk samples of silica doped with germania using 647nm illumination.   In particular, they have investigated the changes in the fluorescence which occur after exposure to ultraviolet light.

The intercept of the best fit line in Figure 9.1 with the vertical axis, divided by the length of the fibre, gives the optical power per unit angular frequency per unit fibre length produced by the fluorescence when it is driven into saturation.   Such intercepts were available for a range of wavelengths as a by-product of data collection for the spontaneous Raman scattering experiments (see Section 9.2). A subset of the saturation fluorescence data available is plotted in Figure 9.7. All the data in this figure was collected using the fibre and pump polarization described in Section 9.1, so this is 'perpendicular' fluorescence, and, of course, the pump wavelength used was 647.1nm.

The fluorescence is particularly clear in Figure 9.1 since the perpendicular Raman scattering is weak at this wavelength (see Figure 9.2). At other wavelengths the Raman scattering dominated and it was difficult to measure the fluorescence with any precision. In particular, the oscillations seen at Stokes wavelengths in Figure 9.7 could be an artifact of measurement uncertainty. Also measurement of the 'parallel fluorescence' (pump polarized for parallel scattering) was even more difficult. However, for many wavelengths it was found that the parallel fluorescence was comparable in strength to the perpendicular fluorescence or up to a factor of two stronger.

The strength of the fluorescence in the 38.6m piece of fibre was stronger than that in the 6.95m piece, but only by a factor of two to four, suggesting that the fluorescence might originate from imperfections which are not uniformly distributed along the fibre length.
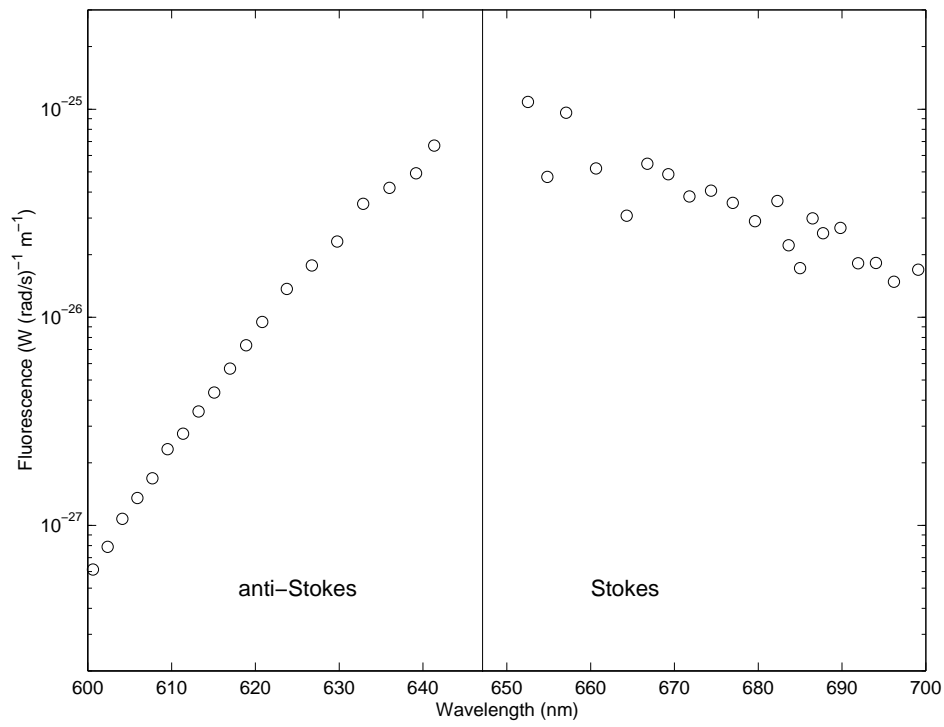
Figure 9.7: Saturation fluorescence power per unit angular frequency per unit fibre length. The vertical line indicates the pump wavelength (647.1nm).

Qualitatively similar fluorescence was observed in other fibres (a 3M low birefringence fibre for the HeNe wavelength type FS-SN-3224, a York bow-tie structure high birefringence fibre purchased through Newport type HB600 and an Andrew elliptical core fibre type 48280-633S-1) but was not observed in the Stolen fibre. Removal of the plastic jacket from the fibre did not change the strength of the fluorescence.

Fluorescence was not observed in the measurements made with a 676.4nm pump wavelength (see Section 9.3). However, this may have been because measurements were confined to Stokes wavelengths, and mainly for parallel scattering, conditions under which the Raman scattering might well be dominant.

Some indication of the lifetime of the fluorescence could be obtained using the pulsed pump. The cavity dumper driver was used to trigger a 1GHz analogue oscilloscope in synchronization with the repetition rate of the laser (which was set to 143kHz, corresponding to a time separation between pulses of 7μs). The signal from the PM tube was observed on the oscilloscope. At high pump powers (where the Raman scattering is dominant; see Figure 9.1) the signal from the PM tube was observed to be pulses 7μs apart, indicating that the detected photons were being produced in synchronization with the laser pulses (expected for Raman scattering). At low pump powers (where the fluorescence is dominant) the signal from the PM tube consisted of pulses distributed randomly in time. This suggests that the lifetime of the fluorescence is at least of order 7μs.

Chapter 10

Stimulated scattering experiments

This chapter describes the results of stimulated scattering experiments (those experiments where the number of scattered photons becomes large enough for stimulated scattering to become significant; see Section 6.2). Section 10.1 builds on Chapter 7, describing some specific features of the apparatus used in the stimulated scattering experiments. In a similar fashion, Section 10.2 builds on Chapter 8, describing some specific aspects of calibration. The experimental results are presented in Section 10.3. Some discrepancy between theoretical predictions and experimental results is observed in the limits of high pump powers. Possible origins for this discrepancy are further discussed in Section 10.4. This section also includes some comments about relating theory to experiment, and, as such, could have been included in Chapter 6. Hopefully, deferring the comments to this later stage will make them easier to follow.

10.1 Apparatus

The only pump wavelength used in the stimulated scattering experiments was 647.1nm (see Section 7.1). In all experiments, the pulsed laser was operated on divide by 32, giving a pulse repetition frequency of 37.644/32MHz and hence

$$T_R = 850\text{ns}. \tag{10.1}$$

The only fibre used was a 2.85m length of the Stolen fibre (see Section 7.4) Note that the Stolen fibre was selected for these experiments since it produces no observable fluorescence or SHG (see Sections 9.12 and 3.4.1). The output end of the fibre was oriented so that light from the fast axis was deflected

by the PBS into the monochromator (see Figure 7.3). In all experiments the pump beam (either pulsed or cw) was aligned to the fast axis (parallel scattering). The transmission of the fibre and two microscope objectives was about 58% (measured with the cw laser). Only about 2% of the pump power after the 10x, passed undeflected through the PBS.

10.2 Calibration

10.2.1 Monochromator bandwidth

The calibration data in Chapter 8 was obtained using the FS-HB-3611 fibre. Much of the calibration is independent of fibre, the one exception being calibration of the monochromator, since the spot size of the beam in the monochromator depends on the mode field radii of the fibre. It would seem sensible to assume the collection efficiency is approximately independent of spot size, so, in this chapter, the calibration from Section 8.4.1 will be assumed to hold.

For this chapter, the bandwidth of the monochromator was recalibrated using the Stolen fibre. The bandwidth was measured as described in Section 8.4.3, except that the 45^0 mirror positioned after the PM housing in Figure 8.4, was positioned in front of the PM housing. This arrangement has the drawback that any influence of the PM housing optics on the bandwidth is excluded, introducing a potential systematic error.

At wavelengths of 647nm and 666nm the measured bandwidths were 3.18nm and 3.60nm respectively. These are 6.5% and 8.4% (respectively) larger than the values predicted by the calibration curve in Figure 8.9. As a consequence, the bandwidths in this chapter have been obtained by increasing the values in the calibration curve by 7.5%.

While making these measurements it was observed that the slit on the OMA was reducing the bandwidth by about 11%. This has been taken into account in this chapter. It is possible that the bandwidths in Section 8.4.3 may have been underestimated by a similar amount.

10.2.2 Pulse duration

The duration of the pulses from the pulsed pump was calibrated using the 25GHz photodiode and 34GHz digital oscilloscope (see Section 7.1). The pulses were delivered to the photodiode using 1.2m of fibre (FCH-1C-SMF-0.83). The trigger was derived from one pulse incident on the photodiode and the signal from the following pulse. This arrangement is known to

have an impulse response of 20ps (FWHM) [63], with the rise time being considerably shorter than the fall time.
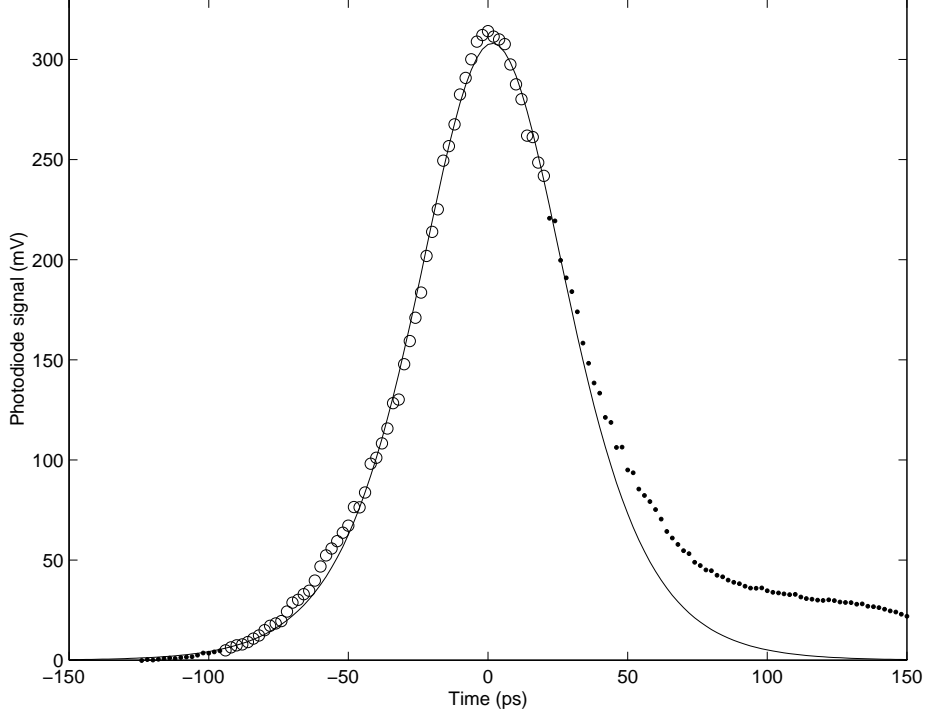
Figure 10.1: Typical pump laser pulse as recorded by the 25GHz photodiode and 34GHz oscilloscope. The dots and circles are the data points recorded by the oscilloscope. In this case, the data has been averaged four times. The line is a $sech^2$ fit to the circles.

Figure 10.1 shows a typical pulse profile. This particular profile was recorded after the pulse had propagated through the test fibre, and the average power leaving the fibre was about 30mW, but the actual profile was found to be insensitive to the average power propagating in the fibre. The rise of the pulse has been fitted with a $sech^2$ (the pulses are known to have an approximately $sech^2$ shape [63]). The fitted $sech^2$ has a duration of 63.4ps (FWHM). A more appropriate value, taking into account the impulse response of the photodiode, is given by

$$T_F = \sqrt{(63.4\text{ps})^2 - (20\text{ps})^2} = 60.2\text{ps}. \tag{10.2}$$

Note that the exact pulse duration depends on the alignment of the laser, which can vary from day to day. In an attempt to eliminate the fluctuations,

the alignment of the laser was adjusted so that an average pump power of 35mW leaving the fibre produced an average SRS power leaving the fibre (measured with the 818-UV; see Section 8.3.3) of 40μW. In practice, the SRS power could not be maintained at precisely this value and fluctuated between a maximum and a minimum which differed by a factor of about three. The reproducibility of the measurements will be illustrated further in Figure 10.2.

10.3   Results

10.3.1   Scattered power per unit angular frequency verses pump power

Figure 10.2 shows measurements of the time averaged scattered power per unit angular frequency, $\langle\Gamma_\parallel\rangle_t$, verses time averaged pump power, $\langle P_p\rangle_t$, for the case of parallel scattering from 647.1nm to 666nm ($\Omega = 82.7\times 10^{12}$rad/s) (see Section 9.1). The output coupling losses have been taken into account so that the measurements are estimates of $\langle\Gamma_\parallel\rangle_t$ and $\langle P_p\rangle_t$ inside the end of the fibre (see Section 8.1).

The data obtained with the cw pump is observed to be a straight line. Using Equation 6.2 and the gradient of the line gives

$$R_\parallel = 6.52 \times 10^{-22}\mathrm{m}^{-1}(\mathrm{rad/s})^{-1} \pm 1.5\%.$$

The uncertainty quoted here is just the random error based on the reproducibility of the experiment (the experiment was repeated on three different days). Once $R_\parallel$ is known, $g_\parallel$ can be calculated using

$$g_\parallel = \frac{\Omega}{|\Omega|}\,\frac{2\pi}{\hbar\omega_p}\,\frac{1}{h\left(\Omega, T\right)}\,R_\parallel \qquad (10.3)$$

which follows from Equations 5.11 and 5.12.   If the pulse duration and repetition rate of the pulsed laser are known, a prediction for $\langle\Gamma_\parallel\rangle_t$ in the case of pulsed pumping can then be obtained using Equations 6.15 and 6.16. This has been done, and the resulting curve is included in Figure 10.2. Note that the predictions can be obtained without any knowledge of the refractive indices, and, more importantly, of the integral

$$\int_{-\infty}^{\infty} dx \int_{-\infty}^{\infty} dy\, M_\parallel\left(|\Omega|\right) |f_p|^2\, |f|^2\,, \qquad (10.4)$$

which is observed to introduce considerable uncertainty when attempting to relate spontaneous scattering in fibres to spontaneous scattering in bulk
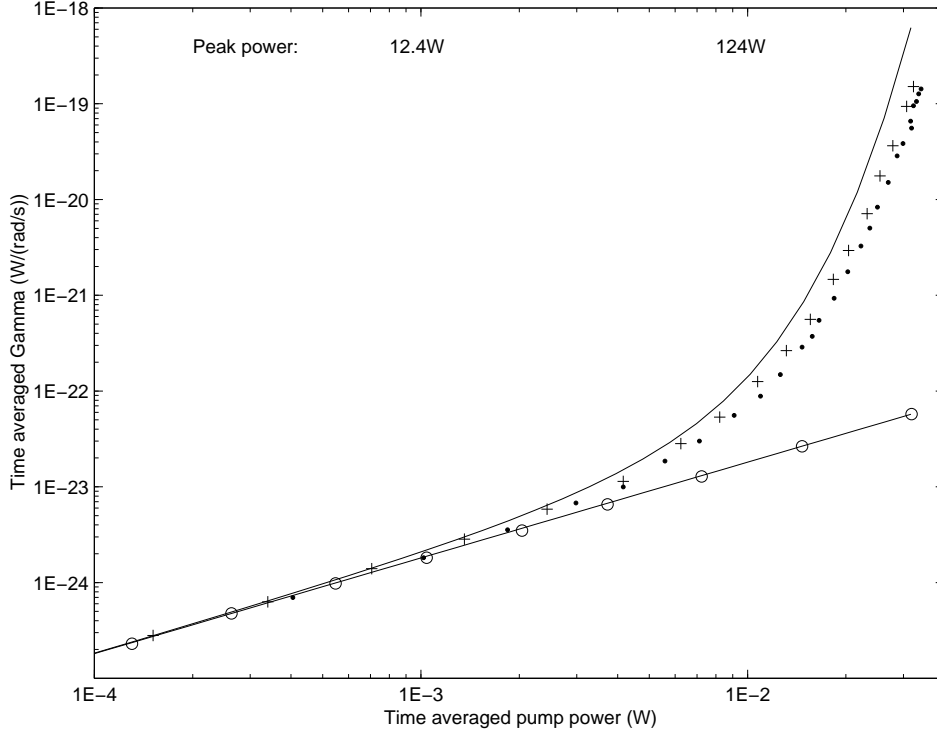
Figure 10.2: Time averaged scattered power per unit angular frequency $\left\langle \Gamma_\parallel \right\rangle_t$ verses time averaged pump power $\left\langle P_p \right\rangle_t$. This is for the case of parallel scattering to the peak of the gain (647.1nm to 666nm). The circles were obtained with the cw pump laser and the crosses with the pulsed pump laser. The straight line is a fit to the cw data. The curve is a prediction for the pulsed data using Equation 6.15. Measurements were made down to $\left\langle P_p \right\rangle_t \simeq 30\mu\text{W}$. These measurements are not shown as they only confirmed the straight line behaviour in the low power limit. The dots are the same as the crosses, except that the measurements were made on a different day (giving some idea of the reproducibility of measurements made with the pulsed laser). Using Equations 6.16, 10.1 and 10.2, the peak power of the pulses exceeds their average power by a factor of 12.4×10^3, and this is also indicated on the graph.

glass (see Chapter 9). Despite this, there is obviously some disagreement between theory and experiment. In the high power limit, theory is larger than experiment by a factor of about six. Similar results were obtained for parallel scattering from 647.1nm to 658.9nm; in the high power limit, theory was greater than experiment by a factor of about twelve. Possible reasons for the disagreement will be discussed further in Sections 10.3.2 and 10.4.
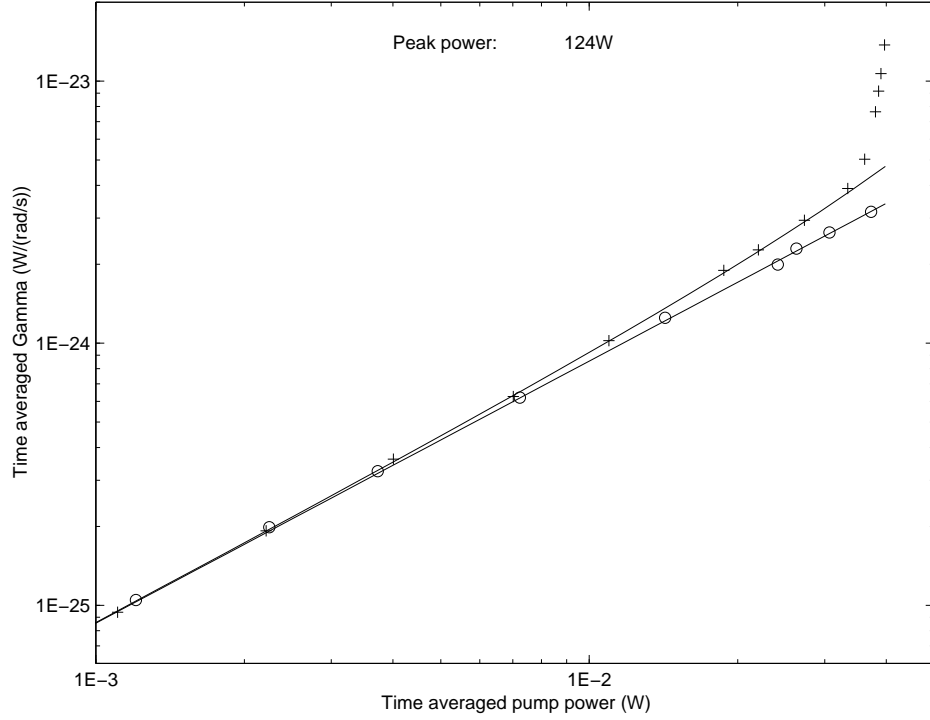
Figure 10.3: Same as Figure 10.2 but for the case of parallel scattering from 647.1nm to 686.1nm. Once again some measurements at low power, which have been included in fitting the straight line, are not shown on the graph.

Figure 10.3 shows the results of a similar investigation for parallel scattering from 647.1nm to 686.1nm ($\Omega = 166$rad/s). Once again there is divergence between theory and experiment, but, in this case, the nature of the divergence is quite different. At high powers the scattering is observed to increase abruptly and dramatically. One plausible explanation is stimulated scattering from the Stokes beam at 666nm to 686nm (this corresponds to $\Omega = 83$rad/s i.e. the peak of the gain). This possibility has not been included in the calculations.

Figures 10.4 and 10.5 show the results of similar experiments for parallel scattering from 647.1nm to 635.8nm and 629.3nm respectively (correspond-
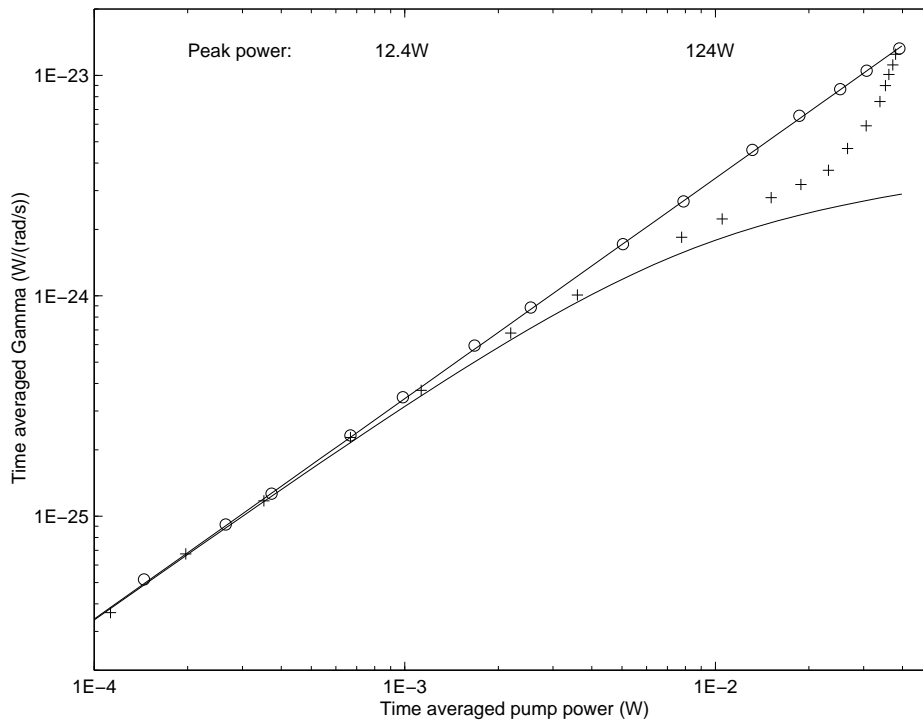
Figure 10.4: Same as Figure 10.2 but for the case of parallel scattering from 647.1nm to 635.8nm. Once again some measurements at low power, which have been included in fitting the straight line, are not shown on the graph.

Figure 10.5: Same as Figure 10.2 but for the case of parallel scattering from 647.1nm to 629.3nm. Once again some measurements at low power, which have been included in fitting the straight line, are not shown on the graph.
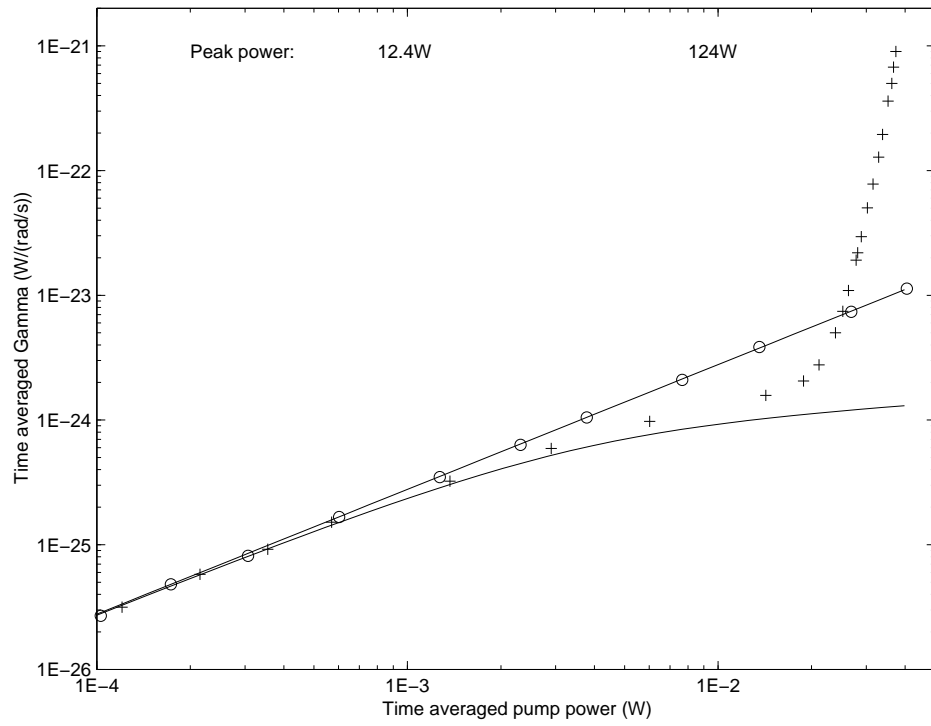
ing to values for Ω of -51.8rad/s and -82.4rad/s respectively). In these experiments, there is also an abrupt increase in scattered light in the high power limit. Raman scattering alone cannot account for this, since, in the case of anti-Stokes scattering, stimulated scattering is expected to attenuate rather than amplify the scattered light. A successful account of the scattering may require the inclusion of four wave mixing. However, identifying the angular frequencies of the photons being destroyed and created may not be straightforward. The obvious candidate of annihilating two pump photons and creating a Stokes/anti-Stokes pair would seem unlikely on the basis of poor phase matching. Consider, for example, the case of $|\Omega| = 82$rad/s. The maximum length over which electrons in the fibre make a coherent contribution to the four wave mixing (independent of whether the nonlinearity is electronic or nuclear in origin; see Section 3.5.3) is given by [5]

$$L_{coh} \simeq \frac{\pi}{|k_1 + k_2 - k_3 - k_4|} \tag{10.5}$$

where k_1 and k_2 (k_3 and k_4) are the angular wavenumbers of the photons destroyed (created). In the case of the annihilation of two pump photons and the creation of a Stokes/anti-Stokes pair, all on one axis of the fibre, Equation 10.5 reduces to [5]

$$L_{coh} \simeq \frac{\pi}{|\beta_2 \Omega^2 - 2\gamma P|} \tag{10.6}$$

Using values for β_2 and γ from Section 6.2.1, the term $2\gamma P$ is found to be negligible for pulses with peak powers less than 500W if $|\Omega| = 82.4$rad/s, and the resulting coherence length is only about 1cm.

10.3.2   Spectra at peak of gain

Some measurements were made using the same arrangement as for Figure 10.2, except that the scattered light was redirected into the OMA, as described in Section 10.2.1, and the spectrum recorded. Figure 10.6 shows spectra for the limits of low pump peak power and high pump peak power. The change in the shape of the spectrum observed to occur as the pump power is increased has been discussed by Stolen et al. [88].

10.4   Other sources of error

10.4.1   Averaging over the monochromator bandwidth

Thus far in this thesis, an assumption has been made that $\langle \Gamma_{\parallel} \rangle_t$ is approximately constant over the bandwidth of the monochromator (see Section 6.3).
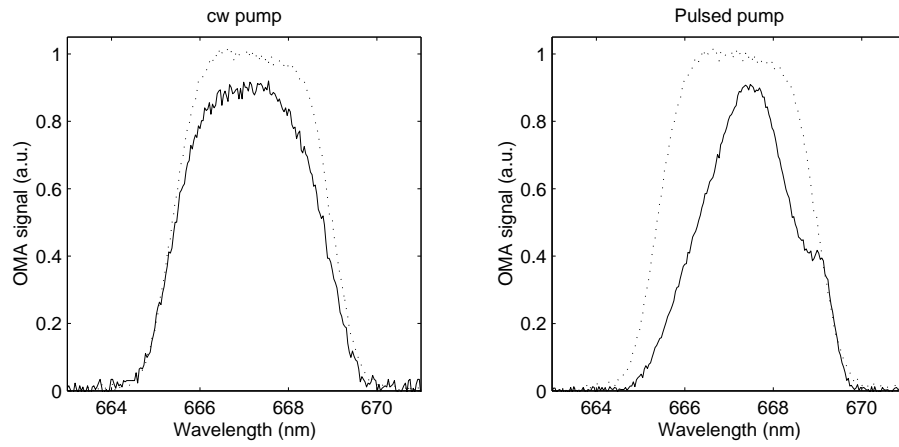
Figure 10.6: Spectra of light parallel scattered from 647.1nm to approximately 666nm (see also Figure 10.2). The dotted line is the spectrum of the white light source (see Sections 7.3 and 8.4.3), normalized to unity, so this gives an estimate for the filter function of the monochromator (see Section 6.3). In the left graph, the solid curve is the signal recorded by the OMA using the cw pump with an average power of 3.32mW at the end of the fibre. In the right hand graph, the solid curve is the signal recorded by the OMA using the pulsed pump with an average power of 30.7mW at the end of the fibre. In both cases, the spectra have been normalized to 0.9.

In particular, the theoretical predictions in Section 10.3.1 have been calculated assuming such a flat spectrum. One feature of a flat spectrum is that its shape does not change with pump power (it's always just flat). However, Figure 10.6 clearly shows that the cw spectrum is not flat, and that there is a considerable difference in shape between the spectra in the limits of high and low peak power (the growth of the shoulder at about 669nm has been observed previously [88]). The theoretical predictions in Section 10.3.1 are therefore in error. The remainder of this section is dedicated to estimating the size of this error.

In the experiments, what is measured is not $\langle \Gamma_\| \rangle_t$, but $\langle \Gamma_\| \rangle_t$ averaged over the bandwidth of the monochromator. Using Equations 6.18 and 6.17, this average is given by

$$\left\langle \langle \Gamma_\| \rangle_t \right\rangle_\omega = \frac{\int d\omega' \, F(\omega') \, \langle \Gamma_\| \rangle_t}{\int d\omega' \, F(\omega')}. \qquad (10.7)$$

(Here the dependence of $\langle \Gamma_\| \rangle_t$ on ω has not been made explicit. Also, use has been made of the fact that F is non-zero only on a narrow interval of angular frequencies and that, on this interval, η and ω are constant to good approximation). In the limit of low pump power, $\langle \Gamma_\| \rangle_t$ is given by the time average of Equation 6.2, so Equation 10.7 reduces to

$$\left\langle \langle \Gamma_\| \rangle_t \right\rangle_\omega = \frac{\int d\omega \, F(\omega) \, R_\|}{\int d\omega \, F(\omega)} \, \frac{\omega}{\omega_p} \, \langle P_p \rangle_t \, z. \qquad (10.8)$$

(Again, use has been made of the result that F is narrow band.) Hence, the measurements with the cw laser allow an average value for $R_\|$ to be inferred. This average is given by

$$\left\langle R_\| \right\rangle_\omega = \frac{\int d\omega \, F(\omega) \, R_\|}{\int d\omega \, F(\omega)} \qquad (10.9)$$

Using Equation 10.3 a corresponding averaged value for $g_\|$, $\langle g_\| \rangle_\omega$, can then be determined. The theoretical predictions in Section 10.3.1 are then obtained from Equation 6.15, using $\langle R_\| \rangle_\omega$ and $\langle g_\| \rangle_\omega$ in place of $R_\|$ and $g_\|$. If the spectrum is not flat, this does not give the same result as substituting the expression for $\langle \Gamma_\| \rangle_t$ from Equation 6.15 directly into Equation 10.7, and it is this that is required in order to accurately model the experiments.

To put in some numerical values, consider the case of Figure 10.2, where $\langle R_\| \rangle_\omega = 6.52 \times 10^{-22} \mathrm{m}^{-1} (\mathrm{rad/s})^{-1}$ (see Section 10.3.1). Suppose that F is a top hat function with width 3.6nm (a reasonable approximation to the white light spectrum in Figure 10.6), and that $R_\|$ varies linearly with angular

frequency over the width of the top hat. The peak to peak variation in $R_\parallel$ over the top hat might be as little as 10% (suggested by the left graph in Figure 10.6) or as large as 30% (suggested by Figure 9.6). In the high power limit (pump is the pulsed laser with 30mW average pump power at the end of the fibre), the experimental value for $\left\langle \left\langle \Gamma_\parallel \right\rangle_t \right\rangle_\omega$ (from Figure 10.2) is approximately $0.7 \times 10^{-19} \mathrm{W(rad/s)^{-1}}$. The value for $\left\langle \left\langle \Gamma_\parallel \right\rangle_t \right\rangle_\omega$ calculated by substituting $\left\langle R_\parallel \right\rangle_\omega$ and $\left\langle g_\parallel \right\rangle_\omega$ in place of $R_\parallel$ and $g_\parallel$ into Equation 6.15 (which is how the theoretical prediction in Figure 10.2 has been obtained) is $3.25 \times 10^{-19} \mathrm{W(rad/s)^{-1}}$, irrespective of the variation in $R_\parallel$. On the other hand, the value for $\left\langle \left\langle \Gamma_\parallel \right\rangle_t \right\rangle_\omega$ obtained by substituting Equation 6.15 into Equation 10.7 is $3.45 \times 10^{-19} \mathrm{W(rad/s)^{-1}}$ for a 10% variation in $R_\parallel$ and $5.35 \times 10^{-19} \mathrm{W(rad/s)^{-1}}$ for a 30% variation in $R_\parallel$. The theoretical prediction in Figure 10.2 has therefore been underestimated in the limit of high pump power by between 6% and 60%. Although this sounds like a large error, it is still comparable to the random error in the experimental measurements. Note, however, that if the theoretical predictions are underestimates then the disagreement between theory and experiment in the limit of high pump power is probably even worse than Figure 10.2 suggests.

10.4.2   Pulsed laser intensity fluctuations

The pulses produced by the pulsed laser were not all identical. The difference in energy between the pulses of maximum and minimum energy was about 5% of the pulse energy. This variation was due to 50Hz noise. In Section 10.3.1, the theoretical predictions have been obtained assuming the pulses are all identical. Using a procedure similar to that in Section 10.4.1, it is straightforward to show that, in the case of Figure 10.2, including the 5% energy fluctuations raises the theoretical predictions in the limit of high peak power by about 1.6%, a negligible amount in the context of this thesis.

10.4.3   Sensitivity to calibration

The theoretical predictions in Section 10.3.1 become very sensitive to errors in calibration in the limit of high pump power. For example, in the case of Figure 10.2 with an average pump power of 30mW, a 5% revision in the estimated value of the monochromator bandwidth (see Section 10.2.1) modifies the experimental data by 5%, but changes the theoretical prediction by a factor of 1.8. The same holds for a 5% change in the calibration of the monochromator collection efficiency (see Section 8.4.1) or a 5% change in the responsivity of the 818-UV (see Section 8.3.3). A 5% change in the

estimated pulse duration (see Section 10.2.2) leaves the experimental data unchanged, but modifies the theoretical predictions by a factor of 1.7.

10.4.4 Theoretical approximations

The sensitivity to calibration may not be quite enough to account for the mismatch between theoretical predictions and experimental results observed in Figure 10.2 in the limit of high pump power. Of course the theoretical predictions are only approximate since some effects are neglected, for example walk off (see Section 6.2.2) and four wave mixing (see Section 5.6). However, it may also be necessary to revisit some of the other assumptions in deriving equations for the Raman effect (Section 5.6), such as the assumption that the phonon modes remain in thermal equilibrium.

Chapter 11

Conclusion

The spontaneous scattering probability has been measured in an optical fibre
for frequency shifts from 4THz to 58THz for both parallel and perpendicular
scattering. There is a minimum in the perpendicular scattering probability
at a frequency shift of 27.7THz which may provide a useful window in which
four wave mixing experiments can be performed free of Raman noise.

The random error in the measured scattering probability is small in com-
parison to the estimated systematic error. In the case of scattering to the
peak of the gain, the largest sources of systematic error are the assumption
that the fibre loss is wavelength independent, the assumption that the mode
shape in the fibre is Gaussian and the uncertainty in the measured band-
width of the monochromator. The actual mode shape in the fibre could be
determined more accurately using existing data. To resolve the issues of
fibre loss and monochromator bandwidth would require further experiments.

The spontaneous scattering probability measured in the fibre has been
compared with measurements of the spontaneous scattering probability in
bulk glass made by Stolen and Ippen [83] and Hellwarth et al. [42]. The
fibre measurement is found to be about 8% larger than the value obtained
by Hellwarth et al. (which is within experimental error) and about 25%
larger than the value obtained by Stolen and Ippen (which is not within
experimental error). Measurements of the stimulated gain in optical fibres
by other authors have tended to support the value obtained by Stolen and
Ippen, or suggest an even lower value.

Other aspects of the spontaneous scattering have also been tested, namely
the ratio of perpendicular to parallel scattering, the ratio of anti-Stokes to
Stokes scattering and, to a very limited extent, the time response. In all
cases, the results have proven consistent with currently accepted theory.

At increased pump powers the transition from spontaneous to stimulated
scattering has been observed and compared with theoretical predictions. The

137

theoretical predictions assume that Raman scattering is the only significant effect. In the case of Stokes scattering to the peak of the gain the experimental results and theoretical predictions are in reasonable agreement. For scattering to other frequency shifts the agreement is less good. In particular, in the case of anti-Stokes scattering, and in the limit of very high pump power, behaviour is observed which is not predicted by the theory. This indicates that other effects, such as four wave mixing, must be included in the theory in order to successfully describe these experiments. The inclusion of four wave mixing is an obvious candidate for further research.

It should be clear from the work done in this thesis, and the work done by others reviewed in Chapter 2, that the stage has not yet been reached where Raman scattering experiments have been performed across a wide range of experimental regimes, the results of the experiments compared with theoretical predictions, and good agreement found between experiment and theory in all cases. Indeed there remain some issues which do not seem to have received adequate attention, either theoretically or experimentally. For example, how the scattering is to be dealt with in fibres which do not preserve polarization (see Section 5.4) and to what extent the phonon modes may be assumed to remain in thermal equilibrium (see 7, Section 5.6) (and, for the author at least, why equations derived assuming the signal modes are in number states can be used to describe experiments in which the signal may be in a more arbitrary state).

If further experiments are to be performed at Auckland, it is certainly possible to envisage ways in which the apparatus might be modified. If it was required, the bandwidth of the monochromator could be greatly reduced by bringing the light to a tight focus at one point in the monochromator. In some experimental regimes the scattering (even the spontaneous scattering) is sufficiently strong that measurements could, in principle, be made with the OMA (see 8.4.3). This would eliminate the tedious and time consuming task of aligning the monochromator for each frequency shift and also allow data for a range of frequency shifts to be collected simultaneously (saving even more time). In order to use the OMA, it would be necessary to first filter the light leaving the fibre in order to eliminate as much of the pump as possible (at least this is certainly the case for forward, parallel scattering). Other authors have done this using holographic filters (see, for example, [75] and references therein). If experiments were to be performed in long lengths of fibre (kilometres) at telecommunications wavelengths, it might be possible [61] to perform the filtering using some of the all fibre devices (such as Bragg gratings) which have been developed for telecommunications systems based on wavelength division multiplexed protocols.

Appendix A

Quantum theory for the Raman effect

This appendix gives the full quantum theory for vibrational Raman scattering in glass. The development of the theory is not free of simplifying assumptions, and these assumptions are stressed. The theory yields the equations for the Raman effect quoted in Chapter 5. As mentioned in Section 5, the books by Long [51] and Loudon [53] were influential in preparing this appendix.

A.1 Description of matter

As mentioned in Section 3.1.1, each atom in a glass is held to all the other atoms by a network of covalent bonds so that any piece of glass is really one giant molecule. This is difficult to deal with theoretically, so the first approximation is to assume that the glass is made up of many discrete molecules which do not interact with one another. The molecules are assumed to be very much smaller than the wavelength of light, all different from each other (which will lead to inhomogeneous broadening) and somehow fixed in space with random orientations. The purpose of this section is to investigate the properties of one such molecule in the absence of any light.

A.1.1 Fundamental considerations

The molecule is made up of atoms. The nuclei in the atoms are taken as fundamental particles (the photon energies of visible light are insufficient to cause excitations among the nucleons). The Coulomb force is assumed to be the only force acting between the subatomic particles and the intrinsic spin

of the particles is neglected. If the particles are assumed to move at non-relativistic speed (which is found to be a good assumption) then the motion of the particles is completely determined by Schrödinger's non-relativistic wave equation. If the molecule contains M particles then this can be written

$$\left[\sum_{k=1}^{M} \frac{p_k^2}{2m_k} + V\left(\mathbf{r}_1, \ldots, \mathbf{r}_M\right)\right] \Psi\left(\mathbf{r}_1, \ldots, \mathbf{r}_M, t\right) = i\hbar \frac{\partial}{\partial t} \Psi\left(\mathbf{r}_1, \ldots, \mathbf{r}_M, t\right).$$

(A.1)

Here p_k is the operator for the magnitude of the momentum of particle k, m_k and $\mathbf{r}_k$ are the mass and position (respectively) of particle k, V is the total Coulomb interaction energy and Ψ the wavefunction in position space. This equation can be solved analytically only for the case of two particles. In the more general case, approximations are necessary. The first approximation (Born-Oppenheimer approximation [15, p477]) is to assume that the nuclei are stationary, classical particles. This is justified by the observation that the mass of a nucleus is typically three orders of magnitude larger than the mass of an electron. So the nuclei will move much more slowly and have a much smaller de Broglie wavelength. This then leaves the problem of solving for the motion of the electrons (once this is done, the motion of the nuclei will be reappraised).

A.1.2   Motion of the electrons

If the molecule contains N electrons, then in the Born-Oppenheimer approximation, the Schrödinger wave equation becomes

$$\left[\sum_{k=1}^{N} \frac{p_k^2}{2m_e} + V\left(\mathbf{r}_1, \ldots, \mathbf{r}_N; R\right)\right] \Psi\left(\mathbf{r}_1, \ldots, \mathbf{r}_N, t; R\right) = i\hbar \frac{\partial}{\partial t} \Psi\left(\mathbf{r}_1, \ldots, \mathbf{r}_N, t; R\right).$$

(A.2)

In this equation m_e is the mass of an electron, p_k is the operator for the magnitude of the momentum of the kth electron, $\mathbf{r}_k$ is the position of the kth electron, R is a parameter which takes into account the position of the nuclei and Ψ is now the wavefunction for the electrons only. By making the identification

$$\Psi\left(\mathbf{r}_1, \ldots, \mathbf{r}_N, t; R\right) = \psi_q\left(\mathbf{r}_1, \ldots, \mathbf{r}_N; R\right) e^{-i\omega_q t}, \qquad (A.3)$$

Equation A.2 becomes

$$\left[\sum_{k=1}^{N} \frac{p_k^2}{2m_e} + V\left(\mathbf{r}_1, \ldots, \mathbf{r}_N; R\right)\right] \psi_q\left(\mathbf{r}_1, \ldots, \mathbf{r}_N; R\right) = \hbar\omega_q\, \psi_q\left(\mathbf{r}_1, \ldots, \mathbf{r}_N; R\right).$$

(A.4)

A solution ψ_q (the subscript is used because there is more than one) to Equation A.4 is called an eigenfunction. It is the wavefunction associated with an eigenstate $|q\rangle$ of the electrons. Since ψ_q will persist as a solution of Equation A.4 over a range of R, it is not necessary to make the state $|q\rangle$ an explicit function of R. Strictly speaking, the angular frequency ω_q will also be a function of R. This will be important in determining the motion of the nuclei in Section A.1.4. However, in the case of the electrons, the dependence of ω_q on R may be neglected, provided the nuclei only move over small distances (which will be the case in this thesis). The energy of the state $|q\rangle$ is then given by $\hbar\omega_q$.

In practice it is often found that the electrons move approximately independently of one another. This means that two eigenfunctions ψ_q and ψ_p may have a similar dependence on, for example, $\mathbf{r}_2, \ldots, \mathbf{r}_N$ and a distinct dependence only on $\mathbf{r}_1$. A change in state from $|q\rangle$ to $|p\rangle$ is therefore associated with a change in the state of just one electron.

The eigenfunctions ψ_q are usually assumed to be complex valued (see any quantum mechanics text which lists the eigenfunctions of the hydrogen atom for example). In fact, if V is given by the Coulomb interaction, then Equation A.4 has a set of orthonormal eigenfunctions which are real, so it is possible to make the assumption that the eigenfunctions ψ_q are real rather than complex. To see this, suppose that $\psi_q = f + ig$ where f and g are real. ψ_q is a solution of Equation A.4 only if f and g are solutions of Equation A.4. ψ_q can be normalized (i.e. $\int \psi_q^* \psi_q$ made to equal unity) only if f and g can be normalized. Hence the real eigenfunctions of Equation A.4 are a complete set. The orthogonality of the real eigenfunctions is established as follows. Eigenfunctions belonging to distinct eigenvalues can be shown to be orthogonal by using the fact that they are solutions of Equation A.4. In the case of eigenfunctions belonging to the same eigenvalue, a Gram-Schmidt procedure can be used to obtain a set of real linear combinations of the eigenfunctions which are guaranteed to be orthogonal.

The general solution of Equation A.2 can now be written

$$\Psi\left(\mathbf{r}_1, \ldots, \mathbf{r}_N, t; R\right) = \sum_q c_q\left(t\right) \psi_q\left(\mathbf{r}_1, \ldots, \mathbf{r}_N; R\right) e^{-i\omega_q t}. \qquad \text{(A.5)}$$

The c_q are actually constants, independent of time, but an explicit time dependence is included at this stage in anticipation of Section A.4.1. At this stage there is no interaction with the electromagnetic field (this will be included in Section A.4.2) so $|c_q|^2$, which represents the probability of the electrons being found in state $|q\rangle$, does not change with time (there are no transitions).

Further insight into the motion of the electrons is given by the expectation value of their total dipole moment

$$\langle \mathbf{D}(R) \rangle = e \int d^3\mathbf{r}_1 \ldots \int d^3\mathbf{r}_N \, \Psi^* \left[\sum_{k=1}^{N} \mathbf{r}_k \right] \Psi. \tag{A.6}$$

Here e is the charge on the electron and Ψ is as given by Equation A.5. Notice that $\langle \mathbf{D}(R) \rangle$ is related to the average position of the electrons. If the electrons are in an eigenstate (all c_q are zero except one) then $\langle \mathbf{D}(R) \rangle$ is found to be independent of time and there is no motion in the classical sense. On the other hand, if the electrons are in the superposition state $(|p\rangle + |q\rangle)/\sqrt{2}$ then, depending on the shape of the eigenfunctions ψ_p and ψ_q, $\langle \mathbf{D}(R) \rangle$ may have a component oscillating sinusoidally with an angular frequency given by $|\omega_p - \omega_q|$.

A.1.3 Dirac notation and second quantization

The Schrödinger wave equation, Equation A.2, contains information about two things; the distribution of the electrons in space and the evolution of the system in time. Once the eigenfunctions have been found the first of these is no longer of interest. Second quantization (see [53]) provides a means of rewriting Equation A.2 so that only the time evolution is retained. The time evolution is determined by the Schrödinger equation, which, adopting Dirac's notation, now takes the form

$$H |\chi(t)\rangle = i\hbar \frac{\partial}{\partial t} |\chi(t)\rangle \tag{A.7}$$

where $|\chi(t)\rangle$ is the state of the system and H the Hamiltonian. In the case of Equation A.2 the appropriate Hamiltonian is

$$H_e = \sum_q \hbar \omega_q |q\rangle \langle q|. \tag{A.8}$$

Equation A.7 then has general solution

$$|\chi(t)\rangle_e = \sum_q c_q(t) \, e^{-i\omega_q t} |q\rangle \tag{A.9}$$

where the c_q are still independent of time at this stage.

It is convenient to introduce the dipole matrix elements $\mathbf{d}_{pq}(R)$ defined by

$$\mathbf{d}_{pq}(R) = e \int d^3\mathbf{r}_1 \ldots \int d^3\mathbf{r}_N \, \Psi_p^* \left[\sum_{k=1}^{N} \mathbf{r}_k \right] \Psi_q \tag{A.10}$$

and dipole moment operator $\mathbf{D}(R)$ for the electrons

$$\mathbf{D}(R) = \sum_{p,q} \mathbf{d}_{pq}(R) \, |p\rangle \langle q| . \tag{A.11}$$

Note that the dipole matrix elements are real (since the eigenfunctions are real) and that $\mathbf{d}_{pq}(R) = \mathbf{d}_{qp}(R)$. The expectation value of the dipole moment of the electrons introduced in Section A.1.2 is now given by

$$_e\langle \chi(t)| \, \mathbf{D}(R) \, |\chi(t)\rangle_e .$$

Of the states $|q\rangle$, one will have minimum energy. Let this state be denoted by $|g\rangle$, the ground state for the electrons. (In this thesis, it will be assumed that the ground state of the electrons is non-degenerate. For chemically inert substances like glass this is a reasonable assumption; molecules with degenerate ground states are expected to be chemically reactive because they can accept additional electrons into a level of low energy.) For atoms the diagonal dipole matrix elements (those $\mathbf{d}_{pq}(R)$ with $p = q$) are zero because the potential V is invariant under space inversion through the nucleus (see [53]). In molecules the symmetry is absent and the diagonal matrix elements can be non-zero. For example, in polar molecules the ground state has a permanent dipole moment ($\mathbf{d}_{gg}(R)$ is non-zero). However, the average separation between electrons and protons is expected to be much smaller than the radius of a typical electron orbit. From this it follows that the diagonal matrix elements are expected to be much smaller than the off diagonal elements. In this thesis, it will be assumed that the diagonal elements are all zero.

The existence of many excited states for the electrons will turn out to be something of a detail. In much of what follows it will be more convenient to consider just two levels; the ground state $|g\rangle$ and a single excited state $|e\rangle$. The dipole moment operator then simplifies to

$$\mathbf{D}(R) = \mathbf{d}_{eg}(R) \, (|e\rangle \langle g| + |g\rangle \langle e|) . \tag{A.12}$$

In Section A.5.1 the multiple levels will be restored.

A.1.4 Motion of the nuclei – classical mechanics

The energy of the ground state of the electrons is $E_g(R) = \hbar\omega_g(R)$. As indicated, this energy depends on the position of the nuclei. Suppose that a position of the nuclei, R_0 can be found at which $E_g(R)$ has a local minimum. If the nuclei are positioned at this minimum, they experience a potential well. If the well is deep enough the position of the nuclei will be constrained and

this results in a stable molecule. In general there will be several possible local minima. These correspond to different stable arrangements of the particles in space, or, in other words, to the formation of different molecules. The study of transitions between these minima is chemistry in a nutshell.

The next task is to analyze the motion of the nuclei in the vicinity of a stable minimum R_0. If there are $M - N$ nuclei then this problem involves $3(M - N)$ degrees of freedom. It is more convenient to imagine that the problem has only two degrees of freedom. The physics is essentially the same and it certainly helps keep the notation transparent.

Suppose $Q_a\mathbf{a}_1 + Q_b\mathbf{b}_1$ is the displacement of the first nucleus from its equilibrium position at R_0, $Q_a\mathbf{a}_2 + Q_b\mathbf{b}_2$ the displacement of the second nucleus, and so on. Here $\{\mathbf{a}_1, \ldots, \mathbf{a}_{M-N}\}$ and $\{\mathbf{b}_1, \ldots, \mathbf{b}_{M-N}\}$ are fixed sets of vectors and Q_a and Q_b are variable amplitudes. The energy, $E_g(R)$ can be written as a Taylor series expansion about R_0. Using the fact that $E_g(R_0)$ is a local minimum, so that at R_0, $\partial E_g(R)/\partial Q_a$ and $\partial E_g(R)/\partial Q_b$ must both be zero, the Taylor series expansion must take the form

$$E_g(R) = E_g(R_0) + \frac{1}{2}k_a Q_a^2 + \frac{1}{2}k_b Q_b^2 + k_{ab}Q_a Q_b + \text{higher order terms.} \quad (A.13)$$

For small displacements the higher order terms are negligible and Q_a and Q_b appear as the displacements of coupled harmonic oscillators. A judicious choice of the sets of vectors $\{\mathbf{a}_1, \ldots, \mathbf{a}_{M-N}\}$ and $\{\mathbf{b}_1, \ldots, \mathbf{b}_{M-N}\}$ results in $k_{ab} = 0$. Q_a and Q_b then appear as displacements of independent harmonic oscillators. These independent harmonic oscillators are called normal modes of vibration and they will, in general, involve the collective motion of more than one, and possibly many, nuclei. The quantities Q_a and Q_b are called normal coordinates.

In general, there will be $3(M - N)$ normal coordinates. Let these be denoted by Q_l, $l = 1, \ldots, 3(M - N)$. In subsequent sections it will be useful to have a Taylor series expansion for the dipole moment operator for the electrons about R_0. This can be obtained by first expanding the dipole matrix elements

$$\mathbf{d}_{pq}(R) = \mathbf{d}_{pq}(R_0) + \sum_l \left.\frac{\partial \mathbf{d}_{pq}(R)}{\partial Q_l}\right|_{R_0} Q_l + \text{higher order terms.} \quad (A.14)$$

It is convenient to introduce the notation

$$\mathbf{d}_{pq} = \mathbf{d}_{pq}(R_0) \text{ and } \mathbf{d}'_{pql} = \left.\frac{\partial \mathbf{d}_{pq}(R)}{\partial Q_l}\right|_{R_0}. \quad (A.15)$$

Note that, since the $\mathbf{d}_{pq}$ are real with $\mathbf{d}_{pq} = \mathbf{d}_{qp}$, the $\mathbf{d}'_{pql}$ are also real with $\mathbf{d}'_{pql} = \mathbf{d}'_{qpl}$.

In much of what follows, the existence of more than one mode of vibration is something of a detail. It is therefore convenient to assume there is just one mode of vibration and drop the subscript l. This will be reviewed in Section A.5.2. The dipole moment operator for the electrons then becomes

$$\mathbf{D} = \left(\mathbf{d}_{eg} + \mathbf{d}'_{eg}\, Q\right) \left(|e\rangle\langle g| + |g\rangle\langle e|\right). \tag{A.16}$$

A.1.5 Motion of the nuclei – quantum mechanics

Having established that the modes of vibration are independent harmonic oscillators, it is useful to review the properties of such oscillators. In the case of just one oscillator, the appropriate Hamiltonian, H_n, for the nuclear motion, to be used in the Schrödinger equation (Equation A.7), is

$$H_n = \hbar\Omega b^\dagger b \tag{A.17}$$

where Ω is the angular frequency of the mode and b and $b^\dagger$ are the annihilation and creation operators (respectively) for the mode. The eigenstates of this Hamiltonian are number states $|n\rangle$. These are equally spaced in energy with $H_n |n\rangle = n\hbar\Omega |n\rangle$. In this thesis, the quanta of energy associated with a vibrational mode will be called phonons (note that, as a small molecule is being considered, this usage is not strictly correct).

The general solution for the state of the oscillator $|\chi(t)\rangle_n$ is

$$|\chi(t)\rangle_n = \sum_{n=0}^{\infty} c_n(t)\, e^{-in\Omega t} |n\rangle. \tag{A.18}$$

At this stage the $c_n(t)$ are actually independent of time (in the absence of any interaction, phonons are neither created nor destroyed).

The following relations will prove useful.

$$b|n\rangle = \sqrt{n}\,|n-1\rangle \ \text{ and } \ b^\dagger |n\rangle = \sqrt{n+1}\,|n+1\rangle. \tag{A.19}$$

Insight into the motion of the oscillator can be gained through the position operator Q given by

$$Q = \sqrt{\frac{\hbar}{2\mathcal{M}\,|\Omega|}}\, \left(b + b^\dagger\right). \tag{A.20}$$

where $\mathcal{M}$ is the effective mass of the vibrational mode. At this point, taking the absolute value of Ω is rather redundant, as Ω is positive. However, in subsequent sections the absolute value braces will prove useful. If the oscillator is in the superposition state $(e^{-in\Omega t}|n\rangle + e^{-im\Omega t}|m\rangle)/\sqrt{2}$ then $\langle Q\rangle =$

0 and there is no motion, unless $|n - m| = 1$ in which case $\langle Q \rangle$ oscillates sinusoidally with angular frequency Ω (use Equation A.19).

In practice, typical values for Ω are much smaller than typical values of $\omega_e - \omega_g$ (angular frequencies between excited and ground states of the electrons). Also, provided the number of phonons in the vibrational mode is small (which will be the case in this thesis), the space wavefunctions for the nuclei are found to be well localized in comparison to the dimensions over which the electrons move. This justifies the Born-Oppenheimer approximation, which treated the nuclei as stationary, classical particles while analyzing the motion of the electrons.

A.2   Description of light

This section gives a description for the behaviour of light in the absence of matter.

A.2.1   The electromagnetic field–classical mechanics

It is customary in classical electrodynamics to begin with Maxwell's equations in differential form. In order to make the transition to quantum mechanics it is necessary to recast the equations in Hamiltonian form (see [27] and [28]. The Hamiltonian formulation needs a finite volume, since the Hamiltonian, which represents the total energy, must not diverge. This insistence on a finite volume is not such a restriction since, once the transition to quantum mechanics has been made, the boundary can be taken to infinity. This also justifies assigning an arbitrary value to the field on the boundary (for example, imposing periodic boundary conditions).

In such a bounded system, the general solution for the electric field (assuming there are no charged particles) can be written [97, p9]

$$\mathbf{E}\left(\mathbf{r}, t\right) = i \sum_k \sqrt{\frac{\hbar \omega_k}{2 \epsilon_0}} \left[\alpha_k e^{-i \omega_k t} \mathbf{u}_k\left(\mathbf{r}\right) - c.c. \right]. \tag{A.21}$$

Here each α_k is an arbitrary, complex constant and *c.c.* denotes complex conjugate. The functions $\mathbf{u}_k$ are called mode functions. They satisfy the time independent part of the wave equation

$$\left(\nabla^2 + \frac{\omega_k^2}{c^2} \right) \mathbf{u}_k = 0, \tag{A.22}$$

and also the transversality condition

$$\nabla \cdot \mathbf{u}_k = 0. \tag{A.23}$$

The mode functions are normalized and, because of the boundary conditions, orthogonal, so that

$$\int_V d^3\mathbf{r}\, \mathbf{u}_k^* \cdot \mathbf{u}_{k'} = \delta_{kk'}. \tag{A.24}$$

In the Hamiltonian formulation, a generalized coordinate, Q_k can be introduced, associated with the mode function $\mathbf{u}_k$. When the Hamiltonian is written in terms of the Q_k and their conjugate momenta, the field appears equivalent to a sum of harmonic oscillators, one harmonic oscillator for each field mode.

A.2.2 The electromagnetic field–quantum mechanics

The quantum mechanics of independent harmonic oscillators has already been discussed in Section A.1.5. There will be an annihilation operator a_k and creation operator $a_k^\dagger$ associated with each field mode. The details of the Hamiltonian formulation show that $\alpha_k e^{-i\omega_k t}$ in the classical theory is replaced by a_k in the quantum theory. So the electric field operator is

$$\mathbf{E}(\mathbf{r}, t) = i \sum_k \sqrt{\frac{\hbar\omega_k}{2\epsilon_0}} \left[a_k \mathbf{u}_k(\mathbf{r}) - h.c. \right] \tag{A.25}$$

where $h.c.$ denotes Hermitian conjugate.

The Hamiltonian for the field, to be used with the Schrödinger equation (Equation A.7), is

$$H_F = \sum_k \hbar\omega_k\, a_k^\dagger a_k \tag{A.26}$$

The energy eigenstates of the field mode k are number states $|n\rangle_k$, equally spaced in energy. The quanta of energy which separate adjacent number states are called photons.

A.3 Light in dielectrics

A.3.1 The linear refractive index

When light propagates in a dielectric, like glass, there are several physical phenomena which occur, for example, Rayleigh scattering, Brillouin scattering, the reduction in speed of light associated with the linear refractive index. In discussing the Raman effect, none of these need be considered except for the linear refractive index.

The origin of the linear refractive index are the processes in which a photon is absorbed and then re-emitted into the same made, with no overall change in the state of matter, as depicted in Figure 3.4. It can be shown that these are completely accounted for if ϵ_0 in Equations A.21 and A.25 is replaced with

$$\epsilon_k = \epsilon_0 n_k^2 \tag{A.27}$$

where the phase velocity of mode k is c/n_k (the derivation of this follows the formalism about to be used for the Raman effect). Actually, this is only strictly true for dielectrics in which there is no dispersion, but glass is only weakly dispersive, so this result will be assumed to hold. Also, for the geometries encountered in this thesis, the effective refractive index, n_k, is found to depend only on the frequency of the mode. Hence, ϵ_k can be written $\epsilon(\omega_k)$.

A.3.2 Mode functions for a single mode fibre

As discussed in Section A.2.1, the analysis must begin with a finite section of fibre. With reference to the coordinate frame in Figure 4.1a, suppose that this piece extends from $z = z_0$ to $z = z_0 + L$ (remember that these boundaries are hypothetical) and that periodic boundary conditions are imposed so that the field at z_0 is the same as the field at $z_0 + L$. Consider the case of waves travelling in the $+z$ direction. The mode functions can then be written

$$\mathbf{u}_k(\mathbf{r}) = \mathbf{e}\, f_k(x, y)\, \frac{1}{\sqrt{L}} e^{i\beta_k z}. \tag{A.28}$$

Here $\mathbf{e}$ is a unit vector which specifies the (linear) polarization and may take either of two orthogonal directions (in the case of a HiBi fibre, the directions must be taken parallel to the fast and slow axes), f_k is the transverse mode profile (see Sections 4.2 and 4.4) for light of angular frequency ω_k, and the angular wavenumber β_k is given by

$$\beta_k = \frac{2\pi k}{L} \tag{A.29}$$

where k is a positive integer. β_k and ω_k are related by

$$\omega_k = c(\omega_k)\, \beta_k. \tag{A.30}$$

Here $c(\omega)$ is the phase velocity of a wave in the fibre with angular frequency ω.

It will be useful to introduce the density of field modes, defined as the number of field modes per unit angular frequency in the vicinity of angular

frequency ω. In the case of a fibre the density of field modes, $\rho_f(\omega)$ is given by

$$\rho_f(\omega) = \frac{L}{2\pi c(\omega)}. \tag{A.31}$$

As the length L is increased, the density of field modes increases but the amplitude of the mode functions decreases. As a consequence, the quantity $\rho_f(\omega_k)|\mathbf{u}_k(\mathbf{r})|^2$, which is important in the mathematics of the interaction of light with matter, is independent of L and given by

$$\rho_f(\omega_k)|\mathbf{u}_k(\mathbf{r})|^2 = \frac{f_k(x,y)^2}{2\pi c(\omega_k)}. \tag{A.32}$$

A.3.3 Mode functions for bulk glass

As in the previous section, the analysis must begin with a finite volume. With reference to the coordinate frame in Figure 5.1, suppose that this is a cube of side L, with the same orientation as the coordinate frame and centred at the origin (this cube is assumed much larger than the imaginary volume element shown in the figure). Periodic boundary conditions are imposed so that the field at $(-L/2, y, z)$ is the same as the field at $(L/2, y, z)$ (and likewise for $y = \pm L/2$ and $z = \pm L/2$).

In the case of linearly polarized, travelling plane waves, the mode functions can be written

$$\mathbf{u_k}(\mathbf{r}) = \mathbf{e}\frac{1}{\sqrt{V}}e^{i\beta_{\mathbf{k}}\cdot\mathbf{r}} \tag{A.33}$$

where $\mathbf{e}$ is a unit vector which may take either of two orthogonal directions (which are in turn orthogonal to $\beta_{\mathbf{k}}$) and which defines the (linear) polarization, $V = L^3$ and the angular wavevector $\beta_{\mathbf{k}}$ is given by

$$\beta_{\mathbf{k}} = \frac{2\pi\mathbf{k}}{L} \tag{A.34}$$

where the components of $\mathbf{k}$ are all integers. The mode function $\mathbf{u_k}$ is associated with angular frequency $\omega_{\mathbf{k}}$ where

$$\omega_{\mathbf{k}} = c(\omega_{\mathbf{k}})|\beta_{\mathbf{k}}|. \tag{A.35}$$

In $\mathbf{k}$ space, each field mode occupies one unit of volume. Calculating volumes in $\mathbf{k}$ space is therefore a convenient means of counting field modes [53, Sec.1.1]. Using this approach the number of field modes per unit angular frequency (density of field modes) in the vicinity of ω, $\rho_b(\omega)$ is given by

$$\rho_b(\omega) = 4\pi\left(\frac{L}{2\pi c(\omega)}\right)^3 \omega^2 \tag{A.36}$$

The field modes are equally distributed in terms of propagation direction. This means that the number of field modes propagating in a direction that lies inside the solid angle $d\Phi$ in Figure 5.1 per unit angular frequency is given by $\rho_b(\omega) d\Phi/4\pi$. As in the case of fibres, multiplying this by $|\mathbf{u_k}(\mathbf{r})|^2$ gives an important quantity

$$\rho_b(\omega_\mathbf{k}) \frac{d\Phi}{4\pi} |\mathbf{u_k}(\mathbf{r})|^2 = \left(\frac{1}{2\pi c(\omega_\mathbf{k})} \right)^3 \omega_\mathbf{k}^2 d\Phi \qquad (A.37)$$

which is found to be independent of L.

A.4 Light and matter in interaction

A.4.1 Interaction picture

To begin now the problem of Raman scattering from the molecule. It is convenient to start with only two modes of the electromagnetic field; a pump mode and a signal mode (more signal modes will be added later). The pump mode will be assumed to be sufficiently intense that it can be treated classically. This means it will make a contribution to the electric field according to Equation A.21. Also, it will be assumed invariant under the addition or deletion of photons. The signal mode will be treated using quantum mechanics and will make a contribution to the electric field according to Equation A.25. The single molecule is imagined to be embedded in glass (either bulk glass or single mode fibre). Using Section A.3.1, the electric field can then be written

$$\mathbf{E}(\mathbf{r}, t) = i \left[\sqrt{\frac{\hbar\omega_p}{2\epsilon(\omega_p)}} \alpha e^{-i\omega_p t} \mathbf{u}_p(\mathbf{r}) - c.c. + \sqrt{\frac{\hbar\omega}{2\epsilon(\omega)}} a\mathbf{u}(\mathbf{r}) - h.c. \right] \quad (A.38)$$

where ω_p and ω are the angular frequencies, and $\mathbf{u}_p$ and $\mathbf{u}$ mode functions, for pump and signal (respectively), α determines the amplitude of the pump, and a is the annihilation operator for the signal mode. The state ket for the system of molecule and light can be written

$$|\psi(t)\rangle = \sum_{\substack{q = g, e \\ m = 0 \to \infty \\ n = 0 \to \infty}} c_{qmn}(t) e^{-i\omega_q t} e^{-im\Omega t} e^{-in\omega t} |q\rangle |m\rangle |n\rangle. \qquad (A.39)$$

Here $|q\rangle$ is either ground or excited state of the electrons, $|m\rangle$ is a number state for the phonon mode (which has angular frequency Ω) and $|n\rangle$ is a

number state for the signal mode (which has angular frequency ω). $|\psi(t)\rangle$ must satisfy the Schrödinger equation (Equation A.7) with total Hamiltonian

$$H = H_e + H_n + H_F + H' \tag{A.40}$$

where H_e, H_n and H_F are given by Equations A.8, A.17 and A.26 and H' is the Hamiltonian describing the interaction between molecule and field. Even in the case of moderately powerful lasers, H' is small in comparison to H_e, H_n and H_F, which justifies using the eigenstates of H_e, H_n and H_F as a basis for constructing $|\psi(t)\rangle$.

In the absence of any interaction ($H' = 0$), $|\psi(t)\rangle$ is a solution of the Schrödinger equation if the $c_{qmn}(t)$ are taken as constants, independent of time. Since $|c_{qmn}(t)|^2$ gives the probability of the system being in the eigenstate $|q\rangle|m\rangle|n\rangle$ at time t, this means that, in the absence of H', there are no transitions. But $|\psi(t)\rangle$ still evolves with time because of the presence of the rotating phasors. The rotating phasors therefore represent a rather uninteresting time evolution and are something of a nuisance.

Thus far all the quantum mechanics has been formulated in a Schrödinger picture, in which the operators are independent of time (see, for example, Equations A.11, A.20 and A.25). The rotating phasors can be eliminated by transforming to an interaction picture. The state ket in the interaction picture is defined by

$$|\psi(t)\rangle_I = e^{i(H_e + H_n + H_F)t/\hbar} |\psi(t)\rangle. \tag{A.41}$$

It follows from this that

$$|\psi(t)\rangle_I = \sum_{\substack{q = g, e \\ m = 0 \to \infty \\ n = 0 \to \infty}} c_{qmn}(t) |q\rangle |m\rangle |n\rangle. \tag{A.42}$$

The Schrödinger equation in the interaction picture is

$$H_I'(t) |\psi(t)\rangle_I = i\hbar \frac{\partial}{\partial t} |\psi(t)\rangle_I \tag{A.43}$$

where

$$H_I'(t) = e^{i(H_e + H_n + H_F)t/\hbar} H' e^{-i(H_e + H_n + H_F)t/\hbar}. \tag{A.44}$$

A.4.2 The electric dipole interaction

The interaction Hamiltonian can be written as a sum of terms [53]. In this sum the electric dipole term is usually dominant, allowing other terms, such

as those due to magnetic dipole and electric quadrupole interactions, to be neglected. In this case the interaction Hamiltonian is

$$H' = \mathbf{D} \bullet \mathbf{E}(\mathbf{r}). \tag{A.45}$$

Here $\mathbf{D}$ is the dipole moment operator and $\mathbf{E}(\mathbf{r})$ is the electric field operator evaluated at the position $\mathbf{r}$ of the molecule (the molecule is assumed to be very much smaller than the wavelength of light, so that $\mathbf{E}$ is approximately constant across the molecule). Strictly speaking, the dipole moment operator should be the total dipole moment due to all charged particle, including the nuclei. In the interaction of light and glass, the dipole moment of the nuclei is of some importance, since it causes the strong absorption of light at mid and far IR wavelengths (and hence the greenhouse effect). However, in the propagation of visible light, the dipole moment of the nuclei is not important, so in this thesis only the dipole moment of the electrons will be considered. With this approximation, and using Equations A.16, A.20 and A.38, H' becomes

$$H' = \left(\mathbf{d}_{eg} + \mathbf{d}'_{eg} \sqrt{\frac{\hbar}{2\mathcal{M}|\Omega|}} \left(b + b^{\dagger} \right) \right) \left(|e\rangle\langle g| + |g\rangle\langle e| \right)$$

$$\bullet\, i \left[\sqrt{\frac{\hbar\omega_p}{2\epsilon(\omega_p)}} \alpha e^{-i\omega_p t} \mathbf{u}_p(\mathbf{r}) - c.c. + \sqrt{\frac{\hbar\omega}{2\epsilon(\omega)}} a\mathbf{u}(\mathbf{r}) - h.c. \right] \tag{A.46}$$

Using Equation A.44, and with the aid of the Baker-Hausdorff formula [73], the corresponding interaction picture Hamiltonian is

$$H'_I(t) = \left(\mathbf{d}_{eg} + \mathbf{d}'_{eg} \sqrt{\frac{\hbar}{2\mathcal{M}|\Omega|}} \left(b e^{-i\Omega t} + b^{\dagger} e^{i\Omega t} \right) \right) \left(|g\rangle\langle e|\, e^{-i\omega_E t} + |e\rangle\langle g|\, e^{i\omega_E t} \right)$$

$$\bullet\, i \left[\sqrt{\frac{\hbar\omega_p}{2\epsilon(\omega_p)}} \alpha e^{-i\omega_p t} \mathbf{u}_p(\mathbf{r}) - c.c. + \sqrt{\frac{\hbar\omega}{2\epsilon(\omega)}} a e^{-i\omega t} \mathbf{u}(\mathbf{r}) - h.c. \right] \tag{A.47}$$

where

$$\omega_E = \omega_e - \omega_g \tag{A.48}$$

is the angular frequency associated with the motion of the electrons.

A.4.3   Perturbation theory

From here on, all calculations will be performed in the interaction picture. For convenience, the I subscript, which has been used to denote interaction picture kets and operators, will henceforth be omitted.

Suppose that at $t = 0$ the system is in the state $|g\rangle |m\rangle |n\rangle$ i.e.

$$|\psi (0)\rangle = |g\rangle |m\rangle |n\rangle . \qquad (A.49)$$

The state of the system at a later time is given by

$$|\psi (t)\rangle = |\psi (0)\rangle + \int_0^t dt' \; \frac{\partial}{\partial t} |\psi (t)\rangle \bigg|_{t'} \qquad (A.50)$$

where the brace $|_{t'}$ indicates that the partial derivative is to be evaluated at time t'. Using the Schrödinger equation (Equation A.43) this becomes

$$|\psi (t)\rangle = |\psi (0)\rangle + \frac{1}{i\hbar} \int_0^t dt' \, H' (t') \, |\psi (t')\rangle . \qquad (A.51)$$

The general solution to Equation A.51 can be written as the Dyson series

$$|\psi (t)\rangle = \left[1 + \frac{1}{i\hbar} \int_0^t dt' \, H' (t') + \left(\frac{1}{i\hbar} \right)^2 \int_0^t dt' \int_0^{t'} dt'' \, H' (t') \, H' (t'') \right.$$
$$\left. + \left(\frac{1}{i\hbar} \right)^3 \int_0^t dt' \int_0^{t'} dt'' \int_0^{t''} dt''' \, H' (t') \, H' (t'') \, H' (t''') + \dots \right] |\psi (0)\rangle \quad (A.52)$$

(this is easily checked by differentiating the series). The first integral in the series is referred to as the first order perturbation, the second integral, second order perturbation, and so on. Provided the time t is sufficiently short that $tH'/\hbar \ll 1$, successive orders will get rapidly smaller. In this case, it is only necessary to consider the first few orders, remaining orders being negligible. A value for H' can be estimated using Equation A.45, and assuming a classical picture. An order of magnitude estimate for the dipole moment of the electrons is the electronic charge multiplied by a typical atomic diameter, or $|\mathbf{D}| \simeq 1.6 \times 10^{-29}$Cm. The maximum electric field associated with a 100W peak power pulse propagating in a fibre with mode field radius 2μm, is $|\mathbf{E}| \simeq 1 \times 10^8$NC^{-1}. Hence, $\mathbf{D} \bullet \mathbf{E}/\hbar \simeq 1.6 \times 10^{13}$s^{-1}, corresponding to a time of 63fs. This is still quite long in comparison to 2fs, the approximate period of a red light wave.

A.4.4 Single photon absorption

Since H' could be expanded into a sum of terms (see Equation A.47), each of the integrals in the Dyson series (Equation A.52) could also be expanded into a sum of terms. One such term in the first integral is

$$\frac{1}{i\hbar} \int_0^t dt' \, \mathbf{d}_{eg} \, |e\rangle \langle g| \, e^{i\omega_E t'} \bullet i\sqrt{\frac{\hbar\omega}{2\epsilon (\omega)}} a e^{-i\omega t'} \mathbf{u} (\mathbf{r}) .$$

This will cause transitions from the initial state $|g\rangle |m\rangle |n\rangle$ to $|e\rangle |m\rangle |n-1\rangle$, corresponding to the absorption of a single photon from the signal mode and excitation of the electrons, as suggested by Figure 3.1. Since this is the only term which can cause a transition to this state, the probability of the transition having occurred at time t is

$$
\begin{aligned}
|\langle n-1| \langle m| \langle e| \psi(t)\rangle|^2 &= \left| \frac{1}{i\hbar} \int_0^t dt' \, \mathbf{d}_{eg} e^{i\omega_E t'} \bullet i\sqrt{\frac{\hbar\omega}{2\epsilon(\omega)}} \sqrt{n} e^{-i\omega t'} \mathbf{u}(\mathbf{r}) \right|^2 \\
&\propto \left| \int_0^t dt' \, e^{i(\omega_E - \omega)t'} \right|^2.
\end{aligned}
\tag{A.53}
$$

If $\omega \neq \omega_E$, which will be the case for visible light and fused silica, since ω_E in fused silica corresponds to the angular frequency of an ultraviolet photon (see Section 3.2.1), the phasor on the right hand side of Equation A.53 will be rapidly rotating. As a consequence, it will integrate to zero and the absorption of single photons will not occur. If $\omega \simeq \omega_E$, then the rotating phasor will be approximately constant and the integral will grow with time. Hence, in order for the transition to occur, it must be consistent with approximate overall energy conservation.

For the experimental regime in this thesis, none of the terms in the first integral satisfy energy conservation and all may be neglected.

A.5 Stokes scattering from pump to signal

To begin with, Stokes scattering from pump to signal will be the only process considered. Anti-Stokes scattering and scattering from signal to pump are considered in Sections A.8 and A.9 respectively.

A.5.1 Scattering from a single molecule

To reiterate, at this point, the scattering is still restricted to a single phonon mode, two photon modes, and a single excited state for the electrons (although the remaining excited states will be added imminently).

The second integral in the Dyson series contains the term

$$
\left(\frac{1}{i\hbar} \right)^2 \int_0^t dt' \int_0^{t'} dt'' \left[\mathbf{d}'_{eg} \sqrt{\frac{\hbar}{2\mathcal{M}|\Omega|}} b^\dagger e^{i\Omega t'} |g\rangle \langle e| e^{-i\omega_E t'} \right.
$$

$$
\left. \bullet (-i) \sqrt{\frac{\hbar\omega}{2\epsilon(\omega)}} a^\dagger e^{i\omega t'} \mathbf{u}^*(\mathbf{r}) \right] \left[\mathbf{d}_{eg} |e\rangle \langle g| e^{i\omega_E t''} \bullet i\sqrt{\frac{\hbar\omega_p}{2\epsilon(\omega_p)}} \alpha e^{-i\omega_p t''} \mathbf{u}_p(\mathbf{r}) \right].
$$

This converts the initial state $|g\rangle\,|m\rangle\,|n\rangle$ to $|g\rangle\,|m+1\rangle\,|n+1\rangle$, corresponding to Stokes scattering according to Figure 3.6a. The term makes a contribution to $\langle n+1|\,\langle m+1|\,\langle g|\,\psi(t)\rangle$ of

$$-\sqrt{\frac{\omega_p\omega}{8\hbar\epsilon(\omega_p)\,\epsilon(\omega)}}\sqrt{\frac{1}{\mathcal{M}\,|\Omega|}}\sqrt{m+1}\sqrt{n+1}\,\alpha\,\mathbf{d}'_{eg}\bullet\mathbf{u}^*(\mathbf{r})\,\mathbf{d}_{eg}\bullet\mathbf{u}_p(\mathbf{r})$$

$$\int_0^t dt'\int_0^{t'}dt''\,e^{i\Omega t'}e^{-i\omega_E t'}e^{i\omega t'}e^{i\omega_E t''}e^{-i\omega_p t''}.\quad\text{(A.54)}$$

Here, the factors $\sqrt{m+1}$ and $\sqrt{n+1}$ come from $b^\dagger$ and $a^\dagger$ acting on $|m\rangle$ and $|n\rangle$ (see Equation A.19). The second integral in the Dyson series contains three additional terms which also cause transitions from $|g\rangle\,|m\rangle\,|n\rangle$ to $|g\rangle\,|m+1\rangle\,|n+1\rangle$. These correspond to Figures 3.6b, 3.6c and 3.6d and make contributions of

$$-\sqrt{\frac{\omega_p\omega}{8\hbar\epsilon(\omega_p)\,\epsilon(\omega)}}\sqrt{\frac{1}{\mathcal{M}\,|\Omega|}}\sqrt{m+1}\sqrt{n+1}\,\alpha\,\mathbf{d}'_{eg}\bullet\mathbf{u}_p(\mathbf{r})\,\mathbf{d}_{eg}\bullet\mathbf{u}^*(\mathbf{r})$$

$$\int_0^t dt'\int_0^{t'}dt''\,e^{i\Omega t'}e^{-i\omega_E t'}e^{-i\omega_p t'}e^{i\omega_E t''}e^{i\omega t''},\quad\text{(A.55)}$$

$$-\sqrt{\frac{\omega_p\omega}{8\hbar\epsilon(\omega_p)\,\epsilon(\omega)}}\sqrt{\frac{1}{\mathcal{M}\,|\Omega|}}\sqrt{m+1}\sqrt{n+1}\,\alpha\,\mathbf{d}_{eg}\bullet\mathbf{u}^*(\mathbf{r})\,\mathbf{d}'_{eg}\bullet\mathbf{u}_p(\mathbf{r})$$

$$\int_0^t dt'\int_0^{t'}dt''\,e^{-i\omega_E t'}e^{i\omega t'}e^{i\Omega t''}e^{i\omega_E t''}e^{-i\omega_p t''},\quad\text{(A.56)}$$

and

$$-\sqrt{\frac{\omega_p\omega}{8\hbar\epsilon(\omega_p)\,\epsilon(\omega)}}\sqrt{\frac{1}{\mathcal{M}\,|\Omega|}}\sqrt{m+1}\sqrt{n+1}\,\alpha\,\mathbf{d}_{eg}\bullet\mathbf{u}_p(\mathbf{r})\,\mathbf{d}'_{eg}\bullet\mathbf{u}^*(\mathbf{r})$$

$$\int_0^t dt'\int_0^{t'}dt''\,e^{-i\omega_E t'}e^{-i\omega_p t'}e^{i\Omega t''}e^{i\omega_E t''}e^{i\omega t''},\quad\text{(A.57)}$$

to $\langle n+1|\,\langle m+1|\,\langle g|\,\psi(t)\rangle$ (respectively). If there is more than one excited state for the electrons, then transitions from $|g\rangle\,|m\rangle\,|n\rangle$ to $|g\rangle\,|m+1\rangle\,|n+1\rangle$ can occur via any of the excited states. Hence, $\langle n+1|\,\langle m+1|\,\langle g|\,\psi(t)\rangle$ is obtained by summing Equations A.54, A.55, A.56 and A.57 over all excited states for the electrons. Before writing down the result, it is helpful to change the vector dot products to matrix notation and evaluate (and then

simplify) the time integrals. Assuming vectors are column matrices, the dot products in Equation A.54 can be rewritten according to

$$\mathbf{d}'_{eg} \bullet \mathbf{u}^* (\mathbf{r}) \; \mathbf{d}_{eg} \bullet \mathbf{u}_p (\mathbf{r}) = \mathbf{u}_p (\mathbf{r})^t \; \mathbf{d}_{eg} \mathbf{d}'^t_{eg} \, \mathbf{u}^* (\mathbf{r}) \qquad \text{(A.58)}$$

where the superscript t denotes transpose. Note that $\mathbf{d}_{eg} \mathbf{d}'^t_{eg}$ is a three by three matrix (rank two tensor).

The time integral in Equation A.54 evaluates to

$$\frac{1}{i \, (\omega_E - \omega_p)} \left\{ \frac{1}{i \, (\Omega + \omega - \omega_p)} \left[e^{i(\Omega + \omega - \omega_p)t} - 1 \right] \right.$$
$$\left. - \frac{1}{i \, (\Omega - \omega_E + \omega)} \left[e^{i(\Omega - \omega_E + \omega)t} - 1 \right] \right\}. \qquad \text{(A.59)}$$

The first term inside the curly brackets in Equation A.59, has amplitude $1/ (\Omega + \omega - \omega_p)$. If $\Omega + \omega - \omega_p \simeq 0$, that is, if the transition satisfies approximate energy conservation, then this amplitude will become very large and there will be a large transition probability. Further analysis is restricted to this case. The second term in the curly brackets has amplitude $1/ (\Omega - \omega_E + \omega)$. In the experimental regimes encountered in this thesis, it is assumed that

$$\omega_p, \omega, |\Omega| \ll \omega_E, \qquad \text{(A.60)}$$

so $(\Omega - \omega_E + \omega) \simeq 0$ cannot occur (see Section A.4.4). So the first term has low frequency and large amplitude, and the second term has high frequency and small amplitude. The second term therefore has negligible effect on the long time evolution. In calculating the transition probabilities, it is the long time evolution which is of interest (this is true provided the pump is not rapidly changing with time). The second term in Equation A.59 can therefore be discarded. The time integrals in Equations A.55, A.56 and A.57 also simplify in a similar way.

Having changed the notation for the dot products and simplified the time integrals, $\langle n + 1 | \langle m + 1 | \langle g | \, \psi (t) \rangle$, obtained by summing Equations A.54, A.55, A.56 and A.57 over all excited states for the electrons, is

$$\langle n + 1 | \langle m + 1 | \langle g | \, \psi (t) \rangle = i \sqrt{\frac{\omega_p \omega}{8 \hbar \epsilon (\omega_p) \, \epsilon (\omega)}} \sqrt{\frac{1}{\mathcal{M} \, |\Omega|}} \sqrt{m + 1} \sqrt{n + 1} \alpha$$
$$f \, (\Omega + \omega - \omega_p, t) \; \mathbf{u}_p (\mathbf{r})^t \, M_4 \mathbf{u}^* (\mathbf{r}) \quad \text{(A.61)}$$

where

$$f \, (\Omega + \omega - \omega_p, t) = \frac{1}{i \, (\Omega + \omega - \omega_p)} \left[e^{i(\Omega + \omega - \omega_p)t} - 1 \right] \qquad \text{(A.62)}$$

and M_4 is the matrix

$$M_4 = \sum_e \left\{ \left(\frac{1}{\omega_e - \omega_g - \omega_p} + \frac{1}{\Omega + \omega_e - \omega_g + \omega} \right) \mathbf{d}_{eg}\mathbf{d}''^t_{eg} \right.$$
$$\left. + \left(\frac{1}{\omega_e - \omega_g + \omega} + \frac{1}{\Omega + \omega_e - \omega_g - \omega_p} \right) \mathbf{d}'_{eg}\mathbf{d}^t_{eg} \right\}. \quad \text{(A.63)}$$

In M_4, the sum is to be performed over all excited states for the electrons.

The matrix M_4 conveys some important information. Firstly, the four fractions give the mismatch in energy between initial and virtual states in the four diagrams (see Figure 3.6). If the mismatch is large, the fraction will be small, and the corresponding diagram will then make only a small contribution to the transition rate. This is why the diagrams on the left in Figure 3.6 make a greater contribution to the transition rate than the diagrams on the right. Secondly, the contributions from different excited states for the electrons within the single molecule must be added coherently (interference is possible). In practice, there are usually subsets of states which are degenerate in all respects except for the directions of their vectors $\mathbf{d}_{eg}$ and $\mathbf{d}'_{eg}$. Interference between such subsets is particularly important in accounting for the polarization properties of the scattered radiation.

In this thesis, it is assumed that $\Omega \ll \omega, \omega_p \ll \omega_e - \omega_g$. Hence, Ω may be neglected in Equation A.63, and M_4 is well approximated by

$$\sum_e \left(\frac{1}{\omega_e - \omega_g - \omega_p} + \frac{1}{\omega_e - \omega_g + \omega} \right) \left(\mathbf{d}_{eg}\mathbf{d}''^t_{eg} + \mathbf{d}'_{eg}\mathbf{d}^t_{eg} \right). \quad \text{(A.64)}$$

This is a real, symmetric matrix. As will be discussed in Section A.7, this is all that is required to obtain the polarization properties of the scattered radiation, embodied by Inequality 5.6. However, it will be convenient to make the further approximation that ω and ω_p are negligible in the expression for M_4. M_4 is then well approximated by M_2, where

$$M_2 = 2\sum_e \frac{1}{\omega_e - \omega_g} \left(\mathbf{d}_{eg}\mathbf{d}''^t_{eg} + \mathbf{d}'_{eg}\mathbf{d}^t_{eg} \right). \quad \text{(A.65)}$$

Note that the selection rules for Raman scattering, that is, whether or not a particular phonon mode is Raman active (able to scatter photons) depends entirely on the $\mathbf{d}_{eg}$ and $\mathbf{d}'_{eg}$. In particular, in order for a phonon mode to be Raman active, there must be at least one excited state for the electrons with both $\mathbf{d}_{eg}$ and $\mathbf{d}'_{eg}$ non-zero.

A.5.2 Scattering from many molecules

In a typical textbook discussion of scattering, the next step would be to sum over the optical modes. There are optical modes available with a continuum of frequencies and the dynamics which emerges is heavily dependent on the existence of this continuum. From the point of view of this thesis, summing over the optical modes will divide the problem of scattering in bulk glass from the problem of scattering in single mode fibre, since the optical modes differ in the two geometries. It is desirable to postpone this division for as long as possible in order to avoid having to do a large number of calculations twice. Hence it is convenient to take advantage of the near continuum of phonon modes available in the glass and sum over these instead.

To address the problem of how the contribution of different phonon modes is to be added, imagine the pump mode and signal mode interacting with two phonon modes. These phonon modes may or may not be associated with the same molecule. As a first example, suppose that the first phonon mode is in the coherent state $|\beta_1\rangle$ and the second phonon mode is in the coherent state $|\beta_2\rangle$. The initial state of the system can therefore be written $|g\rangle |\beta_1\rangle |\beta_2\rangle |n\rangle$. Stokes scattering off the first phonon mode causes transitions to the state $|g\rangle |\beta_1\rangle |\beta_2\rangle |n+1\rangle$ (assuming the scattering is from pump to signal). Stokes scattering off the second phonon mode causes transitions to the same state. Interference is therefore possible (for example, the contribution of the two phonon modes may cancel). As a second example, suppose that the first phonon mode is in the number state $|m_1\rangle$, and the second phonon mode is in the number state $|m_2\rangle$, so that the overall initial state for the system is $|g\rangle |m_1\rangle |m_2\rangle |n\rangle$. Stokes scattering off the first phonon mode causes transitions to the state $|g\rangle |m_1+1\rangle |m_2\rangle |n+1\rangle$, while Stokes scattering off the second phonon mode causes transitions to the state $|g\rangle |m_1\rangle |m_2+1\rangle |n+1\rangle$. Since these states are orthogonal, there is no possibility of interference; the probability of a transition when both phonon modes are present is the sum of the transition probabilities when the phonon modes are considered separately. In this thesis, the assumption will be made that the phonon modes are in number states.

Consider now the problem of scattering from a small volume element of glass dV, which is embedded in glass (either bulk glass or a single mode fibre). The volume element is assumed to contain a very large number of molecules, while still being sufficiently small for the mode functions of the electromagnetic field to be approximately constant throughout the volume (at this stage, the assumption that there are only two electromagnetic field modes still applies). The position of the volume element may therefore be taken as $\mathbf{r}$. Let $\rho(\Omega)$ be the number of phonon modes per unit volume

per unit angular frequency. These modes are assumed to be in thermal equilibrium, so each is in a number state, and the probability a mode has m phonons is given by the Boltzmann distribution $B(\Omega, m, T)$

$$B(\Omega, m, T) = \left(1 - e^{-\frac{\hbar|\Omega|}{kT}}\right) e^{-\frac{m\hbar|\Omega|}{kT}}. \tag{A.66}$$

Here k is Boltzmann's constant and T the absolute temperature. In what follows, the assumption is made that modes of the same angular frequency have the same effective mass, $\mathcal{M}$, and that $\mathcal{M}$ is a slowly varying function of frequency. In the more conventional treatment, where the continuum of photon modes is included before adding more than one phonon mode, this assumption does not need to be made but the results obtained are essentially the same.

The number of phonon modes in dV with angular frequencies in the interval $[\Omega, \Omega + d\Omega]$ and m phonons is therefore given by

$$B(\Omega, m, T) \rho(|\Omega|) \, dV \, d\Omega. \tag{A.67}$$

After time t, the probability that Stokes scattering from pump to signal has occurred due to interaction with one of these phonon modes is given by

$$|\langle n + 1| \langle m + 1| \langle g| \, \psi(t)\rangle|^2, \tag{A.68}$$

where $\langle n + 1| \langle m + 1| \langle g| \, \psi(t)\rangle$ is given by Equation A.61. The probability that Stokes scattering has occurred due to interaction with any of the modes is obtained by simply multiplying Equation A.68 by the number of modes (since the contribution of the modes adds incoherently). The result is

$$
\begin{aligned}
B(\Omega, m, T) \, &\rho(|\Omega|) \, dV \, d\Omega \, |\langle n + 1| \langle m + 1| \langle g| \, \psi(t)\rangle|^2 \\
&= B(\Omega, m, T) \, \rho(|\Omega|) \, dV \, d\Omega \, \frac{\omega_p \omega}{8\hbar \epsilon(\omega_p) \epsilon(\omega)} \frac{1}{\mathcal{M} |\Omega|} (m + 1)(n + 1) |\alpha|^2 \\
&\quad |f(\Omega + \omega - \omega_p, t)|^2 \, |\mathbf{u}_p(\mathbf{r})|^2 \, |\mathbf{u}(\mathbf{r})|^2 \, \overline{\left(\mathbf{e}_p^t M_2 \mathbf{e}\right)^2} \quad \text{(A.69)}
\end{aligned}
$$

Where $|\mathbf{u}_p(\mathbf{r})|^2 = \mathbf{u}_p(\mathbf{r})^* \cdot \mathbf{u}_p(\mathbf{r})$ (and likewise for $|\mathbf{u}(\mathbf{r})|^2$) and the bar over $\left(\mathbf{e}_p^t M_2 \mathbf{e}\right)^2$ indicates average over all orientations of M_2 (the molecules are randomly oriented).

Let $P(t, m)$ denote the probability that a Stokes scattering has occurred after time t due to interaction with all the phonon modes containing m phonons (that is, not just those modes with angular frequencies in the interval

$[\Omega, \Omega + d\Omega]$). $P(t, m)$ is obtained by integrating Equation A.69 over Ω

$$P(t, m) = \int_0^\infty d\Omega\, B(\Omega, m, T)\, dV\, \frac{\omega_p \omega}{8\hbar\epsilon(\omega_p)\,\epsilon(\omega)}\, \frac{\rho(|\Omega|)\, \overline{\left(\mathbf{e}_p^t M_2 \mathbf{e}\right)^2}}{\mathcal{M}\,|\Omega|}\, (m+1)$$
$$(n+1)\, |\alpha|^2\, |\mathbf{u}_p(\mathbf{r})|^2\, |\mathbf{u}(\mathbf{r})|^2\, |f(\Omega + \omega - \omega_p, t)|^2 \quad \text{(A.70)}$$

In Equation A.70, $|f(\Omega + \omega - \omega_p, t)|^2$ is sharply peaked about $\Omega = \omega_p - \omega$ and essentially zero everywhere else, while the remaining factors are all slowly varying functions of Ω. Equation A.70 is therefore well approximated by

$$P(t, m) = B(\Omega, m, T)\, dV\, \frac{\omega_p \omega}{8\hbar\epsilon(\omega_p)\,\epsilon(\omega)} \frac{\rho(|\Omega|)\, \overline{\left(\mathbf{e}_p^t M_2 \mathbf{e}\right)^2}}{\mathcal{M}\,|\Omega|}\, (m+1)\,(n+1)$$
$$|\alpha|^2\, |\mathbf{u}_p(\mathbf{r})|^2\, |\mathbf{u}(\mathbf{r})|^2 \int_{-\infty}^\infty dx\, |f(x, t)|^2 \quad \text{(A.71)}$$

where Ω is now to be interpreted as

$$\Omega = \omega_p - \omega. \quad \text{(A.72)}$$

As an aside, if the pump is pulsed then it will contain a range of angular frequencies which extend over some bandwidth $\Delta\omega_p$. In Equation A.70 it will then be necessary to integrate over this bandwidth. In simplistic terms, this means that $|f(\Omega + \omega - \omega_p, t)|^2$ will be significant over an angular frequency interval of width $\Delta\omega_p$, centred at $\Omega \simeq \omega_p - \omega$. If $\Delta\omega_p$ is wider than features in the Raman spectrum then it will not be possible to assume

$$\frac{\rho(|\Omega|)\, \overline{\left(\mathbf{e}_p^t M_2 \mathbf{e}\right)^2}}{\mathcal{M}\,|\Omega|}$$

is independent of Ω and able to be factored out of the integral over Ω, as has been done in going from Equation A.70 to Equation A.71. This indicates that the theory presented in this appendix will only be correct for pulses provided their bandwidth is sufficiently narrow (see Section 5.5) and also indicates how the theory must be modified in order to cope with shorter pulses with broader bandwidths.

According to Gradshteyn and Rhzhik [36, Section 3.782]

$$\int_{-\infty}^\infty dx\, |f(x, t)|^2 = 2\pi t. \quad \text{(A.73)}$$

Therefore the transition rate for Stokes scattering from pump to signal mode, due to the phonon modes containing m phonons, obtained by differentiating

$P(t, m)$ with respect to time is

$$\text{rate} = B\left(\Omega, m, T\right) dV \frac{\omega_p \omega}{8\hbar\epsilon\left(\omega_p\right)\epsilon\left(\omega\right)} \frac{\rho\left(|\Omega|\right)\overline{\left(\mathbf{e}_p^t M_2 \mathbf{e}\right)^2}}{\mathcal{M}\left|\Omega\right|}\left(m+1\right)\left(n+1\right)$$
$$\left|\alpha\right|^2 \left|\mathbf{u}_p\left(\mathbf{r}\right)\right|^2 \left|\mathbf{u}\left(\mathbf{r}\right)\right|^2 2\pi. \quad \text{(A.74)}$$

A.6 Spontaneous and stimulated scattering

The transition rate is observed to depend on the factor $(n+1)$. The n accounts for stimulated scattering (the presence of photons in the signal mode enhances the probability of scattering to the mode), while the 1 accounts for spontaneous scattering (transitions occur even if the signal mode starts in the vacuum state).

At this point it is worthwhile making a digression to consider some typical experimental parameters for the case $n = 1$. This corresponds to spontaneous and stimulated scattering being of equal significance, providing a useful estimate for the optical power required at signal frequencies for stimulated scattering to be observed. The intensity of the signal mode is given by [53, p177]

$$I\left(\mathbf{r}\right) = c\left(\omega\right)\hbar\omega n\left|\mathbf{u}\left(\mathbf{r}\right)\right|^2. \quad \text{(A.75)}$$

(Similarly the intensity of the pump beam is given by

$$I_p\left(\mathbf{r}\right) = c\left(\omega_p\right)\hbar\omega_p\left|\alpha\right|^2\left|\mathbf{u}_p\left(\mathbf{r}\right)\right|^2 \text{).} \quad \text{(A.76)}$$

In the case of a fibre, and taking the light as propagating parallel to the z axis (see Section 5.3), the optical power of the signal mode, obtained by integrating Equation A.75 over the area of the fibre is

$$P = c\left(\omega\right)\hbar\omega n\int_{-\infty}^{\infty} dx \int_{-\infty}^{\infty} dy \left|\mathbf{u}\left(\mathbf{r}\right)\right|^2. \quad \text{(A.77)}$$

Using Equations A.28 and 4.2, this simplifies to

$$P = c\left(\omega\right)\hbar\omega n\frac{1}{L}. \quad \text{(A.78)}$$

where L is the arbitrary length introduced in Section A.3.2. (The analogous equation for the pump beam is

$$P_p = c\left(\omega_p\right)\hbar\omega_p\left|\alpha\right|^2\frac{1}{L} \text{).} \quad \text{(A.79)}$$

Lifting temporarily the restriction that there is only one signal mode, consider all the signal modes with angular frequencies in the interval $[\omega, \omega + d\omega]$. If each signal mode has one photon then the power in each mode is $c(\omega)\,\hbar\omega/L$. Assuming the powers in the modes add incoherently, the total power is the power in each mode multiplied by the number of modes. The number of modes is given by $\rho_f(\omega)\,d\omega$ (see Section A.3.2). Using Equation A.31 the power per unit angular frequency, assuming one photon per mode, is therefore

$$\Gamma = \frac{\hbar\omega}{2\pi}. \tag{A.80}$$

For light of red wavelength, this is approximately $5 \times 10^{-20}\mathrm{W}/\left(\mathrm{rad/s}\right)$, which corresponds to a power per unit wavelength of 220nW/nm.

A.7 Material Raman functions

Returning now to the problem of scattering to a single mode, note that $\overline{\left(\mathbf{e}_p^t M_2 \mathbf{e}\right)^2}$, which appears in Equation A.74, is an average over all orientations of M_2, and can therefore only depend on the angle between $\mathbf{e}_p$ and $\mathbf{e}$. The material Raman functions $M_\parallel$ and $M_\perp$ are defined by

$$M_\parallel = \frac{\rho\left(|\Omega|\right)\overline{\left(\mathbf{e}_p^t M_2 \mathbf{e}\right)^2}}{\mathcal{M}\,|\Omega|}, \mathbf{e}_p \text{ and } \mathbf{e} \text{ parallel}, \tag{A.81}$$

and

$$M_\perp = \frac{\rho\left(|\Omega|\right)\overline{\left(\mathbf{e}_p^t M_2 \mathbf{e}\right)^2}}{\mathcal{M}\,|\Omega|}, \mathbf{e}_p \text{ and } \mathbf{e} \text{ perpendicular}. \tag{A.82}$$

M_2 is a real, symmetric matrix, which guarantees that its eigenvectors are orthogonal. Long [51] shows that this is sufficient to give Inequality 5.6. For discrete molecules, if the equilibrium geometry of the molecule is known, and if the motion of the nuclei associated with the phonon mode has been identified, then, in some cases, it may be possible to deduce a stronger relationship between $M_\perp$ and $M_\parallel$. For example, in the case of molecules whose equilibrium geometry has tetrahedral symmetry, those phonon modes in which this symmetry is preserved as the nuclei move can be shown to have $M_\perp \equiv 0$ [51, p92].

A.8 Anti-Stokes scattering

The analysis for anti-Stokes scattering follows as outlined for Stokes scattering in Section A.5. The diagrams for anti-Stokes scattering are exactly

the same as those for Stokes scattering, except that the phonon is destroyed rather than created. This means that terms from the second integral in the Dyson series containing $be^{-i\Omega t}$ are chosen in place of those containing $b^\dagger e^{i\Omega t}$. Hence, $\sqrt{m+1}$ is replaced with $\sqrt{m}$, and Ω with $-\Omega$. Using Equation A.72, the angular frequency of the phonon modes which contribute most to the scattering is then

$$\Omega = \omega - \omega_p. \tag{A.83}$$

This angular frequency must be positive since it is the angular frequency of phonon modes. It is also the angular frequency which should be used in the final expression for the rate. In practice, it is convenient to retain Equation A.72 as the definition of Ω. Ω is then negative in the case of anti-Stokes scattering. The final expression for the rate will still be correct, provided absolute value braces are placed around Ω. In Equation A.74, these absolute value braces are already present, having been added at appropriate points throughout the treatment. Hence the rate for anti-Stokes scattering is given by Equation A.74 with $(m+1)$ replaced by m.

A.9 Scattering from signal to pump

This is important in stimulated scattering experiments. Again, the treatment follows that for Stokes scattering from pump to signal in Section A.5. The diagrams for Stokes scattering from signal to pump are the same as those in Figure 3.6, except that the signal photon is destroyed rather than created and vice versa for the pump photon. This means that terms from the second integral in the Dyson series are chosen which contain $ae^{-i\omega t}\mathbf{u}(\mathbf{r})$ in place of $-a^\dagger e^{i\omega t}\mathbf{u}^*(\mathbf{r})$ and $-\alpha^* e^{i\omega_p t}\mathbf{u}_p^*(\mathbf{r})$ in place of $\alpha e^{-i\omega_p t}\mathbf{u}_p(\mathbf{r})$. These substitutions actually have little effect on the final expression for the rate. The two sign changes cancel, and the rate for Stokes scattering from signal to pump is found to be given by Equation A.74 with $(n+1)$ replaced by n.

A.10 The continuum of signal modes

Equation A.74 gives the transition rate for scattering to a single signal mode. In a scattering experiment, what is measured is not the transition rate to one mode, but the transition rate to a group of modes. If the modes start in number states (which is certainly the case in spontaneous scattering, since the modes start in the vacuum state), then the total transition rate to the group of modes is just the sum of the transition rates to the individual modes. This is because scattering to one particular mode takes the system to a state

which is orthogonal to all other possible outcomes, so there is no possibility of interference. The situation is analogous to that discussed for the phonon modes in Section A.5.2.

In a stimulated scattering experiment, the state of the signal modes is, in principle, arbitrary and interference between transitions to different signal modes might occur. In this thesis, this possibility will be neglected, perhaps without adequate justification. The approach taken in this appendix, of calculating transition rates, is not well suited to resolving this difficulty. A better approach would be to formulate a Heisenberg equation of motion for the photon intensity operator [53] associated with the signal modes.

Having decided, rather arbitrarily, that the transition rates can be added incoherently, all that remains is to perform the addition. At this point the treatments for bulk glass and fibre geometries must diverge. The bulk glass geometry will be discussed first.

A.10.1 Spontaneous scattering in bulk glass

It is now assumed that the geometry of the experiment is the same as that in Section 5.1. Using the results of Section A.3.3, the number of signal modes with propagation directions inside $d\Phi$ and angular frequencies in the interval $[\omega, \omega + d\omega]$, is given by $\rho_b(\omega) \, d\Phi d\omega / 4\pi$. Multiplying this by Equation A.74 gives the transition rate for Stokes scattering to these propagation directions and angular frequencies. Since, spontaneous scattering is being considered, n in Equation A.74 should be set to zero (see Section A.6). Assuming parallel scattering, the result is

$$\text{rate} = 4\pi \left(\frac{L}{2\pi c(\omega)} \right)^3 \omega^2 d\Phi d\omega / 4\pi \, B(\Omega, m, T) \, dV \, \frac{\omega_p \omega}{8\hbar \epsilon(\omega_p) \, \epsilon(\omega)} M_\parallel (m+1)$$
$$|\alpha|^2 \, |\mathbf{u}_p(\mathbf{r})|^2 \, |\mathbf{u}(\mathbf{r})|^2 \, 2\pi. \quad \text{(A.84)}$$

Using Equation A.76, the pump power incident on dV is

$$P_p = c(\omega_p) \, \hbar \omega_p \, |\alpha|^2 \, |\mathbf{u}_p(\mathbf{r})|^2 \, dA. \quad \text{(A.85)}$$

Using this, and Equation A.33, reduces Equation A.84 to

$$\text{rate} = \frac{1}{\pi^2 c(\omega)^3 \, c(\omega_p)} \omega^3 d\Phi d\omega \, B(\Omega, m, T) \, dz \, \frac{1}{32\hbar^2 \epsilon(\omega_p) \, \epsilon(\omega)} M_\parallel (m+1) \, P_p.$$
$$\text{(A.86)}$$

This gives the transition rate due to those phonon modes with m phonons. The total transition rate is obtained by summing over all m. The scattered

optical power, P, is the transition rate multiplied by $\hbar\omega$, the energy of a scattered photon. The result is

$$P = \frac{\omega}{\omega_p} P_p \frac{\omega_p \omega^3}{32\pi^2 \hbar c (\omega)^3 c(\omega_p) \epsilon(\omega_p) \epsilon(\omega)} M_\| \left[\sum_{m=0}^{\infty} B(\Omega, m, T)(m+1) \right] d\Phi dz d\omega.$$

(A.87)

The sum over m is equal to $h(\Omega, T)$ as defined in Equation 5.3. Using the relationship between permittivity and refractive index (Equation A.27) recovers the equation for parallel Stokes scattering in Section 5.1. The equations for perpendicular and anti-Stokes scattering follow similarly.

A.10.2 Stimulated scattering in bulk glass

With reference to Section 5.2, consider the scattering from an infinite sheet of glass in the xy plane of thickness dz. To begin with, suppose there is just one signal mode, that this mode contains n photons, and that n is sufficiently large that spontaneous scattering can be neglected (that is $(n+1) \simeq n$; see Section A.6). Consider a piece of the glass sheet of area dA and volume $dV = dAdz$. Suppose the signal is at lower frequency than the pump. Equation A.74 therefore gives the transition rate for Stokes scattering from pump to signal due to the piece of glass. Using Sections A.8 and A.9, a corresponding transition rate can be obtained for anti-Stokes scattering from signal to pump. The net transition rate from pump to signal is the difference of the two rates. Assuming parallel scattering, the result is

$$B(\Omega, m, T) dV \frac{\omega_p \omega}{8\hbar \epsilon(\omega_p) \epsilon(\omega)} M_\| n |\alpha|^2 |\mathbf{u}_p(\mathbf{r})|^2 |\mathbf{u}(\mathbf{r})|^2 2\pi.$$

(A.88)

This is the transition rate due to those phonon modes with m phonons, but note that it is independent of m (which gives stimulated scattering its immunity to temperature change). The total transition rate is obtained by summing over all m. Using Equations A.76 and A.75, the result is

$$\text{rate} = dV \frac{\omega_p \omega}{8\hbar \epsilon(\omega_p) \epsilon(\omega)} M_\| \frac{I_p(\mathbf{r})}{c(\omega_p) \hbar\omega_p} \frac{I(\mathbf{r})}{c(\omega) \hbar\omega} 2\pi.$$

(A.89)

The photons produced in the piece of glass of area dA must emerge through the area dA. The change in intensity of the signal beam on crossing the glass sheet is therefore

$$dI = \text{rate} \times \frac{\hbar\omega}{dA}.$$

(A.90)

Using Equation A.89 this becomes

$$dI = \frac{\pi\omega}{4\hbar^2 \epsilon(\omega_p) \epsilon(\omega)} \frac{M_\|}{c(\omega_p) c(\omega)} I_p(\mathbf{r}) I(\mathbf{r}) \, dz$$

(A.91)

If there is more than one signal mode, and if the transitions to the modes are independent (there is no interference), then the intensity of each mode will obey an equation like Equation A.91. These equations can be added (all the left hand sides added and all the right hand sides added). The result is the same as Equation A.91 but with I now equal to the intensity summed over all the modes. Dividing by the angular frequency interval spanned by the modes, and using Equation A.27 for the permittivity, the equations in Section 5.2 are obtained. The results for perpendicular scattering and the case where $\omega > \omega_p$ follow similarly.

A.10.3   Scattering in fibres

With reference to Section 5.3, consider first just a pump (which may be propagating in either direction) and one signal mode (which is assumed to be propagating in the $+z$ direction). Consider also, a cross-section through the fibre in the xy plane of thickness dz. Take one small piece of the cross-section of area dA and volume $dV = dAdz$. Assuming that the signal beam is at lower frequency than the pump beam, Equation A.74 gives the transition rate for Stokes scattering (both spontaneous and stimulated components) from pump to signal due to the small piece of the cross-section. Using Sections A.8 and A.9, a corresponding transition rate can be obtained for anti-Stokes scattering from signal to pump. The net transition rate from pump to signal is the difference of the two rates. Assuming parallel scattering, the result is

$$B\left(\Omega, m, T\right) dV \, \frac{\pi \omega_p \omega}{4\hbar \epsilon\left(\omega_p\right) \epsilon\left(\omega\right)} M_{\parallel}\left(n + m + 1\right) \left|\alpha\right|^2 \left|\mathbf{u}_p\left(\mathbf{r}\right)\right|^2 \left|\mathbf{u}\left(\mathbf{r}\right)\right|^2. \quad \text{(A.92)}$$

This is the rate due to those phonon modes with m phonons. The total rate due to all phonon modes is obtained by summing over m. Using Equations A.79 and A.78, the result is

$$\text{rate} = dV \, \frac{\pi \omega_p \omega}{4\hbar \epsilon\left(\omega_p\right) \epsilon\left(\omega\right)} M_{\parallel} \left[\frac{LP}{c\left(\omega\right) \hbar\omega} + h\left(\Omega, T\right)\right]$$
$$\frac{LP_p}{c\left(\omega_p\right) \hbar\omega_p} \left|\mathbf{u}_p\left(\mathbf{r}\right)\right|^2 \left|\mathbf{u}\left(\mathbf{r}\right)\right|^2, \quad \text{(A.93)}$$

where $h\left(\Omega, T\right)$ is given by Equation 5.3. Multiplying the rate by $\hbar\omega$ gives the power added to the signal mode by the small piece of glass of area dA. In order to get the total power added to the signal mode due to all the glass in the cross-section of thickness dz, it is necessary to integrate over the area

of the cross-section. Using Equation A.28, the result is

$$dP = \frac{\pi \omega_p \omega^2}{4\epsilon(\omega_p)\epsilon(\omega)} M_\| \left[\frac{LP}{c(\omega)\hbar\omega} + h(\Omega,T) \right] \frac{LP_p}{c(\omega_p)\hbar\omega_p}$$
$$\left(\int_{-\infty}^{\infty} dx \int_{-\infty}^{\infty} dy \frac{|f_p|^2}{L} \frac{|f|^2}{L} \right) dz. \quad (A.94)$$

If there is more than one signal mode, and if the scattering to the modes is independent (there is no interference) then an equation like Equation A.94 will hold for each mode. The equations can be added together (all the left hand sides can be added and all the right hand sides can be added) for all the modes with angular frequencies inside the interval $[\omega, \omega + d\omega]$. This addition must be done with some care, since the two terms inside the square brackets in Equation A.94 must be treated differently. The first term contains the power in each mode. These terms will sum to give the total power. The second term gives a contribution of $h(\Omega,T)$ for each mode. These will therefore sum to give $h(\Omega,T)$ multiplied by the number of modes. Using the fact that $\rho_f(\omega)\, d\omega$ gives the number of modes in the interval, and using Equation A.31 for $\rho_f(\omega)$, the total power dP added to all signal modes in the interval $[\omega, \omega + d\omega]$, on crossing the thickness dz, is therefore

$$dP = \frac{\pi\omega^2}{4\hbar\epsilon(\omega_p)\epsilon(\omega)} \frac{M_\|}{c(\omega_p)c(\omega)} \left[\frac{P}{\hbar\omega} + h(\Omega,T)\frac{1}{2\pi}d\omega \right]$$
$$\left(\int_{-\infty}^{\infty} dx \int_{-\infty}^{\infty} dy \, |f_p|^2 |f|^2 \right) P_p dz, \quad (A.95)$$

where P is now to be interpreted as the total power in the interval $d\omega$. Dividing this through by $d\omega$ (to convert from P to Γ), and using Equation A.27 for the permittivity, the equations in Section 5.3 are obtained. The results for perpendicular scattering and the case where $\omega > \omega_p$ follow similarly.

A.11 Anharmonicity

In Section A.1.4 the potential experienced by the nuclei and the dipole matrix elements were both expanded as Taylor series (see Equations A.13 and A.14). So far the higher order terms in these Taylor series have been neglected. If the higher order terms in Equation A.13 are significant then this is called mechanical anharmonicity. Likewise if the higher order terms in Equation A.14 are significant then this is called electrical anharmonicity. Sometimes, in the spectroscopy literature, 'nonlinear' is used in place of 'anharmonic'. This is

rather confusing as 'nonlinear' in optics has come to mean nonlinear interaction between material and light, whilst, in this case, the nonlinearity is entirely a feature of the material.

In Section A.1.4 the discussion was restricted to just two vibrational modes, Q_a and Q_b, and the same approach is adopted here. It is useful to begin with the classical picture of Raman scattering briefly mentioned in Section 3.6.2. If one of the higher order terms involving just Q_a is significant in Equation A.13 then the nuclear motion associated with Q_a will not be harmonic. As well as having a fundamental angular frequency, Ω_a, there will also be harmonics, $2\Omega_a$, $3\Omega_a$, etc. In the classical picture, the electronic motion follows the optical field (angular frequency ω_p) but is amplitude modulated at the vibrational frequency of the nuclei. Hence the electronic motion will have angular frequency components at ω_p (Rayleigh), $\omega_p \pm \Omega_a$ (called fundamental) and $\omega_p \pm 2\Omega_a$, etc. (called overtones). If the higher order terms containing products of both Q_a and Q_b are significant, then the two vibrational modes do not completely decoupled (as suggested by Section A.1.4) and mode a will have angular frequency components at $\Omega_a \pm \Omega_b$, etc. This results in scattered light with angular frequency components $\omega_p \pm \Omega_a \pm \Omega_b$, etc. (called combination bands).

Typical higher order terms in Equation A.14 are $(\partial^2 \mathbf{d}_{pq}/\partial Q_a^2)\, Q_a^2$ and $(\partial^2 \mathbf{d}_{pq}/\partial Q_a \partial Q_b)\, Q_a Q_b$. These will result in the electronic motion having angular frequency components at $\omega_p \pm 2\Omega_a$ and $\omega_p \pm \Omega_a \pm \Omega_b$ even if the nuclear motion is harmonic.

A.11.1 Spontaneous scattering for overtones

The theory for overtones and combination bands develops in exactly the same way as the theory for fundamental transitions outlined in this appendix. If this is pursued, it leads to the following conclusions for the spontaneous scattering for overtones. Firstly, there is no simple relation between the strength of an overtone and the strength of its fundamental; in some rare cases, an overtone will be strong even though its fundamental is not Raman active (see Section A.5.1). Secondly, the ratio of perpendicular to parallel scattering for overtones also obeys Inequality 5.6, although the ratio for the overtone is not necessarily the same as the ratio for its fundamental. Finally, the temperature dependence of overtones can be anomalous, although the ratio of anti-Stokes to Stokes scattering is the same for overtones and fundamental transitions (so Equation 9.4 will also hold for overtones, where Ω is the difference in angular frequency between pump and scattered light, which is twice the angular frequency of the phonon mode).

Bibliography

[1] N. Anders Olsson and J. Hegarty, 'Noise properties of a Raman amplifier,' *J. Lightwave Technol.* **LT-4**, 396-398 (1986).

[2] W.T. Anderson and D. L. Philen, 'Spot size measurements for single-mode fibres: a comparison of four techniques,' *J. Lightwave Technol.* **LT-1**, 20-26 (1983).

[3] B. P. Antonyuk and V. B. Antonyuk, 'Second-harmonic generation in Ge-doped silica fibres: experiment and theory,' *J. Mod. Opt.* **45**, 257-268 (1998).

[4] B. P. Antonyuk and V. B. Antonyuk, 'High efficient second harmonic generation in Ge-doped silica fibers,' *Opt. Commun.* **147**, 143-147 (1998).

[5] G. P. Agrawal, *Nonlinear fiber optics* (Academic Press, San Diego, 1989 (1st Edn.) and 1995 (2nd Edn.)).

[6] Y. Aoki, S. Kishida, H. Honmou, K. Washio and M. Sugimoto, 'Efficient backward and forward pumping cw Raman amplification for InGaAsP laser light in silica fibers,' *Electron. Lett.* **19**, 620-622 (1983).

[7] Y. Aoki, 'Properties of fiber Raman amplifiers and their applicability to digital optical communication systems,' *J. Lightwave Technol.* **LT-6**, 1225-1239 (1988).

[8] R. M. Atkins, 'Measurement of the ultraviolet absorption spectrum of optical fibres,' *Opt. Lett.* **17**, 469-471 (1992).

[9] J. Auyeung and A. Yariv, 'Spontaneous and stimulated Raman scattering in long low loss fibers,' IEEE J. *Quantum Electron.* **QE-14**, 347-352 (1978).

[10] O. Aytür and P. Kumar, 'Pulsed twin beams of light,' *Phys. Rev. Lett.* **65**, 1551-1554 (1990).

[11] B. G. Bagley, C. R. Kurkjian, J. W. Mitchell, G. E. Peterson and A. R. Tynes, 'Materials, properties and choices,' Chapter 7 in [58].

[12] L. E. Ballentine, *Quantum mechanics* (Prentice Hall, Englewood Cliffs, N.J, 1990).

[13] R. J. Bell and P. Dean, 'Atomic vibrations in vitreous silica,' *Discuss. Faraday Soc.* **50**, 55- (1970).

[14] N. Bloembergen, 'The stimulated Raman effect,' *Am. J. Phys.* **35**, 989-1023 (1967).

[15] B. H. Bransden and C. J. Joachain, *Introduction to Quantum mechanics* (Longman, Essex, 1989).

[16] E. Brinkmeyer, 'Analysis of the backscattering method for single-mode optical fibers,' *J. Opt. Soc. Am.* **70**, 1010-1012 (1987).

[17] E. L. Buckland and R. W. Boyd, 'Electrostrictive contribution to the intensity-dependent refractive index of optical fibers,' *Opt. Lett.* **21**, 1117-1119 (1996).

[18] E. L. Buckland and R. W. Boyd, 'Measurement of the frequency response of the electrostrictive nonlinearity in optical fibers,' *Opt. Lett.* **22**, 676–678 (1997).

[19] J. Canning and M. G. Sceats, 'Spatial distribution of 650nm luminescence in UV-processed germanosilicate preforms,' *Opt. Lett.* **19**, 1119-1121 (1994).

[20] S. J. Carter and P. D. Drummond, 'Quantum theory of fibre optics I: Heisenberg equations,' to be published.

[21] P. Chmela and J. Petráček, 'First demonstration of $\chi^{(2)}$ grating encoding function in optical fibers,' *Opt. Commun.* **156**, 374-383 (1998).

[22] N. Christensen, R. Leonhardt and J. D. Harvey, 'Noise characteristics of cross-phase modulation instability light,' *Opt. Commun.* **101**, 205-212 (1993).

[23] L. G. Cohen, P. Kaiser, P. D. Lazay and H. M. Presby, 'Fiber characterization,' Chapter 11 in [58].

[24] B. Crosignani, P. Di Porto and S. Solimeno, 'Influence of guiding structures on spontaneous and stimulated emission: Raman scattering in optical fibres,' *Phys. Rev.* A **21**, 594-598 (1980).

[25] M. L. Dakss and P. Melman, 'Amplified spontaneous Raman scattering and gain in fiber Raman amplifiers,' *J. Lightwave Technol.* **LT-3**, 806-813 (1985).

[26] J. C. Daly, *Fiber optics* (CRC Press, Boca Raton, Florida, c1984).

[27] P. A. M. Dirac, *The Principles of Quantum Mechanics* (3rd edn) (Clarendon Press, Oxford, 1947).

[28] P. A. M. Dirac, *Lectures on Quantum Field Theory* (Belfer Graduate School of Science, Yeshiva University, New York, 1966).

[29] D. J. Dougherty, F. X. Kärtner, H. A. Haus and E. P. Ippen, 'Measurement of the Raman gain spectrum of optical fibers,' *Opt. Lett.* **20**, 31–33 (1995).

[30] P. D. Drummond, T. A. B. Kennedy, J. M. Dudley, R. Leonhardt and J. D. Harvey, 'Cross-phase modulational instability in high-birefringence fibers,' *Opt. Commun.* **78**, 137-142 (1990).

[31] J. M. Dudley, 'Coherent transient phenomena in the mode-locked argon laser,' Ph.D. thesis, University of Auckland (1992).

[32] A. Fellegara, A. Melloni and M. Martinelli, 'Measurement of the frequency response induced by electrostriction in optical fibers,' *Opt. Lett.* **22**, 1615-1617 (1997).

[33] F. L. Galeener and G. Lucovsky, 'Longitudinal optical vibrations in glasses: GeO_2 and SiO_2,' *Phys. Rev. Lett.* **37**, 1474-1478 (1976).

[34] F. L. Galeener, J. C. Mikkelsen, R. H. Geils and W. J. Mosby, 'The relative Raman cross-sections of vitreous SiO_2, GeO_2, B_2O_3 and P_2O_5,' *Appl. Phys. Lett.* **32**, 34-36 (1978).

[35] M. P. Gold and A. H. Hartog, 'Measurement of backscatter factor in single-mode fibres,' *Electron. Lett.* **17**, 965-966 (1981).

[36] I. S. Gradshteyn and I. M. Rhzhik, *Table of integrals, series and product*, corrected and enlarged edn. (Academic Press, New York, 1980).

[37] M. Hass, 'Temperature dependence of the Raman spectra of vitreous silica,' *Solid State Commun.* **7**, 1069-1071 (1969).

[38] M. Hass, 'Raman spectra of vitreous silica, germania and sodium silicate glasses,' *J. Phys. Chem. Solids* **31**, 415-422 (1970).

[39] C. Headley, III, and G. P. Agrawal, 'Noise characteristics and statistics of picosecond Stokes pulses generated in optical fibers through stimulated Raman scattering,' *IEEE J. Quantum Electron.* **QE-31**, 2058-2067 (1995).

[40] E. Hecht, *Optics* (Addison-Wesley, Reading, Massachusetts, 1998).

[41] R. W. Hellwarth, 'Theory of stimulated Raman scattering,' *Phys. Rev.* **130**, 1850-1852 (1963).

[42] R. Hellwarth, J. Cherlow and T.-T. Yang, 'Origin and frequency dependence of nonlinear optical susceptibility of glasses,' *Phys. Rev. B.* **11**, 964-967 (1975).

[43] R. W. Hellwarth, 'Third-order optical susceptibilities of liquids and solids,' *Prog. Quant. Electr.* **5**, 1-68 (1977).

[44] K. O. Hill, B. Malo, F. Bilodeau and D. C. Johnson, 'Photosensitivity in optical fibers,' *Ann. R. Mater.* **23**, 125-157 (1993).

[45] D. B. Hirst, 'Phase-wave effects in mode-locked argon and krypton lasers,' Ph.D. thesis, University of Auckland (1995).

[46] M. Ikeda, 'Stimulated Raman amplification characteristics in long span single-mode silica fibers,' *Opt. Commun.* **39**, 148-152 (1981).

[47] A. Kovačec, 'On an algorithmic method to prove inequalities,' in *General Inequalities III,* E. F. Beckenbach and W. Walter, eds. (Birkhäuser Verlag, Basel, 1983), pp69-89. See also A. Kovačec, 'An algorithmic approach to inequalities I,' *Monatsh. Math.* **92**, 19-35 (1981).

[48] P. G. Kwiat and H. Weinfurter, 'Embedded Bell-state analysis,' *Phys. Rev. A* **58**, R2623-2626 (1998).

[49] G.-L. Lan, P. K. Banerjee and S. S. Mitra, 'Raman scattering in optical fibers,' *J. Raman Spectrosc.* **11**, 416-423 (1981).

[50] K. X. Liu and E. Garmire, 'Understanding the formation of the SRS Stokes spectrum in fused silica fibers,' *IEEE J. Quantum Electron.* **QE-27**, 1022-1030 (1991).

[51] D. A. Long, *Raman Spectroscopy* (McGraw-Hill, New York, 1977).

[52] R. S. Longhurst, *Geometrical and Physical Optics*, 3rd Edn (Longman, Essex, 1973).

[53] R. Loudon, *The quantum theory of light*, 2nd Edn (Oxford University Press, Oxford, 1983).

[54] J. D. Mackenzie (ed), *Modern aspects of the vitreous state* Vol.1 (Butterworths, London, 1960).

[55] D. Mahgerefteh, D. L. Butler, J. Goldhar, B. Rosenberg and G. L. Burdge, 'Technique for measurement of the Raman gain coefficient in optical fibers,' *Opt. Lett.* **21**, 2026-2028 (1996).

[56] H. Marantz, R. I. Rudko and C. L. Tang, 'The singly ionized krypton laser,' *IEEE J. Quantum Electron.* **QE-5**, 38-44 (1969).

[57] A. Melloni, M. Frasca, A. Garavaglia, A. Tonini and M. Martinelli, 'Direct measurement of electrostriction in optical fibers,' *Opt. Lett.* **23**, 691-693 (1998).

[58] S. E. Miller and A. G. Chynoweth (Eds.), *Optical Fiber Telecommunications* (Academic Press, New York, 1979).

[59] T. Mizunami, T. Miyazaki and K. Takagi, 'Short-pulse ultraviolet fiber Raman laser pumped by a XeCl excimer laser,' *J. Opt. Soc. Am.* B **4**, 498-504 (1987).

[60] T. Mizunami, M. Hashimoto, S. Gupta, Y. Uchida and T. Shimomura, 'Wavelength dependence of two-photon absorption in germanosilicate optical fibers,' *Opt. Commun.* **138**, 40-44 (1997).

[61] K. Mochizuki, N. Edagawa and Y. Iwamoto, 'Amplified spontaneous Raman scattering in fiber Raman amplifiers,' *J. Lightwave Technol.* **LT-4**, 1328-1333 (1986).

[62] S. G. Murdoch, R. Leonhardt and J. D. Harvey, 'Polarization modulation instability in weakly birefringent fibers,' *Opt. Lett.* **20**, 866-868 (1995).

[63] S. G. Murdoch, 'Polarization modulation instability in birefringent optical fibres,' Ph.D. thesis, University of Auckland (1997).

[64] M. Nakazawa, 'Rayleigh backscattering theory for single-mode optical fibers,' *J. Opt. Soc. Am.* **73**, 1175-1180 (1983).

[65] E. -G. Neumann, *Single-mode fibres* (Springer-Verlag, Berlin, 1988).

[66] V. B. Neustruev, 'Colour centres in germanosilicate glass and optical fibres,' *J. Phys.: Condens. Matter* **6**, 6901-6936 (1994).

[67] P. O'Connor and J. Tauc, 'Light scattering in optical waveguides,' *Appl. Opt.* **17**, 3226-3231 (1978).

[68] F. L. Pedrotti and L. S. Pedrotti, *Introduction to Optics* (Prentice-Hall, New Jersey, 1993).

[69] R. Pini, R. Salimbeni, M. Matera and C. Lin, 'Wideband frequency conversion in the UV by nine orders of stimulated Raman scattering in a XeCl laser pumped multimode silica fibre,' *Appl. Phys. Lett.* **43**, 517-518 (1983).

[70] B. Poumellec and F. Kherbouche, 'The Photorefractive Bragg gratings in the fibers for telecommunications,' *J. Phys. III France* **6**, 1595-1624 (1996).

[71] J. E. Rothenberg, 'Modulational instability for normal dispersion,' *Phys. Rev.* A **42**, 682-685 (1990).

[72] M. Rothschild and H. Abad, 'Stimulated Raman scattering in fibres in the ultraviolet,' *Opt. Lett.* **8**, 653-655 (1983).

[73] J. J. Sakurai, *Modern Quantum Mechanics* (Addison-Wesley, Redwood City, California, 1985).

[74] M. G. Sceats, G. R. Atkins, S. B. Poole, 'Photolytic index changes in optical fibers,' *Ann. R. Mater.* **23**, 381-410 (1993).

[75] M. D. Sharma and C. J. R. Sheppard, 'Holmium-doped optical fiber for filter applications,' *Appl. Opt.* **36**, 6815-6821 (1997).

[76] Y. R. Shen and N. Bloembergen, 'Theory of stimulated Brillouin and Raman scattering,' *Phys. Rev.* A **137**, A1787-A1805 (1965).

[77] R. Shuker and R.W. Gammon, 'Raman-scattering selection-rule breaking and the density of states in amorphous materials,' *Phys. Rev. Lett.* **25**, 222-225 (1970).

[78] I. Simon, 'Infra-red studies in glass,' Chapter 6 in [54].

[79] J. R. Simpson, R. H. Stolen, F. M. Sears, W. Pleibel, J. B. MacChesney and R. E. Howard, 'A single-polarization fibre,' J. Lightwave Technol. **LT-1**, 370-374 (1983).

[80] R. G. Smith, 'Optical power handling capacity of low loss optical fibers as determined by stimulated Raman and Brillouin scattering,' *Appl. Opt.* **11**, 2489-2493 (1972).

[81] D. T. Smithey, M. Beck, M. Belsley and M. G. Raymer, 'Sub-shot-noise correlation of total photon number using macroscopic twin pulses of light,' *Phys. Rev. Lett.* **69**, 2650-2653 (1992).

[82] R. H. Stolen, E. P. Ippen and A. R. Tynes, 'Raman oscillation in glass optical waveguide,' Appl. Phys. Lett. **20**, 62-64 (1972).

[83] R. H. Stolen and E. P. Ippen, 'Raman gain in glass optical waveguides,' *Appl. Phys. Lett.* **22**, 276-278 (1973).

[84] R. H. Stolen, 'Nonlinear properties of optical fibres,' Chapter 5 in [58].

[85] R. H. Stolen, 'Polarization effects in fiber Raman and Brillouin lasers,' *IEEE J. Quantum Electron.* **QE-15**, 1157-1160 (1979).

[86] R. H. Stolen, 'Nonlinearity in fiber transmission,' *Proc. IEEE* **68**, 1232-1236 (1980).

[87] R. H. Stolen and M. A. Bösch, 'Low-frequency and low-temperature Raman scattering in silica fibres,' *Phys. Rev. Lett.* **48**, 805-808 (1982).

[88] R. H. Stolen, C. Lee and R. K. Jain, 'Development of the stimulated Raman spectrum in single-mode silica fibers,' *J. Opt. Soc. Am.* B **1**, 652-657 (1984).

[89] R. H. Stolen, J. P. Gordon, W. J. Tomlinson and H. A. Haus, 'Raman response function of silica-core fibers,' *J. Opt. Soc. Am.* B **6**, 1159-1166 (1989).

[90] J. Stone, 'cw Raman fiber amplifier,' *Appl. Phys. Lett.* **26**, 163-165 (1975).

[91] M. C. Tobin and T. Baak, 'Raman spectra of some low-expansion glasses,' *J. Opt. Soc. Am.* **58**, 1459-1461 (1968).

[92] S. Trillo and S. Wabnitz, 'Parametric and Raman amplification in birefringent optical fibers,' *J. Opt. Soc. Am.* B **9**, 1061-1082 (1992).

[93] B. Valk, E. M. Kim and M. M. Salour, 'Second harmonic generation in Ge-doped fibers with a mode-locked Kr$^+$ laser,' *Appl. Phys. Lett.* **51**, 722-724 (1987).

[94] M. P. Varnham, D. N. Payne, R. D. Birch and E. J. Tarbox, 'Single-polarization operation of highly birefringent Bow-Tie optical fibers,' *Electron. Lett.* **19**, 246-247 (1983).

[95] D. von der Linde, M. Maier and W. Kaiser, 'Quantitative investigations of the stimulated Raman effect using subnanosecond light pulses,' *Phys. Rev.* **178**, 11 (1969).

[96] S. Wabnitz, 'Modulational polarization instability of light in a non-linear birefringent dispersive medium,' *Phys. Rev.* A **38**, 2018-2021 (1988).

[97] D. F. Walls and G. J. Milburn, *Quantum Optics* (Springer-Verlag, Berlin, 1994).

[98] G. E. Walrafen, 'New slitless optical fiber laser-Raman spectrometer,' *Appl. Spectrosc.* **29**, 179-185 (1975).

[99] G. E. Walrafen and J. Stone, 'Raman spectral characterization of pure and doped fused silica optical fibres,' *Appl. Spectrosc.* **29**, 337-344 (1975).

[100] D. L. Williams, S. T. Davey, R. Kashyap, J. R. Armitage and B. J. Ainslie, 'Ultraviolet absorption studies on photosensitive germanosilicate preforms and fibres,' *Appl. Phys. Lett.* **59**, 762-764 (1991).

[101] G. Winterling, 'Very-low-frequency Raman scattering in vitreous silica,' *Phys. Rev.* B. **12**, 2432 (1975).

[102] E. J. Woodbury and W. K. Ng, 'Ruby laser operation in the near IR,' *Proc. IRE* **50**, 2367-2367 (1962).

[103] A. Yariv, *Optical Electronics* (CBS College Publishing, New York, 1985).